

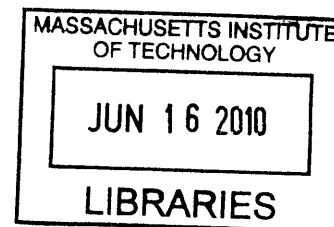
**Biologically inspired materials for
electro-responsive coatings and the
photo-oxidation of water.**

by

Andrew P. Magyar

A.B., Hamilton College (2003)

ARCHIVES



Submitted to the Department of Material Science and Engineering
in partial fulfillment of the requirements for the degree of

Doctor of Philosophy

at the

MASSACHUSETTS INSTITUTE OF TECHNOLOGY

February 2010

© Massachusetts Institute of Technology 2010. All rights reserved.

Author

Department of Material Science and Engineering
November 5, 2009

Certified by..

Angela M. Belcher
Germeshausen Professor of Materials Science and Engineering and
Biological Engineering
Thesis Supervisor

Accepted by

Christine Ortiz
Chair, Departmental Committee on Graduate Students

Report Documentation Page		Form Approved OMB No. 0704-0188
Public reporting burden for the collection of information is estimated to average 1 hour per response, including the time for reviewing instructions, searching existing data sources, gathering and maintaining the data needed, and completing and reviewing the collection of information. Send comments regarding this burden estimate or any other aspect of this collection of information, including suggestions for reducing this burden, to Washington Headquarters Services, Directorate for Information Operations and Reports, 1215 Jefferson Davis Highway, Suite 1204, Arlington VA 22202-4302. Respondents should be aware that notwithstanding any other provision of law, no person shall be subject to a penalty for failing to comply with a collection of information if it does not display a currently valid OMB control number.		
1. REPORT DATE FEB 2010	2. REPORT TYPE	3. DATES COVERED 00-00-2010 to 00-00-2010
4. TITLE AND SUBTITLE Biologically inspired materials for electro-responsive coatings and the photo-oxidation of water		5a. CONTRACT NUMBER
		5b. GRANT NUMBER
		5c. PROGRAM ELEMENT NUMBER
6. AUTHOR(S)	5d. PROJECT NUMBER	
	5e. TASK NUMBER	
	5f. WORK UNIT NUMBER	
7. PERFORMING ORGANIZATION NAME(S) AND ADDRESS(ES) Massachusetts Institute of Technology, 77 Massachusetts Avenue, Cambridge, MA, 02139		8. PERFORMING ORGANIZATION REPORT NUMBER
9. SPONSORING/MONITORING AGENCY NAME(S) AND ADDRESS(ES)		10. SPONSOR/MONITOR'S ACRONYM(S)
		11. SPONSOR/MONITOR'S REPORT NUMBER(S)
12. DISTRIBUTION/AVAILABILITY STATEMENT Approved for public release; distribution unlimited		
13. SUPPLEMENTARY NOTES		

14. ABSTRACT

Evolving out of research on biomineralization, a new field devoted to studying the interactions between inorganic materials and proteins is emerging. In natural systems proteins are responsible for the assembly of complex hierarchical structures such as the nacre of abalone. Tools such as phage and yeast display libraries have enabled the combinatorial screening of peptides against a multitude of materials to which natural systems typically have no exposure. These techniques have yielded peptides that can bind and assemble technologically relevant materials such as gold and CdS. In this work, combinatorial phage and yeast display libraries are used to identify peptide sequences that bind to electrode materials and metal oxides. As in nature it is observed that the context of a particular peptide dramatically influences its properties. While a peptide sequence may exhibit good adhesion to a particular surface when displayed on yeast, the same peptide may have little affinity towards that same surface when displayed on bacteriophage. To probe the interactions between peptides and materials in a context-free environment, rationally designed synthetic peptides were screened against a number of inorganic materials. A synthetic peptide covalently linked to either microspheres, quantum dots, or a polymer, was able to mediate adhesion of those entities to electrode surfaces. In nature, proteins play important roles beyond biomineralization. For example membrane proteins contain voltage-gated ion channels that open and close in response to a voltage bias. Inspired by the electro-responsive activity of ion channels, the interactions between peptides, surfaces and electric fields was investigated. The peptide sequences that exhibited significant adhesion to metal oxides were dominated by positively charged residues. A high voltage, pulsed electric field was used to overcome the inherent negative charge of the metal oxide electrode surface, thereby controlling peptide adhesion to an electrode surface. Drawing further inspiration from the way nature employs peptides, a synthetic photocatalytic system for water oxidation was developed using photosystem II (PSII) as a model. Proteins form the structural scaffold for PSII, assembling dye molecules as well as the metal-oxo catalytic center; furthermore, peptides play an active role in shuttling charge throughout PSII. The D1 peptide in PSII is an electro-responsive peptide of sorts, releasing plastoquinone upon the two electron reduction of the molecule. The system developed in this work uses: iridium oxide as a metal-oxo catalyst assembled by a peptide expressed on the M13 bacteriophage; metalloporphyrin photosensitizers that are covalently assembled on the protein framework of the bacteriophage and a synthetic Ce(IV)

15. SUBJECT TERMS

16. SECURITY CLASSIFICATION OF:

a. REPORT
unclassified

b. ABSTRACT
unclassified

c. THIS PAGE
unclassified

17. LIMITATION OF
ABSTRACT

**Same as
Report (SAR)**

18. NUMBER
OF PAGES

202

19a. NAME OF
RESPONSIBLE PERSON

Biologically inspired materials for electro-responsive coatings and the photo-oxidation of water.

by

Andrew P. Magyar

Submitted to the Department of Material Science and Engineering
on November 5, 2009, in partial fulfillment of the
requirements for the degree of
Doctor of Philosophy

Abstract

Evolving out of research on biomineralization, a new field devoted to studying the interactions between inorganic materials and proteins is emerging. In natural systems, proteins are responsible for the assembly of complex hierarchical structures such as the nacre of abalone. Tools such as phage and yeast display libraries have enabled the combinatorial screening of peptides against a multitude of materials to which natural systems typically have no exposure. These techniques have yielded peptides that can bind and assemble technologically relevant materials such as gold and CdS. In this work, combinatorial phage and yeast display libraries are used to identify peptide sequences that bind to electrode materials and metal oxides. As in nature, it is observed that the context of a particular peptide dramatically influences its properties. While a peptide sequence may exhibit good adhesion to a particular surface when displayed on yeast, the same peptide may have little affinity towards that same surface when displayed on bacteriophage. To probe the interactions between peptides and materials in a context-free environment, rationally designed synthetic peptides were screened against a number of inorganic materials. A synthetic peptide, covalently linked to either microspheres, quantum dots, or a polymer, was able to mediate adhesion of those entities to electrode surfaces.

In nature, proteins play important roles beyond biomineralization. For example, membrane proteins contain voltage-gated ion channels that open and close in response to a voltage bias. Inspired by the electro-responsive activity of ion channels, the interactions between peptides, surfaces and electric fields was investigated. The peptide sequences that exhibited significant adhesion to metal oxides were dominated by positively charged residues. A high voltage, pulsed electric field was used to overcome the inherent negative charge of the metal oxide electrode surface, thereby controlling peptide adhesion to an electrode surface.

Drawing further inspiration from the way nature employs peptides, a synthetic photocatalytic system for water oxidation was developed using photosystem II (PSII) as a model. Proteins form the structural scaffold for PSII, assembling dye molecules as well as the metal-oxo catalytic center; furthermore, peptides play an active role in

shuttling charge throughout PSII. The D1 peptide in PSII is an electro-responsive peptide of sorts, releasing plastoquinone upon the two electron reduction of the molecule. The system developed in this work uses: iridium oxide as a metal-oxo catalyst assembled by a peptide expressed on the M13 bacteriophage; metalloporphyrin photosensitizers that are covalently assembled on the protein framework of the bacteriophage; and a synthetic Ce(IV) dipicolinate electron accepting molecule. The electron accepting molecule, developed to fill the role of plastoquinone in PSII, is believed to be the first non-sacrificial electron acceptor capable of driving the metalloporphyrin-sensitized photocatalytic oxidation of water.

Thesis Supervisor: Angela M. Belcher

Title: Germeshausen Professor of Materials Science and Engineering and Biological Engineering

Acknowledgments

I thank my advisor, Professor Angela Belcher for her support and mentoring. I joined Angie's lab at MIT near its infancy, giving me the opportunity to be part of the evolution of her work. The research in her lab shifted primary focus from biologically mediated assembly of nanowires to ways in which biology can improve systems with real world applicability such as batteries, solar cells, and photocatalysis. As I struggled to find a project that I truly felt passionate about, Angie encouraged and empowered me to keep trying new ideas. With her help, I was able to develop my thesis studies of photocatalytic water splitting. I am grateful to my other committee members, Professor Michael Rubner and Professor Donald Sadoway, who have helped me navigate MIT and have provided me with sound scientific judgement during my time here. My first experience with research at a big university was in Prof. Rubner's lab as an undergraduate working on $[\text{Ru}(\text{bpy})_3]^{2+}$ -based light-emitting devices. The summer I spent working in his lab inspired me to change fields from physics to materials science and to attend MIT. Entering MIT as a first year graduate student, barely knowing what material science was, I was assigned to TA Prof. Sadoway's 3.091 class. From his lectures and by teaching my students in recitation, I learned about Bravais lattices, phase diagrams, and many other topics that proved invaluable during my graduate career.

Ms. Shanying Cui began working with me as a UROP student during her freshman year and was a part of nearly every piece of this thesis. Throughout the thesis I try to acknowledge data that was acquired or analyzed by someone other than myself; however, Shanying and I worked so closely on every aspect of this work it was impossible to know where to give her credit. Shanying's insights, perspectives, and humor have been greatly appreciated. Much of the early work in this thesis was performed in collaboration with Dr. Eric Krauland. Eric taught me yeast display and his wisdom and insight concerning the interactions between peptides and surfaces helped motivate much of the work in Chapters 2 and 3 of this thesis. Mr. Yoon Sung Nam has played a very important role in the water photooxidation portion of this

thesis. The water splitting project was conceived in collaboration with Yoon Sung and he performed a majority of the experiments for the hybrid nanowire section of this thesis. My discussions with Yoon Sung have stimulated many exciting ideas and often yielded a deeper understanding of an experiment or of a particular phenomenon.

Dr. Charlene Mello was a great resource for much of my work studying the interactions between peptides and electric fields, providing me with synthetic peptides as well as a enabling access to an Army fluorescence spectrophotometer. Dr. Dong Soo Yun identified the IrOx-binding sequence that stimulated the photocatalytic work in this thesis. He also tirelessly assisted with electron microscopy. Dr. Georg Fantner, Mr. Brian Neltner, and Mr. Mike Tarkanian provided substantial help with electronics and machining. Dr. Peter Mueller provided x-ray crystallographic support for this work. My “thesis buddy,” Dr. Jennifer Hsieh, has been a source of substantial moral and scientific support during our time in the Belcher lab. Upon my arrival in the Belcher lab, Dr. Yu Huang walked me through the techniques involved in phage display. Prof. Evelyn Hu helped with data interpretation. Thanks to Ms. Anne Gorham, Dr. Robert Kennedy, and Dr. Jeff Simpson for NMR training and assistance. Ms. Deborah Pheasant provided training and assistance with DLS and Mr. Tim McClure provided assistance with FTIR.

Mr. Vesal Dini and Dr. Christine Flynn made my graduate life immeasurably easier by making sure the lab ran smoothly, while Michelle Barron and Jared Embelton helped me with all things administrative. Thanks to Monica, Helen and Steve at VWR and John from shipping for going above and beyond the call of duty.

I want to thank the Belcher Lab lunch group which has included over the years: Dr. Beau Peele, Dr. Dan Solis, Dr. Steve Kottman, Dr. Eric Krauland, Dr. Ahmad “Mo” Khalil, Mr. Vesal Dini, Mr. David Gray, Dr. Debadyuti “Rana” Ghosh, Mr. Roberto “Robbie” Barbero, and Mr. Aditya Kohli. These lunches were full of great discussions of science and everything else under the sun. I have had innumerable valuable conversations with the following people: Dr. Saeeda Jaffar, Dr. Kiley Miller, Dr. Kaity Ryan, Dr. Soo-Kwan Lee, Dr. Chung-Yi Chiang, Ms. Julie Norville, Dr. Sreekar Bhaviripudi, Dr. Asher Sinensky, Ms. Youjin Lee, Dr. Jifa Qi, Dr. Mark

Allen, Dr. Ki Tae Nam, Sgt. John Burpo, Dr. Paul Widboom, Ms. Joan Mao, Dr. Rebekah Miller, Ms. Rebecca Ladewski, Dr. Yun Jung Lee, Mr. Forrest Liao, Ms. Elizabeth Wood, Mr. Gaelen Hess, Dr. Kang Xu, Ms. Hyunjung Lee, Ms. Dahyun Oh, Mr. Xiangnan Dang, and the heir to the water-splitting project, Mr. Heechul Park. Special thanks to Dr. Nicholas Orf for proof-reading parts of this thesis.

Outside of the Belcher lab, a special thank-you to Dr. Jerome “Jay” Mettetal and Dr. Kenneth “Kenny” MacLean, my former housemates, scientific sounding boards, and all around good guys.

This work has been funded over the years by ARL, ICB, CMSE, and Eni S.p.A. Thanks to MIT facilities including the DCIF, ISN, CMSE Materials Analysis SEF and CSBi BIF.

In their thesis, most people thank their families for their love, moral support, etc., and of course all this is true for me as well, but I must also thank my parents Elaine and Jim and my brothers John and Paul for their scientific insights and guidance. Particularly, my mother has helped me proofread papers and this thesis as well as help interpret NMR results. My brother, John, has been a valuable resource imparting knowledge about all things inorganic chemistry. Lastly I want to thank my beautiful wife Kendra, who puts up with me everyday and makes me smile even when nothing in lab works with everybody else expecting me to fix it. Our weekend walks and adventures with our little dog Emma provided an excellent respite from all things science.

Contents

1	Introduction	25
1.1	Motivation	25
1.2	Biomineralization	26
1.3	Photosynthesis	28
1.3.1	Light Harvesting Dye Molecules	29
1.3.2	Manganese Reaction Center	31
1.3.3	Quinone Electron Acceptor	34
1.3.4	Protein Framework for Electron Transfer	36
1.4	Scope of Work	37
2	Peptides that Bind to Conducting Surfaces	39
2.1	Summary	39
2.2	Motivation	39
2.3	Methods of Peptide Discovery	41
2.3.1	The M13 Bacteriophage	42
2.3.2	<i>Saccharomyces cerevisiae</i>	45
2.4	Peptide Selection Results	49
2.4.1	Noble Metals: Platinum and Gold	49
2.4.2	Conducting Oxides: Indium Tin Oxide and Aluminum	53
2.4.3	Sapphire	54
2.4.4	The A08 Peptide	60
2.4.5	Differential binding to gold foil and gold films on glass	61
2.5	Synthetic Peptides	62

2.5.1	Peptide synthesis	63
2.5.2	Binding rules for A08-derived peptides to different materials .	64
2.5.3	Peptide Binding Rules	67
2.5.4	Dissociation Constant, A08 to Aluminum	69
2.6	Synthetic Peptides as Binding Mediators	72
2.6.1	Microspheres	72
2.6.2	Quantum Dots	74
2.6.3	A08-Conjugated Polymer	76
3	Peptide-based electro-responsive materials	79
3.1	Summary	79
3.2	Motivation	80
3.2.1	Electric Fields in Natural Systems	81
3.2.2	Electroactive Monolayers	81
3.2.3	Peptide Based Electro-responsive Materials	83
3.3	Theory	83
3.3.1	Overcoming Electrolysis of Water	85
3.3.2	High voltage phenomena	85
3.4	Experimental Setup For Electrical Experiments	86
3.5	Bio-panning with Electrochemical Elution Pressure	87
3.5.1	Phage Survivability	90
3.5.2	Phage and Yeast Screening with Electrical Elution	90
3.6	Electrically Controlling A08 Peptide Binding to Aluminum	92
3.7	Bipolar Electrode - Electrically Removing Yeast From Sapphire . . .	96
3.8	Removal of 2K1-MBP from ITO	99
3.9	Future Directions	100
4	Photocatalytic Water Oxidation	101
4.1	Summary	101
4.2	Porphyrin-Sensitized, Iridium-Oxide-Catalyzed Water Oxidation . . .	102
4.2.1	Review of porphyrin/metal oxide photooxidation of water. . .	102

4.2.2	Mechanism of Porphyrin/Iridium Oxide Catalytic Water Oxidation	104
4.3	Methods for Iridium Oxide Synthesis	106
4.3.1	Electroporation	106
4.3.2	Chemical Synthesis	113
4.4	Methods for Continuously Quantifying Oxygen Production	116
4.4.1	Electrochemical Oxygen Detection	116
4.4.2	Luminescent Oxygen Measurement	117
4.4.3	Zirconium Based Gaseous Oxygen Analyzer	119
4.5	Multi-scalar Framework For Oxygen Evolution	122
4.5.1	Porphyrin/IrOx Nanowires	122
4.5.2	Oxygen Evolution from IrOx/ZnD630-9 Nanowires	124
4.5.3	Quantum Yield	127
4.5.4	Microgels	127
4.6	The IrOx Peptide	129
4.6.1	Characterization of the IrOx Binding Peptide	129
4.6.2	Peptide Mutants	136
4.6.3	Oxygen Evolution Data	137
4.7	Development of a Non-Sacrificial Electron Acceptor	140
4.7.1	Currently Used Non-sacrificial Electron Acceptors	141
4.7.2	Identifying Promising Electron Accepting Materials	141
4.7.3	Cerium(IV) Chelate Complexes	142
4.7.4	Other Electron Acceptor Candidates.	152
4.8	Future Directions	154
4.8.1	Light harvesting	154
4.8.2	Catalyst	155
4.8.3	Peptide	156
4.8.4	Electron Acceptors	156
4.8.5	Hydrogen	157

A	Phage Display Protocols	159
A.1	Solutions and Media for Phage Display	159
A.1.1	LB Medium	159
A.1.2	Agarose Top	159
A.1.3	TBS	159
A.1.4	TBS-Tween	160
A.1.5	PEG/NaCl	160
A.1.6	Glycine-HCl	160
A.1.7	Tris-HCl	161
A.1.8	Preparation of LB/IPTG/TET plates	161
A.1.9	Strain Maintenance	161
A.2	Phage Display	162
A.2.1	Biopanning - Round 1	162
A.2.2	Biopanning - Subsequent Rounds	162
A.2.3	Titering	163
A.2.4	Amplification	164
A.2.5	Amplification of Clones for Sequencing	165
A.3	Phage display against the A, C, and R faces of sapphire.	165
A.4	pVIII Library Selection against IrO ₂ powder	165
B	Peptide Sequences	167
B.1	Copper	167
B.2	Sapphire Peptide Sequences	167
B.3	Additional peptide sequences	169
C	Experimental Procedures	175
C.1	Conjugation of peptides to Amino Qdots	175
C.2	Procedure for assembling Qdots on an aluminum substrate.	176
C.3	Conjugation of peptide to p(HEMA-co-MAA)	177
C.4	Conjugation of peptide to carboxylate microspheres.	177
C.5	Cleaning Sapphire	178

C.6	Patterning and Cleaning of ITO Substrates.	179
C.7	Modification of Biorad Electroporator to enable continuous pulses . .	179
C.8	Conditions for IrOx NP and NW synthesis using the stirred high voltage pulse cell.	180
C.9	Conditions for oxygen evolution experiment with electro-pulse synthe- sized nanoparticles.	180
C.10	Procedure for the Chemical Synthesis of IrOx nanoparticles. Adapted from [40]	181
C.11	Recipe for Oxygen Evolution Buffer	181
C.12	Data collection from the ZrO2000 Oxygen Analyzer	182
C.13	Inductively Coupled Plasma - Atomic Emission Spectroscopy	182
C.14	Conditions for oxygen evolution with hybrid IrOx/Porphyrin Nanowires	183
C.15	Synthesis of Ce(III) and Ce(IV) dipic	183
C.16	Synthesis of Ce(IV)DTPA	184
C.17	X-ray crystallographic characterization of Ce(IV) dipic	184
C.18	Conditions for NMR analysis of Ce dipic	184
C.19	Conditions for oxygen evolution experiments involving cerium chelates	188
C.20	Experimental Methods for Electrochemical Oxidation of Ce(III) dipic.	188
C.20.1	Three Electrode Setup	188
C.20.2	Redox Flow Cell	189
C.20.3	Absorbance, Calculation of Ce(III) to Ce(IV) conversion. . . .	189

List of Figures

1-1	Abalone uses proteins to self-assemble multi-scaled ordered structures. (A) An image showing the macroscopic structure of an abalone shell. (B) An SEM image showing the stacked plate morphology of the nacre of abalone, SEM image by Angela Belcher. (C) The nucleation and growth of crystalline CaCO_3 by abalone proteins, from [8]. (D) The peptide responsible for CaCO_3 nucleation by abalone, PDB 1L3Q [116].	27
1-2	The solar irradiation spectrum at air mass 1.5 (ASTM G173-03) overlaid by the absorption spectrum of green plants [46].	29
1-3	The arrangement of chlorophyll pigment molecules in PSII, rendering of PDB 1S5L [35] with UCSF Chimera [86].	30
1-4	Reprinted from [109]. A schematic of the Mn_4Ca catalytic core of PSII shown with putative ligands from the electron density.	32
1-5	Reprinted from [28]. The Kok cycle, updated to show the alternating removal of protons and electrons from the Mn catalytic complex. The nine intermediate states of the Mn complex are denoted as $\text{S}_i^{+/n}$ -states where the subscript gives the number of accumulated oxidizing equivalents and the superscript indicates the relative charge. States enclosed by a rectangle are stable for tens of seconds. The illumination of any of these semi-stable states yields a tyrosine cation radical, T_Z^+	33

1-6	Reprinted from [106]. A schematic drawing of PSII showing the transfer of electrons from the catalytic Mn center to Q_b , an electron transporting plastoquinone molecule. D1 and D2 are the core proteins of the PSII reaction center and LHC-II are the PSII light harvesting complexes. The electrons are transported from the Mn_4Ca complex to the T_z tyrosine residue (Tyr), continuing to the P680 reaction center chlorophyll, a pheophytin molecule (Phe) and then to a bound plastoquinone Q_a . The electron is transported via an iron redox intermediate to plastoquinone Q_b which, after two reduction cycles, is released into the thylakoid membrane and subsequently replaced by an oxidized plastoquinone (PQ) enabling the cycle to start over.	35
2-1	The M13 bacteriophage.	43
2-2	A schematic of the bio-panning procedure used to identify material-selective peptides. The material of interest is incubated with the peptide library (either phage or yeast), non-binding clones are rinsed away, binders are either acid eluted and then amplified or directly amplified off of the material surface, and using this subset of binding clones, the process is repeated 3-5 times.	46
2-3	Structure of a yeast cell and the display of peptides on the yeast surface. Aga1 and Aga2 are proteins through which the peptide insert is expressed. HA is the hemagglutinin antibody used to measure peptide expression rates.	48
2-4	The chemical nature of peptide sequences with affinities towards each face of sapphire. This graph displays the enrichment of groups of chemically similar amino acids in sequences isolated from late round screens versus the original library.	57
2-5	The enhanced probability of peptides from the sapphire mini-library binding to each face of sapphire.	58

2-6	The yeast-displayed A08 peptide has “universal” material binding characteristics, exhibiting binding affinity towards metals, semiconductors and insulating material surfaces.	61
2-7	Differential binding of A08, H6, and C6 yeast to gold film and foil. . .	63
2-8	Adhesion of the A08 peptide to a number of commercially relevant materials.	66
2-9	The relative adhesion of synthetic peptides to ITO and aluminum substrates.	70
2-10	Rate of removal of the A08 peptide from an aluminum substrate. . . .	71
2-11	Optical microscope images of unmodified (A) and A08 (B) microspheres bound to gold. (C) The relationship between esterification and microsphere adhesion.	74
2-12	(A) Image of fluorescence from A08-Qdots bound to an aluminum substrate. The inset shows fluorescence from aluminum incubated with un-modified Qdots. (B) AFM images taken by Shanying Cui of the A08 and un-modified Qdots on the aluminum surface.	75
2-13	Results of adhesion test of pHEMA-co-MAA (top) and A08-modified pHEMA-co-MAA to aluminum-coated slides (bottom).	77
3-1	Addressable deposition and release of peptides from an electrode array could improve controlled drug delivery. Material-specific, electro-responsive peptides would make this type of application a reality. . .	80
3-2	A Bio-Rad Micropulser electroporator was used for pulsed field experiments. This power supply produces an kV amplitude exponentially decaying voltage signal.	87
3-3	A system for producing arbitrary, high voltage pulses. The Trek high voltage amplifier increases the voltage waveform produced by the Tektronix function generator by a factor of 1000.	88

3-4	Phage/Yeast display screening procedure employed to identify peptide sequences that exhibit electro-responsive behavior on a particular material surface.	89
3-5	Fluorescence micrographs showing the pulsed electric field driven removal of the A08 from a positively biased electrode and the transfer of the peptide to the negatively biased electrode.	93
3-6	The effect of reversing the potential after peptide has been released from the positive electrode and transferred to the negative electrode. The ability to reversibly transfer the peptide between electrodes differentiates this system from the bacterial adhesion system described by Poortinga et al. [88].	94
3-7	The influence of potential magnitude on the pulsed-field removal and transport of the A08 peptides in electroporation cuvettes.	95
3-8	The number of 2.5 kV pulses required to transport the A08 peptide between electrodes.	95
3-9	The number of 2.5 kV pulses required to transport the A08 peptide between electrodes.	97
3-10	A simulation of field induced charge on a sapphire substrate.	98
3-11	Yeast removal from a sapphire bipolar electrode by applying -5 kV electric field pulses.	98
3-12	Result of applying different electric potentials to MBP-2K1 bound to ITO.	99

4-1	Photocatalysis of water with an IrOx colloid catalyst and porphyrin photosensitizer. The cycle on the right shows the absorption of light by the porphyrin (1), transfer of an electron to persulfate (2), and subsequent creation of a porphyrin radical cation (3). Also shown is the secondary pathway for creation of the radical cation through porphyrin oxidation by the persulfate radical anion (2b). The cycle on the left shows the accumulation of 4 OH residues on the catalyst surface and subsequent release of oxygen. Each step of the left cycle requires the product of the right hand cycle (3).	105
4-2	TEM images of (A) a single IrO ₂ nanowire, (B) a HRTEM closeup showing the crystalline structure of the nanowire, and (C) EDX mapping showing the distribution of Ir and O atoms on the phage surface. TEM image A by Y. S. Nam and images B and C by D. S. Yun. . . .	110
4-3	The oxygen production from IrOx colloids synthesized with and without a PEG capping molecule. Measured using the ZrO2000 analyzer, described in Section 4.4.3.	115
4-4	The Hach LDO dissolved oxygen probe, with the fiber lamp used to illuminate the sample.	118
4-5	Oxygen evolution from IrOx and ZnTSPP measured using the Hach dissolved oxygen probe.	118
4-6	Oxygen was collected from samples by a stream of nitrogen and quantified using a gaseous oxygen analyzer.	121
4-7	(a) Absorbance and (b) fluorescence of ZnD630-9 and ZnD630-9 conjugated to the M13 bacteriophage.	123
4-8	(a) Negatively-stained porphyrin nanowires, (b) 1:15 IrOx:ZnD630-9 nanowires, and 1:224 IrOx:ZnD630-9 nanowires. TEM images by Y. S. Nam	124

4-9	(a) Total oxygen production for IrOx with ZnD630-9 (black), IrOx mixed with wild type ZnD630-9-conjugated viruses (blue), virus-templated IrOx nanowires with ZnD630-9 (green), and ZnD630-9/IrOx hybrid nanowires (red). (b) Total oxygen production from IrOx/ZnD630-9 hybrid nanowires with different IrOx:ZnD630-9 ratios: 15 (red), 41 (black), 74 (blue), and 224 (green). The TON is recorded above each curve.	126
4-10	Hybrid IrOx/ZnD630-9 nanowires before and after oxygen evolution. (10 hours)	127
4-11	An ordered array of polymer microgels.	128
4-12	(a) Turnover numbers from encapsulated hybrid nanowires with two different IrOx:ZnD630-9 concentrations. (b) Relative oxygen production upon multiple cycles of catalytic microgel regeneration.	129
4-13	A 1D NMR spectrum of the IrOx-binding peptide, KGGG-AGETQQAM. Peaks have been assigned using 2D-gCOSY NMR, Figure 4-14.	131
4-14	The 2D g-COSY spectrum of the IrOx-binding peptide, KGGG-AGETQQAM.	131
4-15	An overlay of the 1D NMR spectra of the IrOx-binding peptide, IrOx colloid and mixed colloid and peptide. The mixed spectrum suggests a downfield shift of the methionine residue.	132
4-16	Through-space interactions of the IrOx Peptide, measured using gROESY 2D-NMR spectroscopy.	133
4-17	Through-space interactions in the combined IrOx-binding peptide / IrOx colloid system, measured using gROESY 2D-NMR spectroscopy.	134
4-18	FTIR spectra of the IrOx colloid, PEG-capped IrOx colloid, IrOx Peptide/Colloid complex and IrOx-binding peptide.	135
4-19	HPLC of the IrOx colloid coordinated to the IrOx-binding peptide at different ratios.	136
4-20	Oxygen production from IrOx - peptide - porphyrin complexes using ZnD630-9 (L) and ZnPPIX (R) peptides.	138

4-21	Oxygen production from peptides with containing different linker sequences. Oxygen concentration was normalized to that of a simultaneously run K-GGG-IrOx sample.	139
4-22	(A) A crystal of Ce(III) dipic. (B) A crystal of Ce(IV) dipic.	143
4-23	Absorbance of Ce(III) dipic, Ce(IV) dipic, and Ce(IV) DTPA.	144
4-24	Thermal ellipsoid drawing (50% probability level) of the crystal structure of Ce(IV) dipic. Hydrogen atoms, sodium ions and water molecules omitted for clarity. X-ray crystallography by P. Mueller.	145
4-25	NMR spectra of Ce(III) dipic and Ce(IV) dipic dissolved in D ₂ O, shown before and after addition of iridium oxide colloid. The broadening observed for the Ce(III) dipic sample is an effect often seen for organic molecules coupled to paramagnetic species. After IrOx addition the NMR plot of Ce(IV) shows a small peak at about 10.5 ppm, the position of the Ce(III) dipic peak. Similarly, after IrOX addition the Ce(III) dipic NMR plot shows a small peak at about 8.2 ppm and 8.4 ppm, the position of the Ce(IV) dipic peak. These small peaks are expanded above. Expansion of Ce(III) and Ce(IV) dipic prior to IrOx addition did reveal any peaks.	147
4-26	Cyclic voltammetry of cerium complexes, measured using a three electrode setup with a glassy carbon working, platinum counter, and Ag/AgCl reference. (A) Ce(III) dipic, (B) Ce(IV) dipic, (C) Dipicolinic acid neutralized with NaOH. (D) Ce(IV) DTPA.	148
4-27	Oxygen evolution using Ce(III) and Ce(IV) dipic, Ce(IV) DTPA, or persulfate electron acceptors.	149
4-28	Oxygen evolution across a wide pH range using Ce(IV) dipic as an electron acceptor.	150
4-29	Electrochemical conversion of Ce(III) dipic to Ce(IV) dipic, showing time course of conversion using a three electrode setup at 1 V and an electrochemical flow cell at 3.5 V. Ce(IV) concentration quantified by absorbance at 294 nm.	151

4-30	A diagram of the two compartment flow cell (Electroanalytica) used to convert Ce(III) to Ce(IV). Image by S. Cui.	152
4-31	A comparison of oxygen produced from regenerated Ce(IV) dipic versus Ce(III) dipic and fresh Ce(IV) dipic.	153
4-32	Comparing the absorbance spectra of the ZnD630-9 nanowires and dual porphyrin nanowires.	155
B-1	The enhanced or reduced probability of observing an amino acid with a particular chemical composition at each position of the pIII peptide insert in sequences selected from the A, C and R faces of sapphire. . .	168
C-1	Thermal ellipsoid representation at the 50% probability level of all non-hydrogen atoms contained in the asymmetric unit in the structure of Ce(IV) dipic. Hydrogen atoms are omitted for clarity. X-ray crystallography by P. Mueller.	185
C-2	Ball-and-stick representation of the three-dimensional supramolecular framework of Ce(IV) dipic supported by 12 crystallographically independent hydrogen bonds (dashed lines). Hydrogen atoms bound to carbon were omitted and carbon atoms were drawn with zero-radius for clarity. Color codes for the atom types are as in Figure C-1. X-ray crystallography by P. Mueller.	186
C-3	Absorbance calibration for Ce(IV) dipic concentration.	190
C-4	Absorbance of Ce dipic solution during electrochemical conversion of Ce(III) to Ce(IV) dipic using a electrochemical flow cell.	191

List of Tables

2.1	Peptide sequences that exhibit an affinity for platinum or gold	50
2.2	Peptide sequences that exhibit an affinity for ITO or Aluminum. . . .	53
2.3	Peptide sequences from screens versus each face of sapphire.	56
2.4	Sequences selected for inclusion in the mini-library for screening against each face of sapphire.	58
2.5	Binding of A08 Variants to Glass and Aluminum.	67
2.6	Peptides designed to study the role of charge spacing on metal oxide binding. The column "Net charge" is the average charge of the peptide at neutral pH.	68
2.7	Zeta potential measurements of microspheres.	73
2.8	Zeta potential measurements of microspheres after esterification. . . .	73
3.1	Phage survivability in an electric field with no current flow.	90
4.1	The conditions for synthesizing IrO ₂ nanoparticles using electric pulses. The TEM image was taken by D. S. Yun.	109
4.2	Diagrams of (A) the cylindrical flow cell designed for continuous pro- duction and (B) the stirred cell for larger batch production of IrO ₂ nanoparticles using HV electropulses.	112
4.3	Comparing the dissolved oxygen produced from electro-pulse synthe- sized nanoparticles with ZnTSPP in the dark and when illuminated. .	112
4.4	Dialysis of IrOx Colloids using differing MW cutoff dialysis tubing. .	115
4.5	TON and TOR	125

4.6	The computationally determined radii of gyration and distance between linker and binding pocket for IrOx-binding peptides with different linker sequences.	137
A.1	Titer on sapphire, Phage, pfu/ μ L	165
B.1	Sequences selected from the A, C and R faces of sapphire using the 12-mer pIII library.	169
B.2	Sequences selected for platinum using the 12-mer phage library. . . .	169
B.3	Sequences selected for ITO using the C7C phage library (samples 1 and 2).	170
B.4	Sequences selected for ITO using the C7C phage library (samples 3 and 4).	171
B.5	Sequences selected for aluminum using the C7C pIII phage library. . .	172
B.6	Sequences selected for aluminum using the 12-mer pIII phage library.	173
C.1	Crystal data and structure refinement for 09014.	187

Chapter 1

Introduction

1.1 Motivation

Amino acids are the functional building blocks of biological systems, each amino acid imparting specific functionalities which in concert enable complex processes such as biomineralization and photosynthesis. Crucial to each of these processes are the interactions between amino acids and inorganic species. Proteins drive the formation of numerous biologically-derived inorganic structures including bone, egg shell, teeth and the shells of mollusks. In photosynthesis, both the assembly of the catalytic center and the precise positioning of light-harvesting molecules are controlled by proteins. Beyond simply serving as a structural scaffold, photosystem proteins play a dynamic role in photosynthesis by facilitating charge transfer between active sites.

The synthesis of a multi-functional chemical compound can take months or years to design, potentially requiring many steps, low yields, and toxic organic conditions. The rich chemical diversity of amino acids enables the design or discovery of multi-functional peptides, while modern peptide synthesis enables the facile synthesis of these compounds. New synthetic amino acids promise to even further extend the functionalities of synthetic materials constructed using peptide bonds. Simply examining how individual amino acids are used by natural systems provides numerous ideas for the utilization of peptides in synthetic systems. Potential applications of peptides include enhancing electron transport, promoting crystal growth, and facili-

tating charge gradients.

1.2 Biomineralization

One of the fundamental tenets of theoretical computer science is that even the most complex computational processes can be reduced to a simple set of rules known as a Turing Machine. The biological-mediated assembly of complex hierarchical structures such as nacre of abalone originates from a similarly simple template. At the atomic scale, calcium carbonate is nucleated by a protein that is secreted by abalone. The protein controls the crystal phase of calcium carbonate that is formed [8]. The abalone nacre is made up of stacked plates that are ordered on a length scale much greater than that of a single protein, and on the macroscale, the shells of mollusks exhibit a further level of ordering. Much like a Turing Machine, a complex, ordered structure arises out of a simple set of rules: the amino acid sequence that controls CaCO_3 nucleation.

Natural systems have a limited set of available raw materials. Beyond the biomineralization of CaCO_3 , diatoms form highly ordered SiO_2 based structures and some bacteria nucleate magnetic iron based nanoparticles used for navigation, but few other inorganic materials are nanostructurally assembled in naturally occurring biological systems. Using combinatorial phage display libraries, Belcher and coworkers identified peptide sequences that could bind to inorganic materials not found in nature, such as GaAs, InP, and Si.[105]. Furthermore, sequences identified using phage display were able to mediate the assembly of crystalline nanowires of materials such as ZnS, CdS, CoPt, and FePt [63, 67]. Biologically templated inorganic nanowires enabled the construction of devices such as batteries, with active electrode materials nucleated on bacteriophage scaffolds [81].

In this thesis, the principles of biomineralization are used to study the interactions between peptides and inorganic materials. Experiments studying electrically responsive materials and photocatalytic water-splitting are not traditionally the realm of biomineralization. Principles developed from the study of interactions between pep-

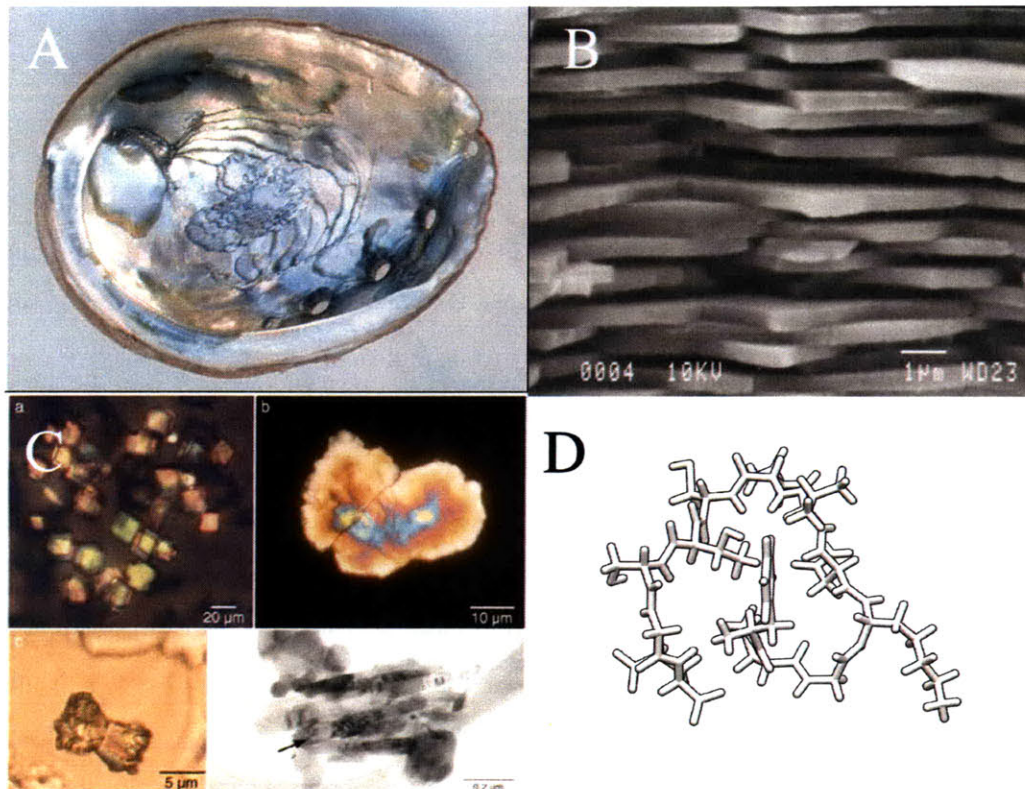


Figure 1-1: Abalone uses proteins to self-assemble multi-scaled ordered structures. (A) An image showing the macroscopic structure of an abalone shell. (B) An SEM image showing the stacked plate morphology of the nacre of abalone, SEM image by Angela Belcher. (C) The nucleation and growth of crystalline CaCO₃ by abalone proteins, from [8]. (D) The peptide responsible for CaCO₃ nucleation by abalone, PDB 1L3Q [116].

tides and inorganic materials are employed to better understand the underlying role of peptides in the water-splitting and electro-responsive systems.

1.3 Photosynthesis

Photosynthesis is one of the most complex natural processes, utilizing highly optimized, multi-scalar structures to convert sunlight, water, and CO_2 into chemical energy in the form of sugars. In eukaryotic organisms the structures that enable photosynthesis are ordered hierarchically. At a molecular level, dye molecules and catalytic metal ions are precisely positioned in four protein matrices that are structurally optimized to promote efficient electron transfer and energy transduction. The proteins are located across membranes as part of sac-like structures called thylakoids [83]. Thylakoids are encapsulated within chloroplasts, flat disks about $1\text{ }\mu\text{m}$ tall and about $5\text{ }\mu\text{m}$ in diameter. In plants, microfluidic structures play an important role in delivering water and nutrients to photosynthetic cells. This multi-scaled framework protects delicate light harvesting antennae, enables the transport of charge and reactants to reaction centers, and constantly replaces photosynthetic molecules.

At the core of photosynthetic processes is photosystem II (PSII), an assemblage of dye molecules, catalytic metal ions, and proteins that cooperate to photocatalytically oxidize water and separate the resulting charge. The overall efficiency of photosynthesis is similar to that of modern silicon solar cells (10 - 25%) [11], however the efficiency of PSII at absorbing light and creating separated charge is very impressive, more than 95% [11]. The light-harvesting molecules, catalytic reaction center, electron accepting complexes, and framework for charge transfer found in PSII are all crucial features for synthetic schemes for the photo-oxidation of water. In this section, these functional entities from PSII are discussed and related to the components of the catalytic water oxidation system developed in this thesis.

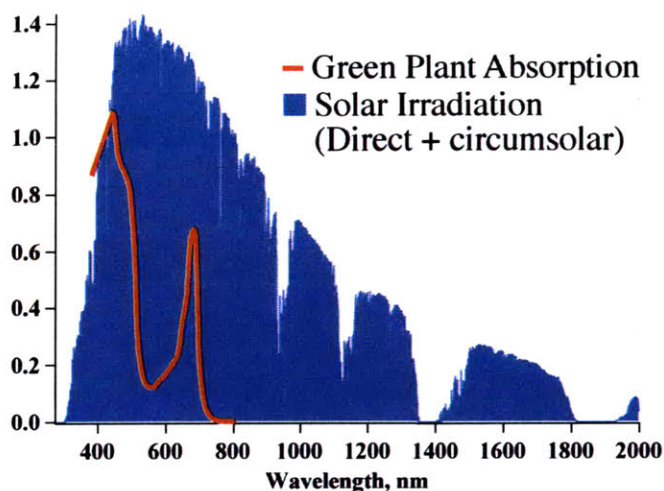


Figure 1-2: The solar irradiation spectrum at air mass 1.5 (ASTM G173-03) overlaid by the absorption spectrum of green plants [46].

1.3.1 Light Harvesting Dye Molecules

More than 200 chlorophyll and around 50 carotenoid molecules are arranged throughout PSII, cooperating to absorb light, convert photons into electric charge, and assist in transferring the charge to a single catalytic reaction center [106]. Chlorophyll, a cyclic tetrapyrrole coordinated to a central manganese ion, is the primary light absorbing molecule while carotenoids, linear polyenes, absorb light in the blue and green region and help protect photosynthetic complexes by quenching the chlorophyll triplet state and by “downregulating” excess light. The absorption of chlorophyll and other dye molecules found in green plants combine to effectively span the solar spectrum, as shown in Figure 1-2. Porphyrin molecules and $[\text{Ru}(\text{bpy})_3]^{2+}$, commonly used dye molecules for synthetic photocatalytic reactions, are similar to chlorophyll: they all contain a central metal cation coordinated via nitrogens to a conjugated ring structure.

The many pigment molecules of PSII are organized in highly ordered structures, as seen in Figure 1-3, enabling them to function cooperatively to focus energy towards the catalytic center, and to overcome overload under high light intensities. The nanoscale separation of the pigment molecules results in strong pigment-pigment

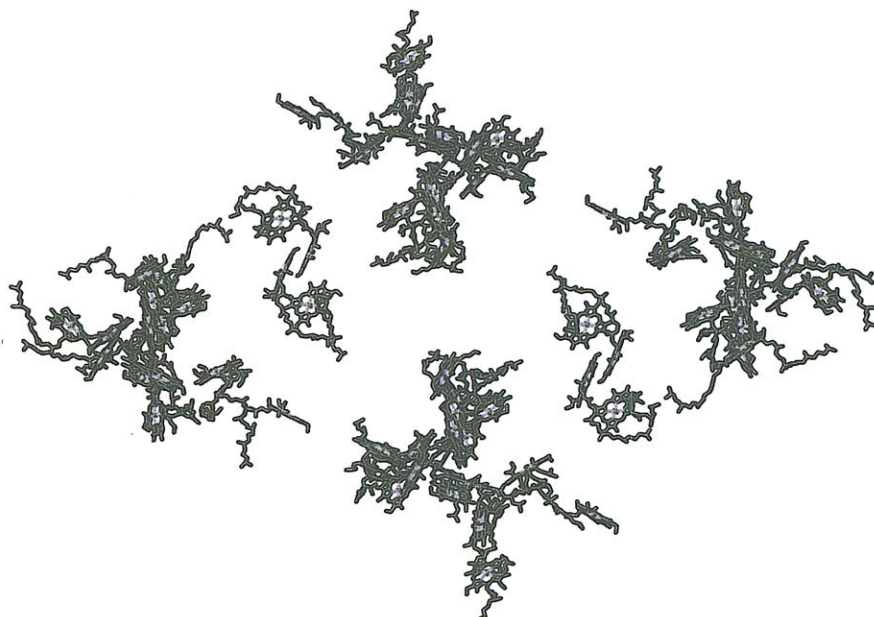


Figure 1-3: The arrangement of chlorophyll pigment molecules in PSII, rendering of PDB 1S5L [35] with UCSF Chimera [86].

interactions enabling delocalization of excited electronic states [21]. Classically, the excitonic coupling between pigments is described using Förster energy transfer [36], a theory of non-radiative exciton transfer by dipole-dipole coupling of allowed transitions. Recent work indicates that the Förster theory for exciton transfer is inadequate because the compact packing of dyes within photosynthetic complexes results in the breakdown of the point-dipole approximation [21]. Modifications to Förster's theory to account for excitonic delocalization [50] and correlated fluctuations between donor and acceptor modes [49] provides a more precise description of multichromophoric systems but cannot account for a critical component of energy transfer in pigment-protein complexes such as PSII: coherence [21]. Engel et al. showed that quantum coherence plays an important role in energy transfer in photosynthetic systems [33]. Quantum phenomena may explain the very high efficiency of photosynthesis at converting light to electronic energy. Wavelike behavior of excited states would allow phase space sampling to identify the most efficient pathway for energy transfer [33]. Theories describing coherent phenomena in pigment-protein systems are in their in-

fancy. Aspuru-Guzik and coworkers have developed models of environment-assisted quantum transfer [91, 74] that suggest that interactions between free Hamilton evolution and thermal fluctuations in the environment lead to significant increases in energy transfer efficiency for the Fenna-Matthews-Olson pigment-protein complex [74]. A better theoretical understanding of the quantum aspects of energy transfer in PSII could enable rationally designed light-harvesting antennae for solar energy harvesting applications.

In this work, the chlorophyll-like zinc porphyrins are co-assembled with catalyst nanoparticles on the surface of bacteriophage, with the idea that the ordered bacteriophage template and nanoscale spacing of pigment molecules may improve light harvesting efficiency of the zinc porphyrins.

1.3.2 Manganese Reaction Center

The catalytic core of photosynthesis is a complex of four manganese atoms and a calcium atom. This Mn_4Ca complex is the reaction center where the oxygen-oxygen bond is created, yielding molecular oxygen. The Mn are connected by mono- μ -oxo, di- μ -oxo, and/or hydroxo bridges. High resolution structures suggest that eight amino acids coordinate to the metal ions in the Mn_4Ca complex [109], shown in Figure 1-4. These ligands likely play a role both in stabilizing the Mn_4Ca complex and in the redox chemistry of the catalytic reaction.

While recent high resolution structures have provided a clearer physical picture of the Mn_4Ca complex, a definitive picture of the coordinating ligands, the exact nature of the oxo-bridges between Mn, and the location of water molecules and protons is not yet possible. The precise chemical processes that occur in Mn_4Ca oxygen generation are not yet fully understood, however Kok and coworkers developed the generally accepted model for the catalytic cycle. Illumination of PSII-complexes with flashes of light results in a period of four appearing in the yield of dioxygen, with the most O_2 appearing after the third, seventh, and eleventh pulse [58]. The “S-state” model explains this periodic behavior by proposing that the catalytic reaction is a four step process with each quantum of energy inducing an increasingly oxidized

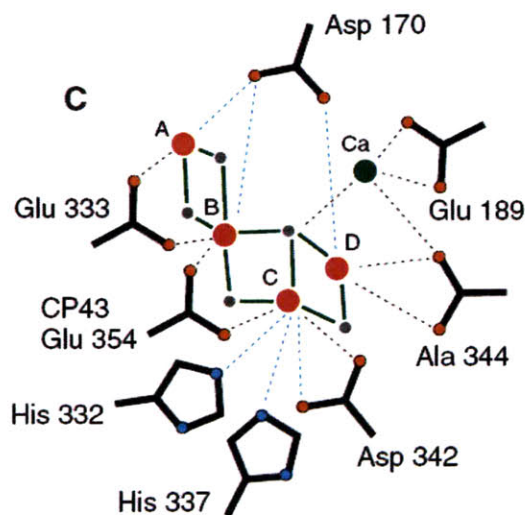


Figure 1-4: Reprinted from [109]. A schematic of the Mn_4Ca catalytic core of PSII shown with putative ligands from the electron density.

state of a trapping center, since identified as the Mn_4Ca reaction center. Figure 1-5 shows a modern revision to the Kok cycle including the proposed removal of protons and electrons from the Mn complex [28]. While many of the features of the Kok Cycle have been confirmed, such as the four quanta requirement for water oxidation, much is still unknown about the exact mechanism of the catalytic reaction. Despite much speculation [10, 28], the exact oxidation state of each Mn, the nature of the oxo-bridges, and much more at each step of the Kok Cycle remains unknown.

Manganese is a natural choice for PSII to utilize as the basis for its catalytic reactions [2]. Mn can exist in each cationic state from +2 to +7, with redox states above +2 all strongly oxidizing under certain conditions. The rich redox chemistry and stability of Mn compounds with water and oxygen enable the removal of multiple electrons and protons that is required during water oxidation [2]. While other elements are suitable catalytically for water oxidation, none are as abundant as Mn, the third most abundant transition metal in the earth's crust. In spite of the advantages of Mn for catalysis, it is remarkable that nature has evolved an efficient complex for water oxidation using Mn, as both the +2 and +5 oxidation states are unstable. Furthermore, the precise structure of the Mn reaction center, appears to

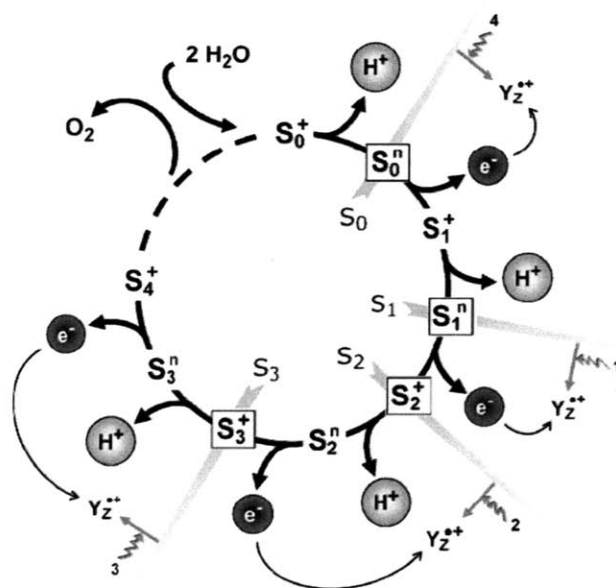


Figure 1-5: Reprinted from [28]. The Kok cycle, updated to show the alternating removal of protons and electrons from the Mn catalytic complex. The nine intermediate states of the Mn complex are denoted as $S_i^{+/n}$ -states where the subscript gives the number of accumulated oxidizing equivalents and the superscript indicates the relative charge. States enclosed by a rectangle are stable for tens of seconds. The illumination of any of these semi-stable states yields a tyrosine cation radical, T_Z^+ .

be very important to its catalytic activity, demonstrated by the limited success of synthetic attempts to replicate the catalytic performance of the Mn reaction center [77]. Researchers have demonstrated catalytic oxygen production using manganese complexes, however, these complexes are used with oxygen-transfer oxidants such as H_2O_2 to facilitate molecular oxygen formation [62]. A complete understanding of the Mn_4Ca complex, including the role of specific PSII amino acids in mediating electron transfer as well as the structure and stability of the complex, and the precise description of the Kok cycle, including the structure and oxidation states of the Mn_4Ca complex at each step, could be the only route to cheap, efficient, Mn-oxo complexes that can catalyze dioxygen production from water.

In this work, iridium was selected in place of manganese as the catalytic centerpiece for water oxidation. While Ir is very rare, making it impractical for the catalytic activities of natural systems or for most commercial applications, the well studied catalytic activity of synthetic iridium oxide clusters [40, 79, 78, 75] makes it a suitable choice for studying the interactions between peptides and catalytic metal-oxo clusters. Iridium, like manganese, exists in a number of different oxidation states and the proposed mechanism for the catalytic activity of iridium oxide clusters, detailed in Section 4.2.2, is similar to the Kok cycle mechanism of PSII. As in PSII, where the Mn-oxo complex is assembled by the protein framework, iridium oxide (IrOx) was co-assembled with dye molecules on the M13 bacteriophage using an IrOx-specific peptide. The catalytic performance of this structure was compared to that of uncoupled IrOx colloidal clusters.

1.3.3 Quinone Electron Acceptor

The electrons and protons removed from water by the Mn_4Ca reaction center are transferred through PSII to drive the reduction of plastoquinone to plastoquinol. Plastoquinol plays an important role in photosynthesis, carrying electrons and protons across the thylakoid membrane to the transmembrane cytochrome b_6f for the subsequent transfer of electrons to PSI and generation of a proton gradient by cytochrome b_6f . PSII contains two quinone molecules, the irreversibly bound Q_a , and the mobile

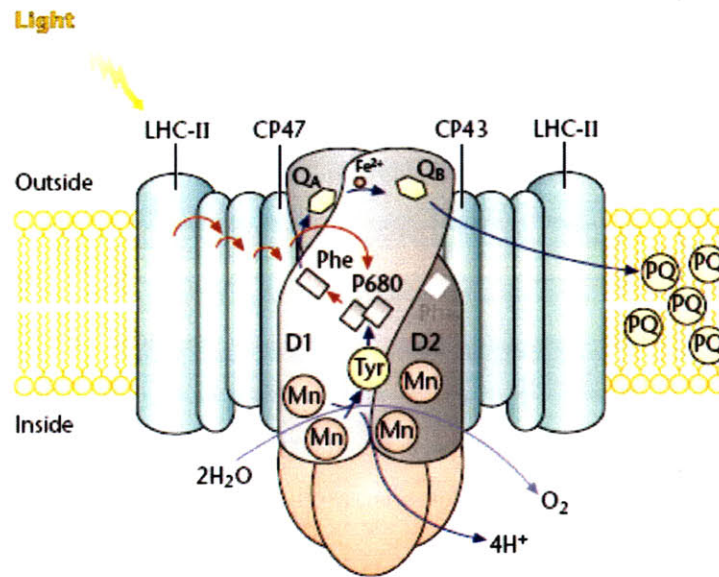


Figure 1-6: Reprinted from [106]. A schematic drawing of PSII showing the transfer of electrons from the catalytic Mn center to Q_b , an electron transporting plastoquinone molecule. D1 and D2 are the core proteins of the PSII reaction center and LHC-II are the PSII light harvesting complexes. The electrons are transported from the Mn_4Ca complex to the T_z tyrosine residue (Tyr), continuing to the P680 reaction center chlorophyll, a pheophytin molecule (Phe) and then to a bound plastoquinone Q_a . The electron is transported via an iron redox intermediate to plastoquinone Q_b which, after two reduction cycles, is released into the thylakoid membrane and subsequently replaced by an oxidized plastoquinone (PQ) enabling the cycle to start over.

Q_b [106]. Binding pockets of the D2 and D1 polypeptides of PSII immobilize Q_a and Q_b respectively [56]. As charge is removed from water by the Mn_4Ca reaction center it is transported via an electron transfer chain to Q_a and to Q_b . Figure 1-6 shows the path taken by electrons as they are transported from the Mn catalytic center to Q_b . After Q_b has been fully reduced by the addition of two electrons and two protons, the D1 binding pocket no longer presents affinity towards Q_b and the molecule is released into the thylakoid membrane. The transmembrane region contains a bath of oxidized plastoquinone molecules that can bind to the Q_b , enabling the process to be repeated. For each O_2 molecule created, two Q_b molecules undergo complete reduction, corresponding to the 4 electrons extracted from water to form the dioxygen bond.

In synthetic, colloidal systems for the photo-oxidation of water, mobile electron acceptors are an important component, filling the role Q_b serves in PSII by removing electrons from the catalytically active site, thereby enabling additional cycles to take place. Many studies of photo-oxidation use electron sinks, employing sacrificial electron acceptors, such as the persulfate anion [72]. The use of a sacrificial electron acceptor enables studies of a catalytic half reaction, but inhibits the future coupling between any resultant oxidative catalytic process and a corresponding reductive half-reaction. In this work, a non-sacrificial electron acceptor based on a Ce(IV) dipicolinate complex is synthesized and its utility as an electron-accepting complex for photo-oxidative applications is demonstrated.

1.3.4 Protein Framework for Electron Transfer

As described above, the protein framework of PSII plays many roles, promoting coherent exciton transfer, assembling the Mn_4Ca complex, facilitating the redox responsive binding and release of Q_b , and facilitating electron transfer processes. Beyond providing a pathway for electron transfer, aromatic amino acids can promote unidirectional energy transfer, thereby inhibiting undesirable back reactions [54].

The dielectric environment that results from the protein framework is crucial to determining electron transfer pathways. Boxer and coworkers studied the functionally asymmetric electron pathways of the bacterial photosynthetic reaction center. The reaction center contains two nearly structurally equivalent electron transfer pathways, though electron transfer only occurs via one of the pathways. Stark spectroscopy reveals that the active pathway has substantially higher dielectric strength than the non-active pathway, suggesting that the collective properties of the amino acids near the electron transfer pathways explain the functional asymmetry [100]. Through the modification of about 14 amino acids, Boxer and coworkers restored the electron transfer capabilities of the non-functioning pathway [26].

In this work, peptides designed to link iridium oxide clusters and porphyrin molecules are synthesized containing different spacer groups to study whether a short peptide sequence can facilitate enhanced electron transfer between porphyrin and

catalyst.

1.4 Scope of Work

This thesis focuses on interactions between peptides and inorganic materials and, in particular, ways to facilitate functionality that extends beyond biomineralization. Using material-binding peptides as a starting point, new electroresponsive coatings and a new framework for photocatalytic water oxidation were developed. Paramount to future applications is understanding the specific role of peptides in a particular material system. For each of the systems described in this thesis, the nature of the peptide's role in either driving adhesion, imparting electro-responsive behavior, or promoting electron transfer is examined.

Chapter 2 focuses on the identification of peptides that bind to electrode surfaces and development of rules for peptide adhesion to metal-oxide surfaces. The binding to metal oxides is predominantly driven by electrostatics. In Chapter 3 this electrostatic binding mechanism is exploited through the use of electric fields to overcome the interactions between a charged peptide and metal oxide electrode yielding an electrically reversible peptide coating. A new framework for photocatalytic water oxidation is presented in Chapter 4. At the core of this framework is a metal-oxide binding peptide that mediates the assembly of the catalytic material.

Chapter 2

Peptides that Bind to Conducting Surfaces

2.1 Summary

A massively parallel combinatorial approach utilizing phage and yeast display libraries is employed to discover peptides that bind to conducting substrates including gold, platinum, aluminum and ITO. It is observed that positive charge is common to many of these peptides, likely due to the negatively charged oxide layer that found on most of these materials in water. The binding characteristics of a highly positively charged, synthetic “universal binder” peptide, termed AO8, is explored. By observing the binding behavior of mutations of this “universal binder” some insight is provided into its binding mechanism. Lastly, carbodiimide chemistry is used to couple the AO8 peptide to a polymer, quantum dots, and microspheres to show that peptides can be used to facilitate binding to conducting surfaces.

2.2 Motivation

Controlling the adhesion of bio-molecules to conducting surfaces is valuable for applications including sensors, drug delivery, anti-microbial coatings, and other electronic technologies. It has been shown that short peptide sequences can assemble and nu-

create numerous inorganic materials. The aim of this work is to discover peptide sequences that can bind to metal or other conducting surfaces. Combinatorial techniques using phage or yeast display libraries are powerful tools to discover peptide sequences with affinity towards a particular material. The specifics of these two techniques and their respective advantages and disadvantages are discussed in this chapter.

Context is critically important to interactions between peptides and inorganic surfaces. While a phage-displayed peptide may exhibit a certain material affinity, the same peptide sequence on yeast may behave completely differently. This is evidenced by examining the peptide “binding rules” for a variety of materials established by Peele et al. for yeast displayed peptides [84] and by Willett et al. for poly-amino acids [108]. The results of Peele et al. indicate that histidine, particularly, up-regulates peptide binding to gold while Willett et al. observe no such effects. Perhaps the negatively charged yeast surface influences peptide structure in a manner that the histidine is more apt to interact with the material surface. Irrespective of the cause, these results make it clear that while display library techniques provide a starting point for discovering peptide sequences that can be used as linker molecules, studies must be performed to understand the interactions of “free” peptides with metal surfaces.

In this section, phage and yeast display are used to discover peptide sequences that exhibit binding affinity towards conducting surfaces. One sequence selected from a yeast surface display library in a screen against CdS by Eric Krauland, RSGRRRSH-HHRL, exhibits a particularly broad binding affinity towards metals and metal oxides [60]. To examine binding properties of peptides in a template free environment, the A08 and several mutants were prepared synthetically. The ability of the A08 peptide to serve as a linker between different materials and metal surfaces was demonstrated by coupling the peptide to microspheres, quantum dots, and a polymer.

2.3 Methods of Peptide Discovery

Using recombinant DNA technology, peptide sequences can be expressed on the surface of biological entities such as phage and yeast. This technique can be extended to create peptide display libraries containing on the order of 10^9 phage or 10^6 yeast each expressing different peptide sequences. Display libraries were first used to screen antibodies against biomedical targets of pharmaceutical interest with such success that companies such as New England Biolabs developed, producing tools for phage display including libraries of phage expressing short peptide sequences.

Inspired by biomineralization peptides found in nature, Whaley et al. used a commercially available phage display library to discover peptides that bind to semiconductor materials not commonly found in nature [105]. Peele et al. constructed peptide libraries on yeast and demonstrated that yeast display can also be used to discover peptides with an affinity towards a particular inorganic material [85, 84]. Some of these peptides are able to promote biomineralization; incubating inorganic precursors together with phage or yeast that express material selective peptides, it is possible to nucleate quantum dots [63], nanoparticles [64], and microshells [34].

The process of selecting material binding from a display library is iterative - downselecting peptides from an initially diverse library over several rounds of screening under increasingly stringent conditions. The library is exposed to the material of interest in a buffer, often containing a detergent or bovine serum albumin to minimize non-specific interactions, and incubated to allow different peptides to sample the surface. Weak binders are removed by rinsing and the remaining clones are amplified and the process repeated for several rounds until a consensus sequence is isolated or trends can be determined from the peptide sequences. While evolutionary processes tend to be quite slow, this combinatorial approach rapidly identifies peptides with unique material affinities.

2.3.1 The M13 Bacteriophage

Bacteriophage Structure

The M13 virus is a filamentous bacteriophage (Ff) belonging to the family Inoviridae. M13 bacteriophage has a quite high aspect ratio; it is about 900 nm long and about 6.5 nm in diameter. The virus capsid is formed by five proteins that assemble around the phage genomic DNA, a 6400 nucleotide, single stranded, covalently-closed DNA molecule. The major coat of the bacteriophage is formed by 2700 copies of the pVIII protein assembled in an alpha-helix around the ss-DNA. The protein assembly has five-fold rotational symmetry, with the axis of the pVIII protein exhibiting an approximately 20° right-hand tilt with respect to the longitudinal axis of the phage. The assembly of the coat proteins is driven by electrostatic interactions between the negatively-charged sugar-phosphate DNA backbone and four positively charged residues at the C-terminus of the pVIII protein. At the proximal end of the bacteriophage (with respect to *E. coli* attachment) are five copies each of the pIII and pVI proteins, while at the distal end five copies each of pVII and pIX assemble. Figure 2-1 shows a depiction of the M13 bacteriophage.

M13 replicates through the non-lytic infection of *Escherichia coli* (*E. coli*). High density virus amplification is made possible by the non-lytic nature of infection, a crucial factor for phage applications. The pIII peptide enables the attachment of the bacteriophage to the F pilus of the *E. coli* host cell. The phage disassembles and the pVIII proteins and virus DNA enter into the cell cytoplasm. Once in the cell, using the single stranded phage DNA as a template, the bacterial host synthesizes the complementary strand yielding double stranded DNA suitable for replication. The complementary strand is the template for transcription, from which the resultant mRNA molecules are translated into phage proteins. The phage is constructed by assembly proteins and is extruded from the *E. coli* through a pore in the cell membrane.

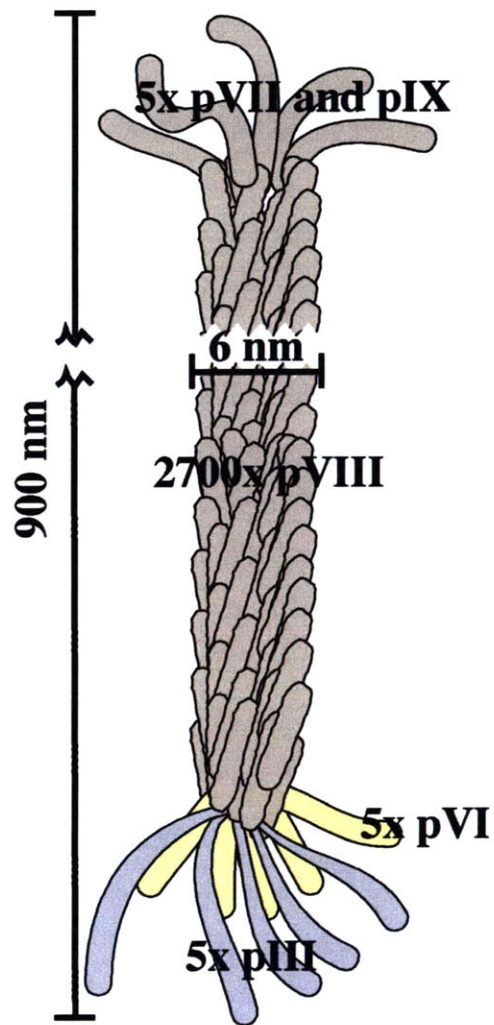


Figure 2-1: The M13 bacteriophage.

Phage Display

Through modifications to the bacteriophage genome, peptides can be inserted into the M13 coat proteins. Peptides have been inserted into the pIII, pVIII, and pIX proteins. On the pVIII protein only short peptides, 6 to 8 amino acids, can be expressed genomically. Furthermore, sequences that can disrupt phage assembly, particularly those that are highly positively charged are not able to be inserted into the pVIII. On the pIII, longer sequences can be inserted and more diversity is possible; some sequences can influence the phage's ability to infect *E. coli*, slowing or completely inhibiting phage replication. Multiple peptide sequences or larger proteins can be expressed using phagemid DNA. Phagemid DNA is a plasmid inserted into the host *E. coli* encoding for the phage protein plus insert. The *E. coli* produces the phage protein and upon infection by a "helper phage" the insert containing proteins are randomly co-incorporated into the phage capsid along with wild type phage proteins. With phagemid system, the complete genome of the bacteriophage is no longer carried on board the virus preventing self-replication. Additionally, 100% display of the peptide on the phage surface is not possible, particularly with large phagemid inserts.

Phage display libraries, containing many phage each expressing different peptide inserts, have been constructed using both pIII and pVIII display. The pIII libraries exhibit significantly higher diversity and copy number, but because there are only 5 copies of each pIII protein per phage they are not suited for all applications. Three different pIII libraries are available commercially from NEB, a 7-mer library, a 12-mer library, and a 7-mer cysteine constrained library (C7C). The 12-mer linear library and 7-mer constrained library were primarily used in this work. In the 7-mer constrained libraries the peptide insert forms a loop due to the disulfide linkage that is formed between the two cysteine residues. This constraint imparts conformational rigidity to the peptide.

Phage Selection

In this work the 12-mer and C7C NEB pIII libraries were used to identify peptides that are able to bind to an array of inorganic materials. For screening with a phage library a piece of the material of interest $\approx 0.5 \text{ cm} \times 0.5 \text{ cm}$ was cleaned and placed in a small petri dish or in a well plate. The sample was incubated with $\approx 1.5 \times 10^{11}$ virions in a buffer solution for about 1 hour. The unbound phage were rinsed off and the binders either eluted with acid or grown directly off of the surface by placing the sample in E.coli broth. The first round binders were amplified and used for the next round of screening. After several rounds the phage were plated and plaques picked for DNA sequencing. DNA sequencing revealed the peptide sequences that mediate binding to the material of interest. Typically, three to five rounds are sufficient to attain either a consensus binding sequence or to be able to discern recurring patterns in the peptide sequences. Figure 2-2 provides a graphical representation of the selection procedure. The C7C library tends to yield consensus sequences more frequently than the 12-mer library, perhaps due to the increased structural conformity imparted by the constrained geometry. For some materials the short length and lack of flexibility inherent to C7C sequences can inhibit binding. Materials for which charge plays an important role to mediate binding, for instance, may not be well suited for screening with the C7C library. This is evidenced experimentally by an overly rapid collapse of library diversity during early panning rounds. More detailed experimental procedures are included in Appendix A.

2.3.2 *Saccharomyces cerevisiae*

Yeast Structure

Saccharomyces cerevisiae have been utilized as single cell bioreactors for millennia. Critical for baking and brewing, yeast turn sugars into CO_2 or ethanol. More recently yeast has been utilized for biofuel production and antibody discovery. Yeast is a single-celled eukaryote, with spherical cells approximately $4 \mu\text{m}$ in diameter. Like all eukaryotes yeast cells contain a set of subcellular organelles within a cell envelope.

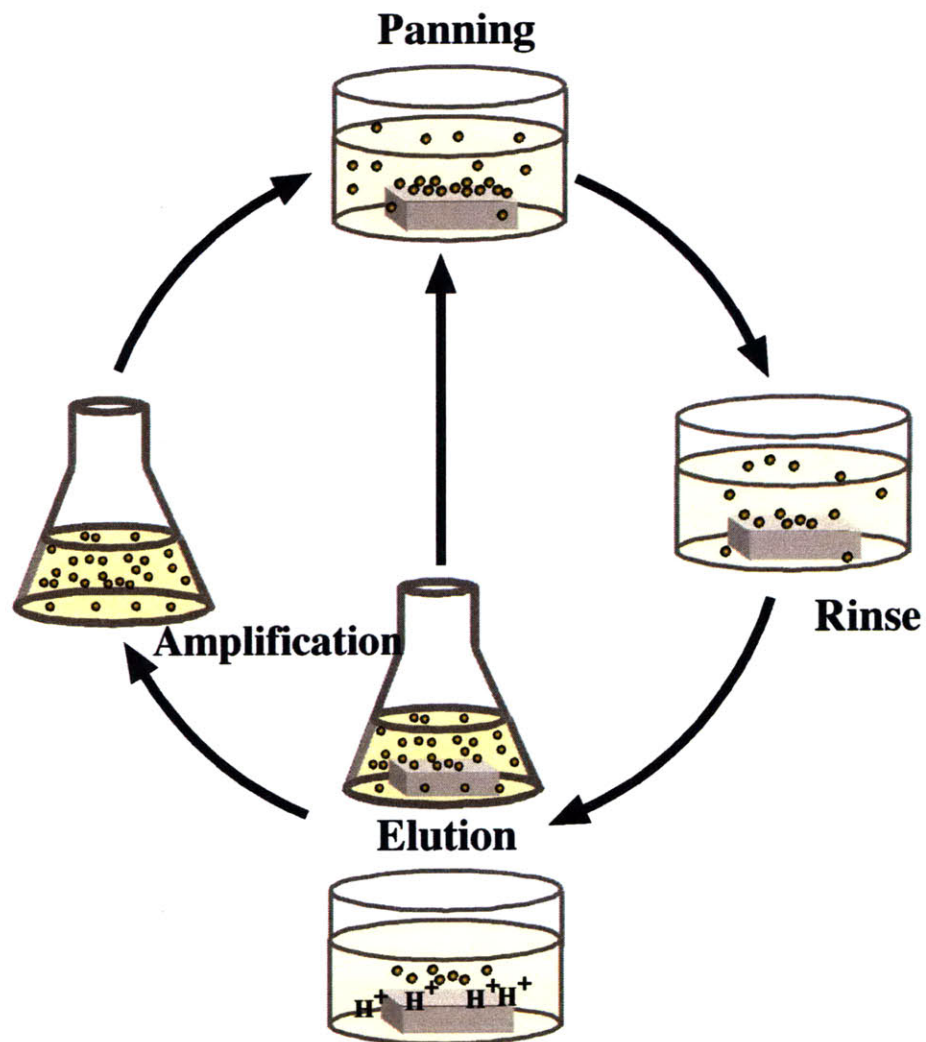


Figure 2-2: A schematic of the bio-panning procedure used to identify material-selective peptides. The material of interest is incubated with the peptide library (either phage or yeast), non-binding clones are rinsed away, binders are either acid eluted and then amplified or directly amplified off of the material surface, and using this subset of binding clones, the process is repeated 3-5 times.

The protective cell envelope is made up of an inner cell membrane and a cell wall. Since this work focuses on interactions between yeast cells and inorganic materials, the properties of the yeast outer surface are important to understand. The outer layers of the cell wall are made primarily of mannoprotein. Mannoproteins are a conglomeration of proteoglycans with varied molecular weight and protein content, though typically the protein content is less than 10%. The carbohydrate moieties of the mannoprotein branch off of the protein components and consequently are the primary groups exposed on the yeast surface. In water these carbohydrate groups are responsible for the yeast's generally negatively charged surface.

Yeast are able to reproduce both sexually and asexually. In nutrient rich media, however, asexual reproduction by yeast budding dominates. Reproduction by yeast budding yields genetically identical offspring - critical for applications of yeast display libraries. Budding initiates with the duplication of the genetic material within the cell as well as an increase in the volume of cellular components. A cell bud forms at actin dots on the cell surface, eventually leading to cytokinesis leaving two fully functional cells.

Yeast Display

Yeast display poses some distinct advantages over phage display. Peptides displayed on yeast are surface expressed and in no way influence the yeast's ability to replicate or grow; this property enables nearly any sequence as well as larger proteins to be expressed on the yeast surface. Additionally, yeast do not require any host cell for reproduction, and yeast cells are easily visible under a light microscope. Antibodies and short peptide sequences can be displayed on the surface of yeast cells as a protein fusion to the Aga2p matting agglutinin protein. The Aga2p protein is disulfide linked to a protein embedded in the cell membrane, Aga1p. Peptide fusion expression is controlled by galactose induction via the GAL1,10 promoter. The strain of yeast used for display, EBY100, is designed with Aga1p expression inducible from a single, integrated open reading frame downstream of the Gal1,10 promoter. The peptide of interest is encoded into the Aga2p protein using the pCT302 plasmid and transformed

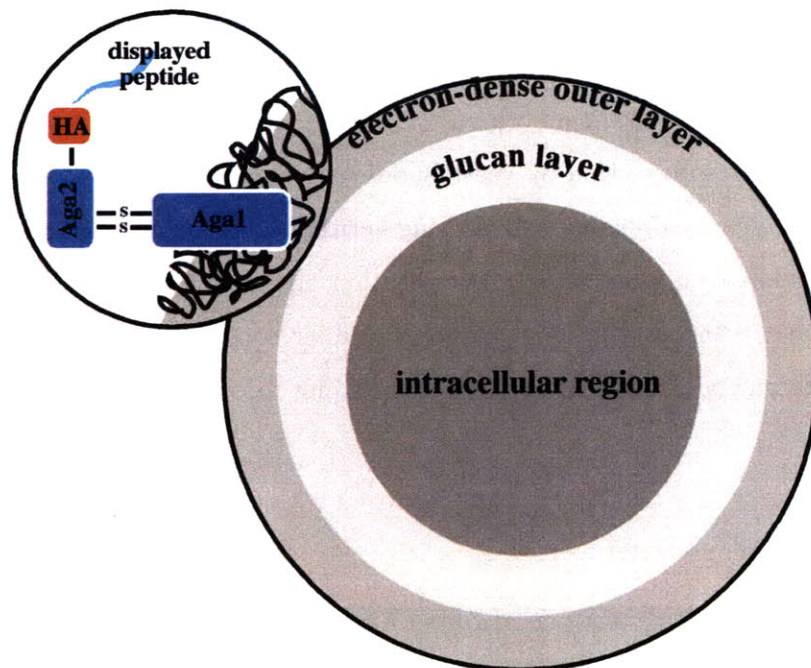


Figure 2-3: Structure of a yeast cell and the display of peptides on the yeast surface. Aga1 and Aga2 are proteins through which the peptide insert is expressed. HA is the hemagglutinin antibody used to measure peptide expression rates.

into the yeast strain. Also on the pCT302 plasmid is the hemagglutinin antigen (HA) antibody. HA can be tagged fluorescently and used as a measure of peptide expression rates. Figure 2-3 depicts the components involved in yeast surface display. Combinatorial yeast display libraries of both antibodies and 12-mer peptides have been created and used for material and antibody selection.

Yeast Selection

For experiments using yeast display libraries to screen against inorganic materials, a 12-mer yeast display library created by Beau Peele and Eric Krauland was used [85]. A yeast library with diversity of approximately 10^7 random 12 amino acid peptide clones was incubated with the material of interest under agitation. Weakly binding cells were removed by surface washing and the sample was imaged to determine overall binding. The adherent cells were grown off of the material surface, serving as a sub-library for further rounds of screening. On subsequent rounds stringency was increased by decreasing the amount of time yeast cells were permitted to interact with the surface and increasing the concentration of Tween20 and BSA to inhibit non specific interactions. Figure 2-2 provides a graphical representation of the selection procedure. The binding peptide sequences were determined by DNA sequencing of the pCT302 plasmid after transforming it into *E. coli*.

2.4 Peptide Selection Results

In this section, the results of screenings against various materials using either phage or yeast display are reported. For each material several sequences from late screening rounds are reported and discussed with respect to the chemical properties of the amino acids in relation to the material surface.

2.4.1 Noble Metals: Platinum and Gold

Though both platinum and gold are often considered too expensive for many applications, they both serve important roles as materials for catalysis and microelectronics.

Platinum	Selection Technique
C P T S T G Q A C	Phage C7C Library, Seker et al.
C M A T S A P R C	Phage C7C Library
R R L L G L S V E F L D	Yeast PL12 Library
S V H G L R H H H V R M	Yeast PL12 Library
W R W G G A P H M D H M	Yeast PL12 Library
R W W L H R L W G A R S	Yeast PL12 Library
R K G C C K R R R R S K	Yeast PL12 Library
Gold	Selection Technique
L K A H L P P S R L P S	Phage 12-mer Library, Nam et al.
V G S S P D S	Phage 7-mer PVIII Chiang et al.
C S L S I G S H C	Phage C7C Library
R M R M K M K	Yeast, Designed by Peele et al.
W R M Q T R R R R H S W	Yeast PL12 Library
W C H R R L C R R H N	Yeast PL12 Library
R P C L R R W W K Q M C	Yeast PL12 Library
Gold and Platinum	Selection Technique
K G W W W L K T G V K P	Yeast PL12 Library
W R W G G A P H M D H M	Yeast PL12 Library

Table 2.1: Peptide sequences that exhibit an affinity for platinum or gold

Nearly every automobile made today contains a catalytic convertor containing platinum as a reduction catalyst. Platinum is also often used as a hydrogen evolving catalyst for electrolysis [53] and photolysis [3, 37] of water. Gold nanostructures can also serve as a catalytic material [12], enable biological imaging [117, 31], and even serve as a therapeutic tool for cancer treatment [103].

Seker et al. reported phage-displayed platinum-binding sequences in 2007 with the cysteine-constrained sequence CPTSTGQAC [93]. Gold nanowires assembled using bacteriophage have been employed for applications including battery electrodes [81] and virus based fibers [22]. The gold binding motif used for those applications had the sequences LKAHLPPSRLPS and VSGSSPDS respectively. Peele et al., in their work examining yeast-displayed sequences of the type XHXHXXH (X is any amino acid) showed significant up-promotion of yeast binding to gold (in reference to X = alanine) by histidine, tryptophan, lysine, methionine, cysteine, arginine, glutamic acid, and tyrosine. Histidine exhibited a nearly seven-fold improvement in binding, while substituting tryptophan, lysine, and methionine each exhibited at least three-fold improvements in binding to gold [84]. Using the binding rules they derived, Peele et al. designed the yeast binding sequence RMRMKMK that exhibits an affinity for gold but not CdS or ZnS [84].

In this work the C7C phage display library (New England Biolabs) was used to select against platinum wire (Alfa Aesar). The platinum wire was first cleaned with 8:7:1 H₂O:HCl:HNO₃, rinsed thoroughly with water and ethanol, and then flame sterilized. A consensus sequence, CMATSAPRC, was reached after three rounds of screening. Some parallels can be drawn between this consensus sequence and that of Seker et al. Each sequence contains a hydrophilic domain at the same position in reference to the disulfide linkage. In their work Seker et al. compare the binding of the constrained version of the peptide CMATSAPRC and the version without cysteine residues. They observe that the constrained peptide exhibits significantly better binding to platinum and argue that this is due to structural considerations [93]. Considering that the consensus sequence reported in this work contains a methionine residue, perhaps the factor leading each of these peptides to exhibit enhanced binding

is actually interactions between the sulfur atoms in both cysteine and methionine and the platinum surface, coupled with interactions by the hydrophilic regime in the middle of the peptide.

The PL12 yeast library was also used to screen for peptides that bind to platinum wire. The platinum wire was cleaned with ethanol and the library incubated with the platinum sample for four hours. BSA was used to block non-specific interactions. Several sequences that resulted from this yeast screening are presented in Table 2.1. The yeast-displayed sequences that bind to platinum contain more positive charge than the phage-displayed sequences. The positive charge may balance the net negative charge of the yeast surface or may cooperate with the negatively charged yeast surface to orient the ring structures of the amino acids histidine and tryptophan to better coordinate with the platinum surface.

A preliminary phage display screening of a gold on silicon substrate was performed using a C7C library. The consensus sequence CSLSIGSHC was isolated after three rounds of screening. Unfortunately this selection was not wholly specific to gold because the library was exposed to both the gold surface and the silicon substrate. This sequence is similar to that reported by Chiang et al. [22] as both are very hydrophilic. The PL12 yeast display library was used to carry out more rigorous selection against gold. Gold coated glass slides (EMF-Corp) were cleaned with concentrated HCl and thoroughly rinsed with water before screening. No consensus sequence was reached from the yeast screening, however three representative sequences from round 5 are shown in Table 2.1. Sequences from other rounds can be found in Appendix B. These gold binding sequences are in good agreement with the bind rules established by Peele et al. [84]. The sequences are highly positively charged, the three sequences are +5.1, +4.1, and +3.9 at pH 7.0, where the screen occurred. Furthermore, the sequences are enriched with tryptophan and cysteine, which Peele et al. indicate up-promotes binding to gold [84].

Indium Tin Oxide												Selection Technique	
C	H	H	N	H	K	K	N	C				Phage C7C Library	
C	K	A	H	T	Q	K	H	C				Phage C7C Library	
C	K	P	H	H	K	T	T	C				Phage C7C Library	
C	H	K	P	H	K	H	W	C				Phage C7C Library	
C	K	P	H	K	M	G	F	C				Phage C7C Library	
Aluminum												Selection Technique	
V	P	S	S	G	P	Q	D	T	R	T	T	Phage 12-mer Library Zuo et al.	
Y	S	P	D	P	R	P	W	S	S	R	Y	Phage 12-mer Library Zuo et al.	
C	T	K	T	L	W	G	S	C				Phage C7C Library	
C	V	A	P	S	R	G	T	C				Phage C7C Library	
C	H	K	S	S	T	T	S	C				Phage C7C Library	
Q	S	N	Y	T	R	Y	I	P	A	S	L	Phage 12-mer Library	
Q	H	A	N	H	Q	A	W	N	N	L	R	Phage 12-mer Library	
S	T	Q	V	S	K	I	H	R	S	P	F	Phage 12-mer Library	
K	K	E	K	R	P	R	K	T	R	K	Y	Yeast PL12 Library	
K	R	C	T	R	T	H	R	H	K	R	K	Yeast PL12 Library	

Table 2.2: Peptide sequences that exhibit an affinity for ITO or Aluminum.

2.4.2 Conducting Oxides: Indium Tin Oxide and Aluminum

Indium tin oxide (ITO) is a transparent, conducting metal oxide, a unique combination of properties that makes ITO commercially indispensable for display production. ITO is more precisely a solid solution of indium oxide and tin oxide typically containing about 9-10% tin oxide. From the perspective of surface chemistry, aluminum is very similar to ITO. Metallic aluminum rapidly forms a several nanometer thick layer of aluminum oxide, yielding a surface that is a mixture of aluminum and oxygen. Without further treatment, both aluminum and ITO have a large number of hydroxyl groups on their surfaces [16, 71], yielding a negatively charged surface in water.

The C7C pIII phage libraries were used to screen for phage that exhibit affinity towards ITO coated glass slides (DCI Inc., gift from Rubner Group). The ITO substrates were cleaned with ethanol and then autoclaved prior to screening. Acid elution was used to elute the bound phage. Screening was carried out multiple times through at least 4 rounds, yielding several different sequences shown in Table 2.2. Each of these sequences contains at least 3 positively charged residues and is particu-

larly enriched with histidine, which appears at least once in each sequence. Additional sequences from other rounds of screening against ITO can be found in Appendix B.

To discover peptide sequences with an affinity for aluminum, the C7C and 12-mer pIII phage libraries and PL12 yeast libraries were screened against aluminum wire or foil (Alfa Aesar). For phage display screening, the aluminum substrate was rinsed with ethanol and water and then autoclaved. Consensus sequences, Table 2.2, that contained hydrophilic amino acids supplemented by positively charged amino acids were observed after 4-5 rounds of screening. Sequences isolated from the 12-mer library exhibited an over-expression of amide-containing amino acids. Both amides and hydrophilic residues can participate in hydrogen bonding interactions with hydroxyl groups on the aluminum surface. These results are consistent with the aluminum binding sequences reported by Zuo et al. in which serine and tyrosine appear to play a critical role in mediating binding [118].

The PL12 yeast display library was screened against pieces of high-purity aluminum foil (Alfa Aesar). The aluminum foil was washed with ethanol and water but not autoclaved, as contamination is not as problematic working with yeast as phage. The sequences isolated after several rounds of screening, shown in Table 2.2 were highly positively charged, some as many as 9 positively charged residues. These highly charged sequences may suggest that the electrostatic forces drive the interaction between the yeast displayed peptides and the aluminum surface. The autoclaving of the aluminum surface may yield a more hydroxylated surface yielding more hydrophilic sequences from phage display, while the native metal oxide is negatively charged in water, resulting in highly positively charged sequences from the yeast display screen.

2.4.3 Sapphire

Sapphire is the single crystal phase of alumina, or $\alpha\text{Al}_2\text{O}_3$. Krauland et al. selected sapphire as a model system to probe the role of peptide sequence in mediating binding to metal oxide materials [61]. In that work, the A, C, and R faces of sapphire were screened using the PL12 yeast display library. In water, the A, C, and R faces exhibit

differing chemical characteristics. The C-face is completely hydrated with doubly coordinated oxygen atoms leading to surface passivated hydroxyl groups that are highly reactive towards metal ions [32]. The R-face is more complex, with a mixture of basic (1-coordinated oxygen atoms) and acidic (3-coordinated oxygen atoms) sites on the surface [19]. The properties of the A-face are expected to be somewhere between that of the C- and R- faces [61]. Krauland et al. found that even yeast without a surface-displayed peptide insert displayed (stop codon) bound to the C-face of sapphire, which they attributed to divalent metal ion bridging between the biomolecules on the cell surface and the oxygen ions on the sapphire surface. On both the A and R faces of sapphire the consensus binding sequences isolated by Krauland et al. are dominated by positively charged residues; compositional analysis of sequences showed an enrichment from 10% positively charged residues in the native library vs. 40% positively charged residues in clones that came from screens versus the A and R faces. After studying a series of designed peptides both displayed on yeast and expressed on maltose binding protein, the final conclusion reached by Krauland et al. was that “spacial matching between peptide and surface charges is not a major mechanism for the observed adhesion” [61]. While Krauland et al. do observe a role of sequence in enhancing binding, they conclude that this is purely a factor of promoting configurations that best expose the positively charged residues to the material surface.

In this work, a 12-mer, pIII phage display library was used to select against the A, C and R faces of sapphire to further probe the hypothesis that the peptide sequence of “consensus clones” for sapphire is driven purely by charge considerations rather than structural features of the sapphire surface. The three different orientations of synthetic sapphire, C-plate (0 0 0 1), A-plate (1 1 -2 0), and R-plate (1 -1 0 2) were obtained from Crystal Systems (Salem, MA). Prior to use, the 0.5 cm x 0.5 cm sapphire substrates were cleaned with hydrochloric acid and ethanol, as detailed in Appendix C.5. Four rounds of screening with increasing stringency were carried out versus each sapphire face. Table 2.3 presents representative sequences selected from each substrate after the forth-round screen. Additional fourth round sequences are included in Appendix B.2. Based on the titer of the eluted phage after one round

Aluminum Oxide, C-Face	Selection Technique
K M R A W G H P I W N W	Yeast PL12 Library, Krauland et al.
T K H G K R S R C Y N L	Yeast PL12 Library, Krauland et al.
L L A D T T H R P W T	Phage 12-mer Library (Also from AI)
K S L S R H D H I H H H	Phage 12-mer Library
T D T P Q S Y G W K T R	Phage 12-mer Library
Aluminum Oxide, A- Face	Selection Technique
R T A K R K W K H T R D	Yeast PL12 Library, Krauland et al. (Both A&R)
M P A V M S S A Q V P R	Phage 12-mer Library
A P R L P Q S L L P Q L	Phage 12-mer Library (Both A&R)
Aluminum Oxide, R- Face	Selection Technique
K R S K K C L R K N G S	Yeast PL12 Library, Krauland et al.
K R H K Q K T S R M G K	Yeast PL12 Library, Krauland et al.
R T A K R K W K H T R D	Yeast PL12 Library, Krauland et al. (Both A&R)
I P W T Q H M A M S P M	Phage 12-mer Library
A P R L P Q S L L P Q L	Phage 12-mer Library (Both A&R)

Table 2.3: Peptide sequences from screens versus each face of sapphire.

of screening, phage binding to each face of sapphire is comparable, suggesting that endogenous binding to the C-face of sapphire, Appendix A.1, is not significant with bacteriophage.

In contrast to yeast display, sequences selected via phage display indicate that binding to sapphire is not mediated simply by positively charged residues. The percentage enrichment of groups of amino acids with similar chemical qualities over the original distribution of the 12-mer pIII library is shown in Figure 2-4. For all three faces of sapphire, positive charge does promote binding, however, aromatic and amide containing residues also figure predominately into the binding signature. Unlike the conclusions of Krauland et al., sequence analysis of clones selected using phage display for the different faces of sapphire suggest that there may be links between the surface structure of the sapphire face and the peptide sequence. Plotting the increased probability versus the library of observing a particular amino acid at a particular location in the peptide insert shows that each face has a slightly different signature. The A and R faces of sapphire are likely to have aliphatic regions at the end of the peptide insert, whereas the C face is more likely to have either positive or aromatic

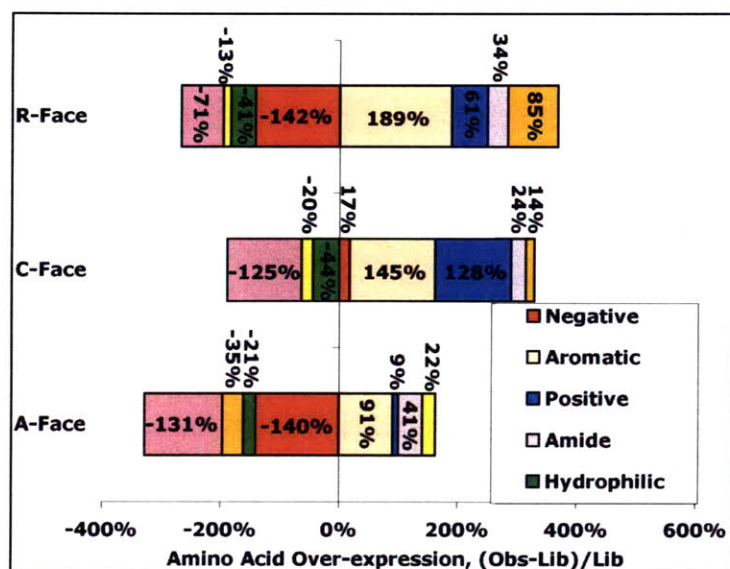


Figure 2-4: The chemical nature of peptide sequences with affinities towards each face of sapphire. This graph displays the enrichment of groups of chemically similar amino acids in sequences isolated from late round screens versus the original library.

residues in this region. Sequences selected versus A- and C-faces have an enhanced probability of negative amino acids near the beginning of the peptide insert, however negatively charged amino acids have a low probability of appearing at any position in sequences selected versus the R-face. For the A-face, particularly, proline has an increased probability at several points along the peptide, which suggests that the peptide structure may play a role in mediating binding to the material surface. The positional analysis graphs of peptide sequences isolated from the A, C and R faces of sapphire are in Appendix B.2, Figure B-1.

To further probe binding interactions between phage-displayed peptides and the different sapphire surfaces, a mini-library was created containing six peptide sequences selected from different faces of sapphire, each selected either because it was isolated multiple times or because of unique chemical characteristics. The six sequences that make up the mini-library are presented in Table 2.4. Sequence C3-4 was isolated from the C-face and also appeared in screens against aluminum metal. Sequence A4-12 was isolated from both the A- and R-face, has a high isoelectric point, and is

Sequence	GRAVY	Neutral Charge	Iso. Point
C3-4 L L A D T T H H R P W T	-0.80	0.2	8
A4-12 A P R L P Q S L L P Q L	-0.01	1	11
A4-11 M P A V M S S A Q V P R	0.25	1	11
C4-31 K S L S R H D H I H H H	-1.76	1.5	10.1
C4-32 T D T P Q S Y G W K T R	-1.88	1	9.7
R4-38 I P W T Q H M A M S P M	-0.03	0.1	7.8

Table 2.4: Sequences selected for inclusion in the mini-library for screening against each face of sapphire.

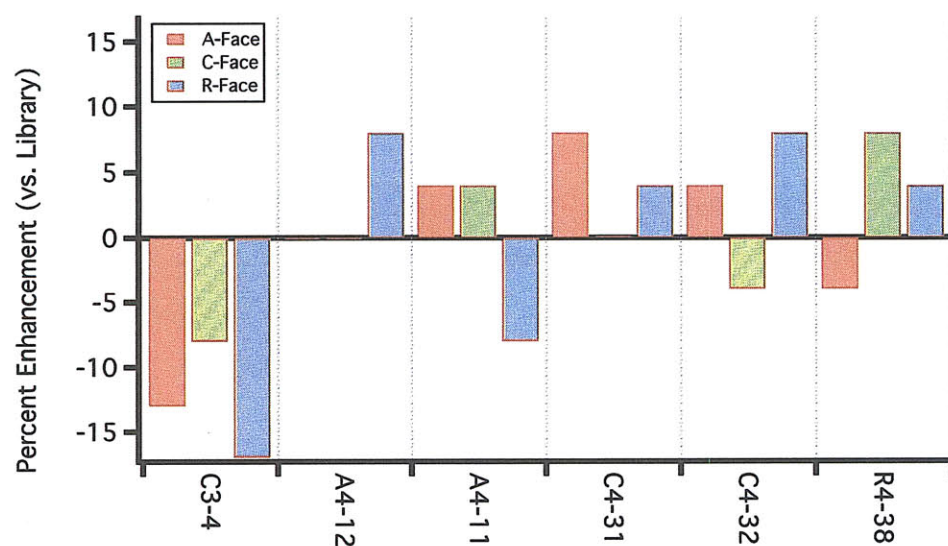


Figure 2-5: The enhanced probability of peptides from the sapphire mini-library binding to each face of sapphire.

aliphatic. Sequence A4-11 was isolated from the A face, has a high isoelectric point, contains methionine residues and is aliphatic. Sequence C4-31 was isolated from the C-face, has a large number of positively charged residues, and a low grand average hydropathicity score (GRAVY). Sequence C4-32 was isolated from the C-face has no aliphatic residues and a low GRAVY. Sequence R4-38 was isolated from the R-face, is hydrophobic, and is enriched with methionine residues. UV-vis absorption was used to normalize the concentrations of each of the sequences when creating the library. Unfortunately, growth biases led to over-representation of sequence C3-4 in the library (63%). The library was screened against the A, C, and R faces of sapphire and 24 clones sequenced from each face. Because of the library bias, sequence frequency was plotted with respect to percent enhancement versus the library, Figure 2-5. Sequence C3-4 appears at lower frequency than it is found in the library for all three sapphire faces, suggesting that while this clone has some affinity for sapphire its recurring appearance may be attributed to accelerated amplification. From the C-face of sapphire, sequences A4-11 and R4-38 both exhibit some enhanced binding. Interestingly, these two clones are both very hydrophobic and contain methionine residues. This result is somewhat surprising given that sulfur-containing residues appear with relatively low frequency from the phage display screen versus the C-face. From the A-face of sapphire, sequences A4-11, C4-31, and C4-32 show some enhancement. These sequences vary dramatically; C4-31 and C4-32 are very hydrophilic while A4-11 is hydrophobic. From the R-face of sapphire, sequences A4-12, C4-31, C4-32, and R4-38 each exhibit some enhanced binding, again these sequences are widely varied in properties.

The result of the mini-library screen illustrates some of the shortfalls of phage display, particularly the idea of “specificity.” Affinities between a particular sequence and the face of sapphire it was selected from exhibited little relation. For example, the sequence that exhibited the most significantly enhanced binding to the A-face was C4-31, a sequence isolated from the C-face. Furthermore, sequence C4-31 exhibited no binding to the C-face of sapphire from the screen. The three bio-panning experiments against each of the faces of sapphire clearly did not yield individual sequences with specificity towards the sapphire face from which the sequence was isolated. Though

true “consensus” sequences were not reached through four rounds of screening, it is unlikely that further rounds of screening would lead to a sequence that matches a particular sapphire surface. Using phage display techniques, with each additional amplification, sequences that bind slightly but amplify well, C3-4 for example, can overtake better binders in late screening rounds. As a result, attaining an individual sequence that is structurally relevant in relation to the surface of interest is difficult when simply using phage display library screening.

Careful examination of the aggregate sequences identified from the phage display screens against each of the faces of sapphire yielded some insight into patterns of binding to the different faces of sapphire. Rigorous studies of rationally designed peptide sequences based on the binding signatures of each sapphire face could yield peptide sequences exhibiting a preferential affinity towards an individual sapphire face. Negative selection screening, a technique that is used to minimize background binding to similar substrates, could be employed in this system. For instance, to identify sequences that had better specificity to the C-face of sapphire, by incubating the library with the A- and R-faces prior to exposing it to the C-face, sequences with affinities towards the A and R face would be removed from the screen. The negative selection technique has proven powerful for applications such as identifying silicon defects in germanium [97]. To identify peptides that exhibit a preferred affinity towards a single face of sapphire, the negative selection approach alone may not suffice because the surfaces are so similar chemically and structurally; but used in combination with rational design peptide sequences, it may be possible to discover peptides that exhibit structural-based preferences towards an individual sapphire face.

2.4.4 The A08 Peptide

The peptide sequence RSGRRRSHHRL, termed A08, was selected from the PL12 yeast display library from a screen against CdS. The A08 sequence is unique, not for its specificity, but for the breadth of materials to which the sequence displays affinity [60]. A08 yeast was screened in collaboration with Eric Krauland against a variety of insulator, semiconductor and conducting materials. The yeast-displayed A08 peptide

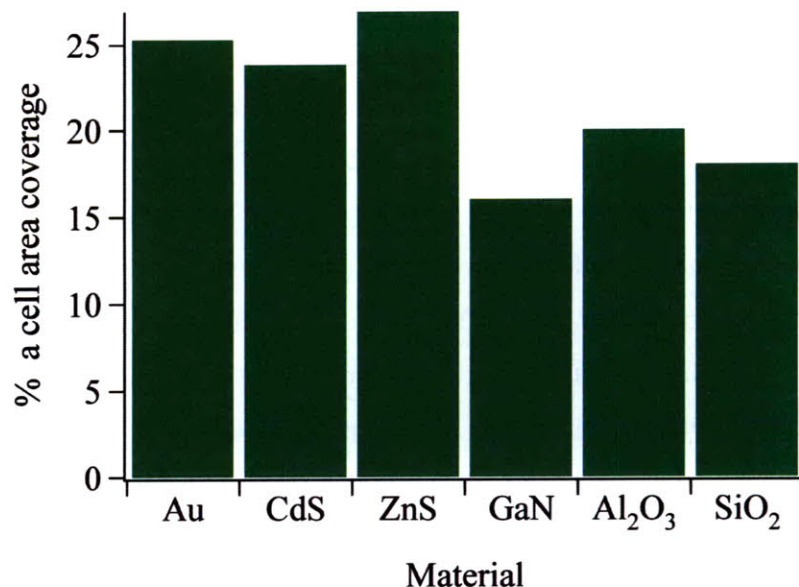


Figure 2-6: The yeast-displayed A08 peptide has “universal” material binding characteristics, exhibiting binding affinity towards metals, semiconductors and insulating material surfaces.

exhibited an affinity towards CdS, ZnS, GaN, Al₂O₃, SiO₂ and gold, Figure 2-6. The binding affinity of yeast-displayed peptides to surfaces is assayed by measuring the percent yeast surface coverage using the optical microscope. The image was processed (ImageJ, NIH) by thresholding the image such that the cells were defined as black and background as white, the percent surface coverage was calculated taken as the percentage of dark pixels. Surface coverages of above about 5% indicate that the yeast clone exhibits some affinity towards the target substrate. The surface coverage of the A08-yeast on each of these materials screened, Figure 2-6, was at least 15%, while the un-induced yeast exhibited little background affinity.

2.4.5 Differential binding to gold foil and gold films on glass

Gold is one of the most non-reactive metals, valued commercially because it does not corrode over time. Considering the inherent stability of gold, the surface properties of different well cleaned gold substrates were expected to be fairly consistent. Three

yeast clones, A08, hexa-histidine (H6), and hexa-cysteine (C6) were interacted with high purity gold foil (Alfa Aesar) and evaporated gold films on glass (EMF-Corp) to compare the gold-binding affinity of the three different peptides. Surprisingly, the binding affinities of the three different peptides differs between the two gold surfaces, Figure 2-7. While all three clones bound well to the gold film on glass, only the C6 clone showed any substantial affinity towards the gold foil, suggestive that the surface properties of the two materials are quite different. The mechanism by which the C6 clone interacts with the gold surface is likely through a thiol-like sulfur-gold bond, which is tenable for either gold surface. A charge-based mechanism is proposed for the interactions between the A08 and H6 peptides and the gold film. The gold film is deposited on SiO_2 , which has a negative surface charge. The negatively charge of the SiO_2 surface will be countered by positive charge at the gold/ SiO_2 interface, leaving an excess of negative charge in the bulk gold. Because gold is such a good conductor, the outer surface is the only place this charge can be readily balanced. Examining water beading on the two gold surfaces it is evident that gold film is more hydrophilic than the gold foil, which is consistent with the gold film having some surface charge. The negative surface charge enhances the binding of both the A08 and H6 yeast to the gold film. The differential binding observed between these two gold substrates suggests that the yeast-displayed peptide binding rules established by Peele et al. for gold, [84] which were assayed based on gold films on glass, may not be broadly applicable to all gold surfaces.

2.5 Synthetic Peptides

Phage-display and yeast-display screening techniques are powerful tools for discovering peptides that possess affinities towards a particular material, and for some applications phage or yeast are suitable templates for material growth to form nano- or micro-structures. Some applications, however, are better suited to peptides that are free of a biological scaffold such as phage or yeast, so that the peptide can be chemically coupled to alternative material frameworks. As described in Section 2.2, peptide

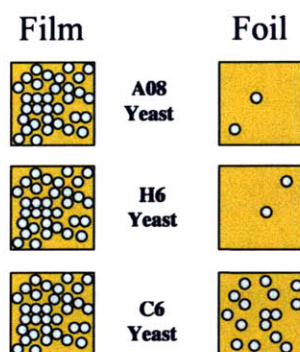


Figure 2-7: Differential binding of A08, H6, and C6 yeast to gold film and foil.

context influences material-peptide interactions, and while a particular residue such as histidine may significantly promote binding to a particular substrate when expressed on yeast, the same residue may minimally influence binding as a "free" peptide. Thus, understanding the interactions between unfettered peptides and a particular material substrate are critical to applications of non-displayed peptides.

2.5.1 Peptide synthesis

In natural systems, peptides are synthesized in the cell by ribosomes, assembling amino acids in a stepwise manner based on the translation of a messenger RNA sequence. This stepwise, translational approach is efficient and highly reproducible, critical features as cells constantly synthesize fresh proteins and when small mutations can inhibit important biological processes such as photosynthesis or cellular respiration. Early in the twentieth century, chemical peptide synthesis was very demanding work, requiring many protection and deprotection reactions and repetitive extractions and purifications to remove secondary products and unreacted precursors [9]. With the "classical approach" for peptide synthesis, low yield and poor purity are major problems, making the chemical synthesis of a biologically active peptide very challenging and the commercialization of such a molecule nearly impossible.

The Nobel Prize work of R. B. Merrifield yielded a solid-phase peptide synthesis technique that enabled high yield, high purity, automated peptide synthesis [69].

Solid-phase peptide synthesis has enabled the construction of peptide libraries for high-throughput pharmaceutical screenings and has enabled bulk peptide synthesis for applications as pedestrian as cosmetics. Merrifield’s revolutionary idea was to build peptides in a stepwise manner with one end of the peptide coupled to a solid support. The covalent linkage of the peptide to an insoluble support during synthesis enabled the rapid removal of any unreacted materials or side products and eliminated the painstaking purification of the final product through crystallization.

Solid state peptide synthesis is a multi-step process, though today the complete process is fully automated. An insoluble polymer matrix is functionalized, enabling the anchoring of the first amino acid. The first amino acid, protected with a blocking group such as tertbutyloxycarbonyl (BOC), is covalently attached to the resin support. The amino acid is deprotected by removing the BOC group and subsequently neutralized. Each additional BOC-protected amino acid is coupled to the growing peptide using carbodiimide or similar chemistries. Finally, the complete peptide is cleaved from the resin [9]. Using modern peptide synthesizers, the purity of some peptides at this point is satisfactory for many applications, requiring only desalting of the peptide. High performance liquid chromatography (HPLC) purification is often used to provide a high purity final product.

In this work, peptides were either prepared by collaborators at the Natick Soldier Center or purchased from the MIT Biopolymers Laboratory, Genscript, or New England Peptide. All peptides were desalted before use and were 85% purity or better.

2.5.2 Binding rules for A08-derived peptides to different materials

The A08 peptide was selected as a model peptide to compare the material binding properties of yeast displayed versus “free” peptides. Because the A08 yeast binds to such a broad array of materials, the A08 peptide could serve as a broadly applicable linker molecule, a kind of single molecule glue, for attaching biomolecules, polymers, or other nanostructures, to inorganic substrates. Binding of the A08 peptide to

numerous inorganic substrates was tested and on aluminum and SiO₂ the binding of the A08 peptide and several mutants thereof were compared.

The A08 peptide was synthesized attached to a tri-glycine linker with an N-terminal lysine. The N-terminal amine is sometimes non-reactive because of incomplete cleavage from the resin; hence, to assure high yield conjugation, the primary amine of the N-terminal lysine is used for chemical linkage reactions. Oregon Green 488 carboxylic acid, succinimidyl ester or similar amine reactive fluorophore molecules were coupled to the A08 peptide to enable visualization of the peptide on material surfaces using a fluorescent microscope.

The fluorescently-labeled A08 peptide was incubated with a number of inorganic materials with properties spanning insulating, semiconducting, and metallic materials. Samples were imaged using the fluorescence microscope. The mean histogram value, correlating to fluorescence intensity, was used as a measure of peptide binding.

As observed for the A08 yeast, the A08 peptide exhibited a binding affinity towards a variety of different materials, Figure 2-8. The A08 peptide bound most strongly to oxide materials including glass, ITO and aluminum. Additionally, the A08 peptide showed a positive affinity towards semiconductors, GaN and CdS, and metals without substantial oxide coatings, brass and stainless steel. Noble metals such as gold and platinum exhibited little to no binding of the A08 peptide, in contrast to the result observed for the A08 yeast. This difference in affinity for gold of the A08 “free” peptide versus A08 yeast suggests that the yeast surface may play a role in orienting the A08 peptide to better enable binding to gold.

The A08 peptide contains a number of both histidine and arginine residues. To determine the role of the nitrogen ring structure of the histidine versus pure electrostatics in promoting binding to oxide materials, mutations of the A08 peptide were synthesized and screened against aluminum, glass, gold, and platinum substrates. Five different peptides were synthesized and screened: two peptides with the histidine residues replaced with either alanine (A08H-A) or arginine (A08H-R), and three peptides with the arginine residues replaced with either alanine (A08R-A), glutamic acid (A08R-E), or glutamine (A08R-Q). Replacing the histidine residues probes the

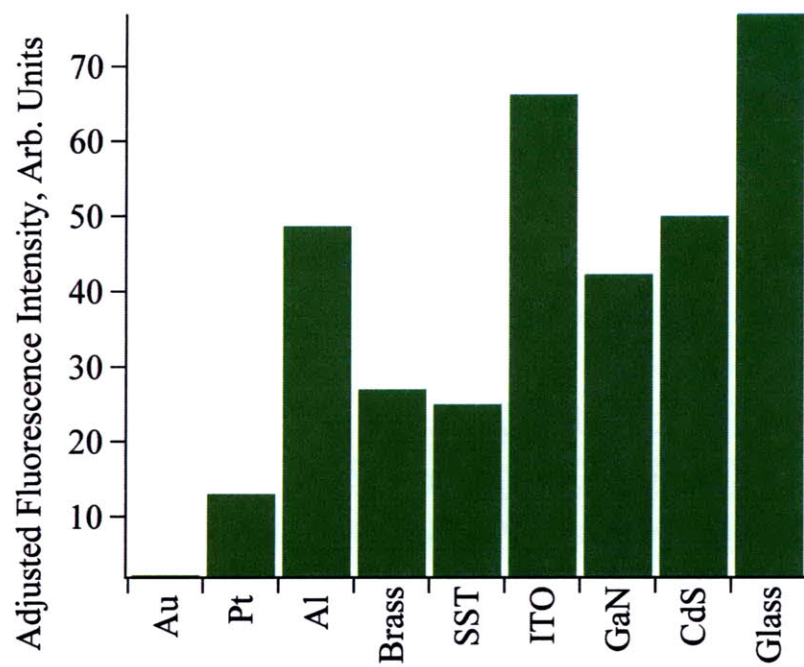


Figure 2-8: Adhesion of the A08 peptide to a number of commercially relevant materials.

Name	Sequence	Al	SiO ₂	Au	Pt
A08	RSGRRRSHHHRL	+++	+++	-	-
A08H-A	RSGRRRSAAARL	++	+++	-	-
A08H-R	RSGRRRSRRRRL	+++	+++	+	+
A08R-E	ESGEEESHHEL	-	-	-	-
A08R-Q	QSGQQQSHHHQL	+	-	-	-
A08R-A	ASGAAASHHHAL	+	-	-	-

Table 2.5: Binding of A08 Variants to Glass and Aluminum.

role of charge in promoting binding, while replacing the arginine probes whether negatively charged residues can still promote binding (A08R-E) or whether nitrogen containing residues can promote binding (A08R-Q).

Table 2.5 shows the different sequences and their respective affinities towards aluminum, glass, platinum and gold. The A08 and A08 H-R peptides are the best binders to both aluminum and glass, indicating that the binding is most likely driven by positive charge. A08H-R is the only peptide showing any affinity towards gold and platinum, suggesting that the peptides interact solely through electrostatics and that the histidine residues in no way enhance binding. A08H-A binds well to aluminum and very well to SiO₂ indicating that the histidine ring plays a minimal role in binding. The lack of significant binding of A08R-Q and A08R-A to either substrate further supports the hypothesis that interactions between the positively charged peptide and negatively charged surface drive the binding of the A08 peptide. The A08R-E peptide exhibits even less binding to aluminum than A08R-A and A08R-Q indicating that the negative charge outweighs the weak interactions between the histidine residues and the aluminum surface.

2.5.3 Peptide Binding Rules

To further probe the role of charge in promoting binding, a number of “rationally-designed”, 12-mer peptides were synthesized to study peptide adhesion on two metal oxide surfaces, ITO and aluminum. These peptides, modeled on sequences studied by Krauland et al. [61], were designed to study the influence of charge spacing as well as

Name	Sequence ^a	Net charge
R12	RRRRRRRRRRRR	+12
H12	HHHHHHHHHHHH	+1.1
AS6	ASASASASASAS	0
AR6	ARARARARARAR	+6
DK6	DKDKDKDKDKDK	0
ER6	ERERERERERER	0
R1	GRGRGRGRGRGR	+6
R2	GRRRGRRRGRRR	+6
R3	GGRRRRGGRRRR	+6
K1	GKGKGKGKGKGK	+6
K2	GGKKGGKKGGKK	+6
K3	GGGKKKGGGKKK	+6

^aEach peptide sequence was synthesized with an N-terminal fluorescein separated from the peptide by a tri-glycine linker.

Table 2.6: Peptides designed to study the role of charge spacing on metal oxide binding. The column “Net charge” is the average charge of the peptide at neutral pH.

the influence of negatively charged or hydrophilic residues on peptide adhesion to the metal oxide surfaces. Krauland et al. engineered yeast to express the peptides R1, R2, R3, K1, K2, or K3 (Table 2.6. Examining the binding of the different yeast clones to sapphire revealed that binding decreased with increasing charge clustering for both the lysine and arginine yeast variants. A mechanism where repulsion forces between adjacent positively charged side chains impedes binding was proposed by Krauland et al. to explain these results [61]. Configurations of peptides containing clustered charge that allow adjacent charged residues to interact with a material substrate are energetically unfavorable. The sequence and net charge of each synthetic peptide is presented in Table 2.6 and the relative binding of each of the peptides to aluminum and ITO is shown in Figure 2-9.

Clustering of lysine residues decreased the affinity of peptides towards ITO, the binding of K3<K2<K1, mirroring the observations made by Krauland et al. On aluminum, clustering of lysine residues also decreases binding, though K2<<K3<K1. The particularly low binding of K2 to aluminum is surprising, and may be an experimental artifact. The R1, R2, and R3 peptides all exhibit good binding affinities

towards ITO, though the binding of R3 is slightly less than R1 and R2 suggesting some influence of charge clustering. R12 exhibits weaker binding to ITO than R3, indicating that arginine clustering is somewhat detrimental to ITO binding. The clustering of arginine residues has the opposite impact on binding to aluminum as expected with $R1 < R2 < R3$. The increase in binding with increased clustering of arginine residues suggests structural matching with the aluminum surface. The positive charge is distributed among the nitrogen atoms of the arginine side chain, potentially minimizing the charge repulsion between adjacent side chains, explaining the differences in affinity to aluminum between peptides with clustered lysine versus arginine residues. Increasing the total charge and charge clustering, as in peptide R12, does not alter the binding affinity compared to R3. Interestingly, replacing the hydrophilic residue, glycine, with the hydrophobic residue, alanine, as in peptide AR6, enhances binding compared to R1.

The H12 peptide binds well to ITO but poorly to aluminum, indicating that the nitrogen ring structure of histidine can promote adhesion to ITO but is not significantly charged enough to promote adhesion to aluminum. Neither ITO nor aluminum bind the AS6 peptide, indicating that hydrophilic interactions are not enough to mediate binding to either material. DK6 and ER6 show moderate binding to ITO and weak binding to aluminum. The presence of negative charge reduces the overall binding affinity, but this result suggests through proper design a net neutral peptide could have a suitable affinity towards either material.

2.5.4 Dissociation Constant, A08 to Aluminum

The A08 peptide binds strongly to aluminum substrates. Vigorous rubbing of the A08-modified aluminum surface does not remove the peptide. This binding affinity can be quantified by calculating the dissociation constant, k_d . The k_d value is determined from the off rate, k_{off} , determined by measuring the adhesion half-life of the A08 peptide to the aluminum substrate, divided by the on rate, k_{on} . The value for k_{on} is approximated as the diffusion-limited on rate. The adhesion half life for the

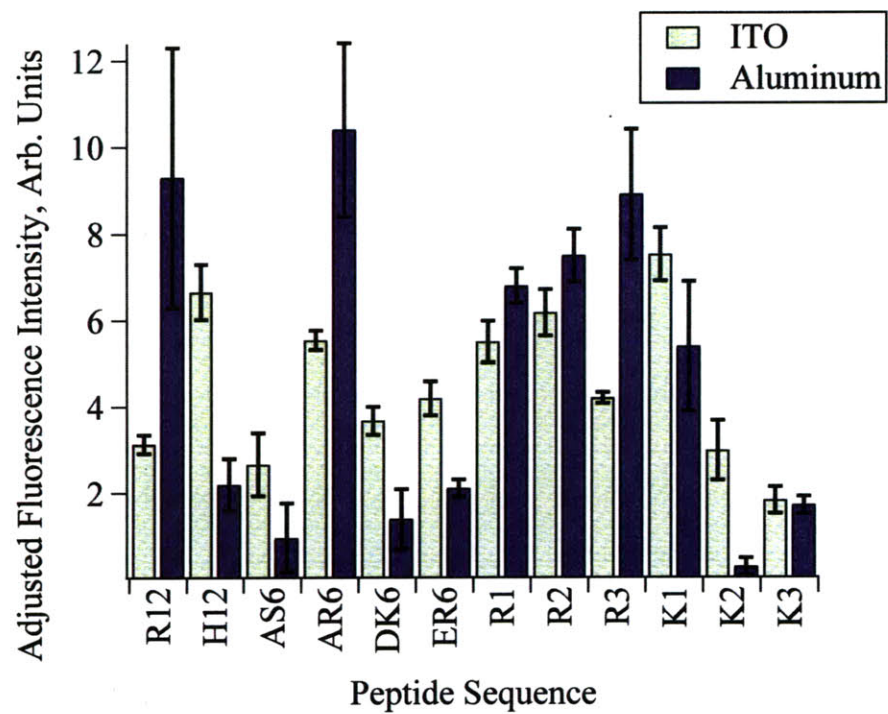


Figure 2-9: The relative adhesion of synthetic peptides to ITO and aluminum substrates.

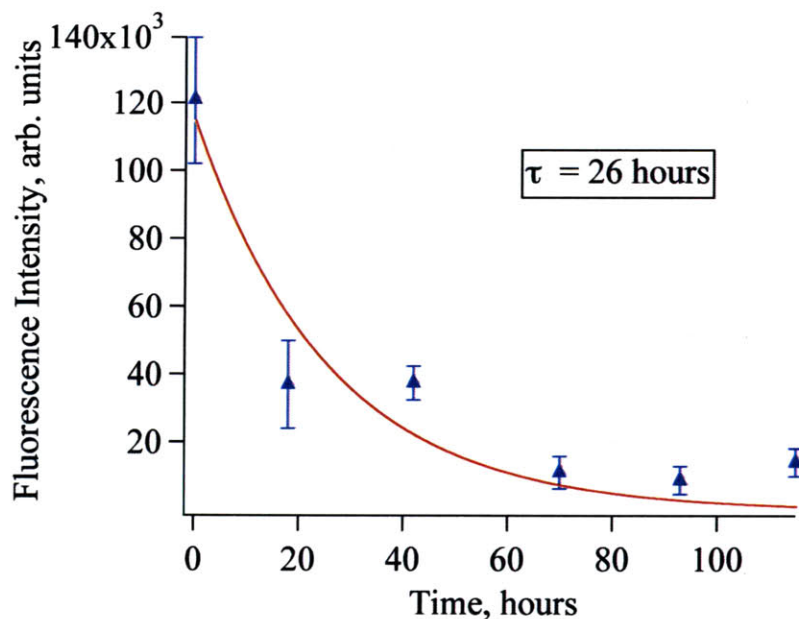


Figure 2-10: Rate of removal of the A08 peptide from an aluminum substrate.

A08 peptide, Figure 2-10, is 26 hours yielding:

$$k_d = \frac{k_{off}}{k_{on}} = \frac{\ln(2)/t_{1/2}}{10^8 M^{-1} \cdot s^{-1}} = \frac{7 \times 10^{-9} M \cdot s}{9.4 \times 10^4 s} \approx 1 \times 10^{-13} M. \quad (2.1)$$

Nanomolar dissociation constants (1×10^{-9}) are considered high affinity interactions for biomolecular binding interactions, typically indicative of a highly specific interaction. Analysis of the “binding rules” established for aluminum along with the breadth of binding exhibited by the A08 peptide refutes any “specific” A08-aluminum interaction. The sub-nanomolar dissociation constant indicates that purely electrostatic interactions between a peptide and surface can exhibit very high binding affinities and suggests that the A08 peptide is suitable as a linker molecule between metal-oxide surfaces and other materials.

2.6 Synthetic Peptides as Binding Mediators

Interfacing biological materials and inorganic substrates has utility for applications including sensors, drug delivery, and biological fuel cells. Biological targets are commonly imaged using quantum dots or microspheres that are coupled to specific peptides. Beyond linking biomaterials to inorganic substrates, peptides have the potential to be used as molecular coupling agents to link any two materials, enabling new levels of control of nanostructured materials. Utilizing carbodiimide chemistry, peptides can be conjugated to any material possessing carboxylic acid groups. The A08 peptide was selected as a model system to demonstrate that short peptide sequences can be used to mediate adhesion between non-biological materials and inorganic surfaces. The strong affinity of the A08 peptide to aluminum was utilized to mediate the assembly of quantum dots and a polymer on aluminum substrates. The A08 peptide was coupled to polymer microspheres as a model system to better understand the role of the yeast surface in mediating binding to substrates such as gold.

2.6.1 Microspheres

The complexity of the yeast surface complicates efforts to understand the role interactions between the surface and displayed peptides play in mediating binding to inorganic materials. For example, the negatively charged yeast surface may play an important role in orienting the A08 peptide in a way that allows its three histidine residues to interact with gold surfaces. Carboxylated polymer microspheres have homogeneous, negatively charged surfaces, making them a suitable platform to probe the role of particle surface charge in relation to A08 yeast gold binding.

The A08 peptide was covalently coupled to 4.5 μm carboxylate polystyrene microspheres (Polysciences). The detailed coupling procedure is in Appendix C.4. The zeta potential of the carboxylate and A08-modified microspheres was measured, Table 2.7. The zeta potential of the unmodified particles is very negative, but when the basic A08 peptide is coupled to the microspheres, the zeta potential is similar to the ≈ 40 zeta value observed for yeast (with or without expressed peptides). The more

A08, μmol	Mobility	Zeta
0.0	-7.9 ± 0.2	-101 ± 2
0.1	-4.9 ± 0.2	-64 ± 3
1.0	-3.4 ± 0.2	-43 ± 2
5.0	-3.8 ± 0.1	-48.7 ± 0.9

Table 2.7: Zeta potential measurements of microspheres.

Sphere Type	Mobility	Zeta
Unmodified	-7.5 ± 0.2	-97 ± 2
Unmod, Esterified	-4.4 ± 0.3	-56 ± 3
A08	-4 ± 0.05	-51.2 ± 0.6
A08, Esterified	-2.11 ± 0.08	-27 ± 1

Table 2.8: Zeta potential measurements of microspheres after esterification.

than 50% decrease in the mobility between the microspheres with no peptide and those reacted with 1.0 μmol of peptide indicates that a significant percentage of the carboxyl groups on the microsphere surface have been functionalized with the A08 peptide.

The A08 microspheres exhibited no binding on aluminum. The net negative charge of the microspheres, even after A08 conjugation, may inhibit their adhesion to aluminum. On gold, the A08 microspheres exhibited enhanced binding over carboxylate microspheres, Figure 2-11. To further probe the interaction between negatively charged groups on the microsphere surface, the A08 peptide, and binding to the aluminum substrate, the microsphere carboxylate residues were esterified through incubation with ethanol. Esterification reduces the negative charge on the surface of both A08-conjugated and un-modified microspheres, as evidenced by the particle zeta potentials, Table 2.8.

Incubation of the A08-microspheres with less than 50% ethanol led to a reduction in binding to gold, Figure 2-11C. The reduction in binding may indicate the disruption of interactions between the peptide and the microsphere surface that enable the peptide to mediate gold binding. Unfortunately, incubation with higher concentrations of ethanol with either the A08 or un-modified microspheres increases binding

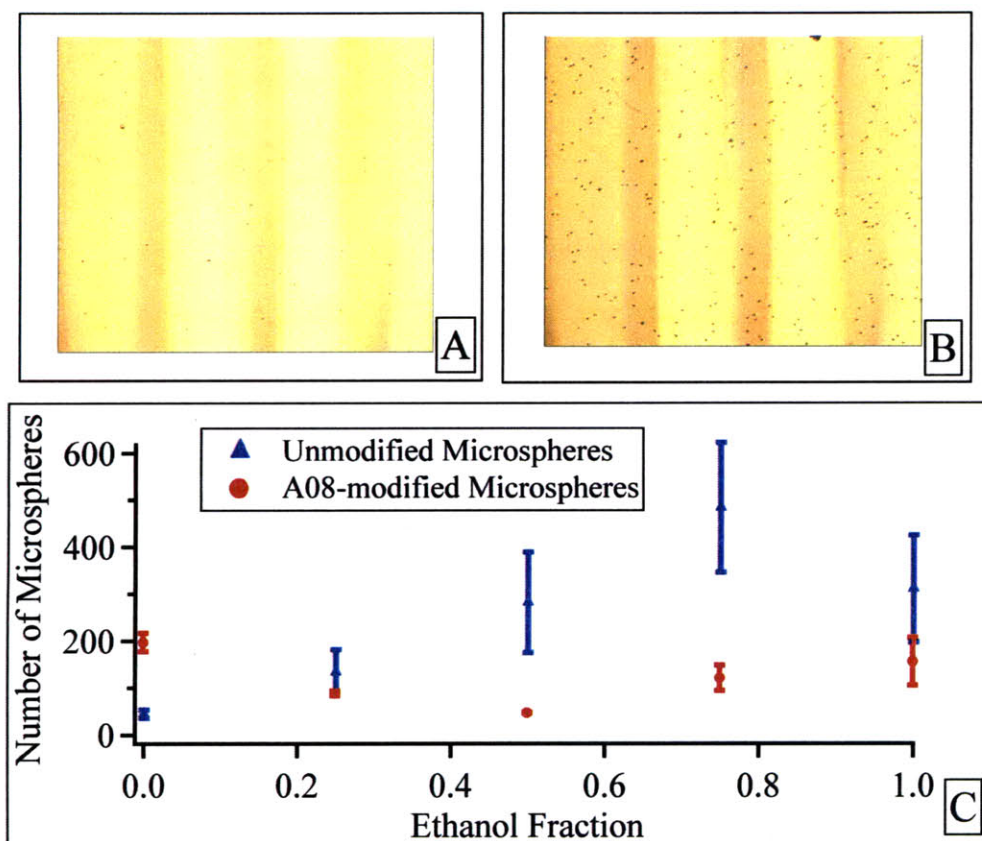


Figure 2-11: Optical microscope images of unmodified (A) and A08 (B) microspheres bound to gold. (C) The relationship between esterification and microsphere adhesion.

to gold, perhaps due to interactions between esters and the gold surface.

2.6.2 Quantum Dots

Quantum dots are fluorescent semiconductor nanoparticles with optical properties that are determined by the quantum confinement of excitons. The emission of quantum dots is tunable based on the size of the particle and unlike organic dyes, quantum dots do not readily photo-bleach. Quantum dot assemblies have potential applications for light-emitting structures, photo-voltaics, and quantum computation and communication. Coupling quantum dots to peptides to mediate assembly on inorganic substrates could enable unique structures to further these different applications.

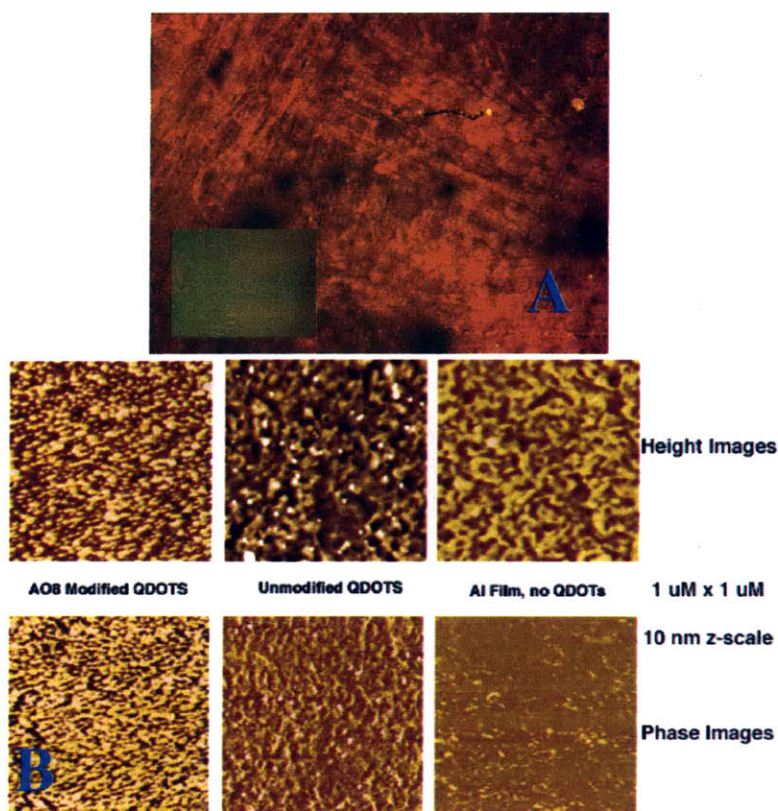


Figure 2-12: (A) Image of fluorescence from A08-Qdots bound to an aluminum substrate. The inset shows fluorescence from aluminum incubated with un-modified Qdots. (B) AFM images taken by Shanying Cui of the A08 and un-modified Qdots on the aluminum surface.

As a proof of concept, the A08 peptide was covalently coupled to 605 nm Amino-QDot quantum dots (Quantum Dot Corporation), Appendix C.1. The A08-quantum dots were incubated with an aluminum substrate (Al on SiO₂), Appendix C.2, and visualized using atomic force (AFM) and fluorescence microscopy. The AFM image, Figure 2-12B, indicates a dense coating of quantum dots on the aluminum surface. Fluorescence from the A08-Qdots was not visible to the eye, but could be imaged using the fluorescence microscope and a 5 sec integration time, Figure 2-12A. The inset of Figure 2-12A is the fluorescence observed from the aluminum surface incubated with un-functionalized Qdots.

2.6.3 A08-Conjugated Polymer

Poly(2-hydroxyethyl methacrylate) (pHEMA) is a biocompatible hydrogel that is used commercially in soft contact lenses [107]. pHEMA and other swellable polymers are highly porous, making them suitable matrices for sensor applications [68, 65]. Immobilization of glucose oxidase within a pHEMA matrix enabled detailed studies of the enzyme's activity in different chemical environments [1]. Applications of hydrogels for on-electrode sensors are hindered by the delamination of the polymer caused by shear forces at the material-polymer interface initiated when the polymer swells.

To improve adhesion properties of hydrogels to inorganic surfaces, a polymer was synthesized with a peptide side-chain to mediate material binding. The A08 peptide was covalently linked to carboxylic acid residues in a poly(2-hydroxyethyl methacrylate/methacrylic acid) 90:10 random co-polymer (pHEMA-co-MAA) using carbodiimide chemistry. The conjugation procedure is described in Appendix C.3. pHEMA-co-MAA and A08-conjugated-pHEMA-co-MAA were deposited on aluminum-coated glass slides to compare their adhesion properties. Adhesion was tested using electrical tape, Figure 2-13. More than 50% of the unmodified polymer was removed from the aluminum surface, while only a small portion of the A08-conjugated polymer was removed. The results of this adhesion test suggest that peptides with a particular material affinity can be used to promote the adhesion of a polymer to that material.

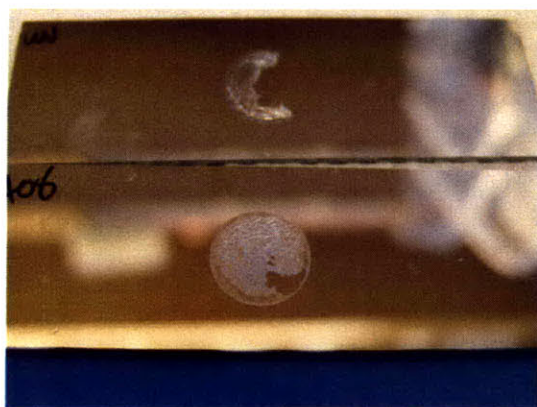


Figure 2-13: Results of adhesion test of pHEMA-co-MAA (top) and A08-modified pHEMA-co-MAA to aluminum-coated slides (bottom).

Chapter 3

Peptide-based electro-responsive materials

3.1 Summary

Phage and yeast display are used in an attempt to identify peptide sequences that exhibit electro-responsive properties. The shortcomings of both phage and yeast display are discussed in the context of the discovery of electro-responsive peptides. The ability of phage to survive exposure to high voltage electric fields is demonstrated. The electrostatic driven interaction between the A08 peptide and an aluminum surface is exploited to demonstrate that pulsed electric fields can remove peptides from an electrode surface and transport the peptides through solution. Charge induced on sapphire surface by high voltage fields is used to remove maltose binding protein from the sapphire surface. Maltose binding protein with a 2K1 affinity tag is removed from an ITO surface using a low voltage electric potential. In conclusion, peptides that interact with a material surface through electrostatic dominated mechanisms can potentially replace complex self-assembled monolayer structures as electro-responsive tags of inorganic materials.

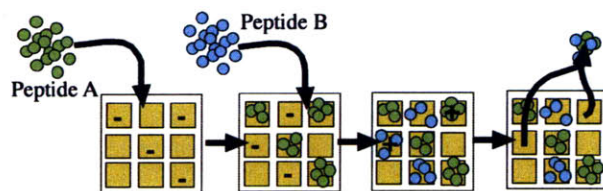


Figure 3-1: Addressable deposition and release of peptides from an electrode array could improve controlled drug delivery. Material-specific, electro-responsive peptides would make this type of application a reality.

3.2 Motivation

Electrical control of biological molecules has the potential to impact technologies including biological and chemical sensing, environmental monitoring, protective films, and drug delivery. The original vision for this work was to employ combinatorial tools such as phage and yeast display under electrical selection pressure to identify peptide sequences that respond to a particular electric field or potential by releasing from a material surface. Alternatively, through the application of a different design pressure, peptides that only bind to a particular material when an electric field is applied could be isolated. With peptides that are both material specific and field controllable it would be possible to control spatially peptide deposition and desorption using an electric stimulus.

Electro-responsive peptides could be used to link drugs to an array of electrodes enabling controlled delivery of the drug through the electro-release of the peptide-drug complex, Figure 3-1. For many sensor applications, the underlying electronics are intricate and expensive. Electro-responsive linkers could yield the ability to rapidly reconfigure a sensor system for a new target or to regenerate a saturated sensor by simply releasing old sensing molecules from the surface and incubating with fresh active species. Currently, many paint and coating technologies for metal surfaces require toxic, flammable solvents to remove the coating. An electro-releasing peptide could mediate the adhesion of coatings which, under regular conditions, adhere well to a surface but can be removed rapidly using an electric field.

3.2.1 Electric Fields in Natural Systems

Electrical signaling in neural circuitry, cell membrane potentials, and photosynthetic redox processes are all examples of situations where electrochemical stimuli play crucial roles in natural systems. While redox chemistries take place with potentials on the order of one volt, the voltage-gated ion channels found in electric eel electrocyte membranes cooperate to produce potentials as high as 600 V. Within cells there can be small voltage differences, ≈ 100 mV, over very small distances, such as a mitochondrial membrane, that yield extremely large electric fields, on the order of $10^6 \frac{\text{V}}{\text{m}}$ or larger.

One example from nature, photosystem II, has particular relevance to this work. Photosystem II is a protein complex that is the water oxidation hub of photosynthesis. Photosystem II (PSII) is described in more detail in Section 1.3. One of the critical functionalities of PSII involves peptide electro-release of the electron accepting molecule, plastoquinone (Q_b). The PSII protein removes electrons from water and transfers them to Q_b . The D1 protein, part of PSII, selectively binds Q_b in a pocket involving approximately 50 amino acids [29, 99]. After two electrons are transferred to Q_b , the binding pocket no longer recognizes the molecule and it is liberated from the D1 protein, moving into the hydrophobic core of the photosynthetic membrane [106]. Q_b is a biological example of a material that undergoes an electro-chemical change and as a result is released by a peptide that no longer possesses an affinity for that material.

3.2.2 Electroactive Monolayers

Synthetic electro-responsive films, relying on redox chemistry similar to that of PSII, have been developed by Mrksich et al. [43, 44, 51]. In their work, redox active groups are coupled to self-assembled monolayers (SAMs) on gold. Mrksich et al. designed SAMs that can release biomolecules under electrochemical control. These SAMs consist of alkanethiolates that attach to gold through their thiol group and assemble in an ordered way due to hydrophobic interactions between the long alkane chains.

Attached to the alkanethiolate is a triethylene glycol group that prevents non-specific adsorption of protein to the surface. Some chains in the SAM are terminated by the electroactive molecule quinone propionic ester, a difunctional molecule that can be linked to both the SAM and a biomolecule. When a reductive potential is applied (-700 mV) to the underlying gold substrate, the quinone is reduced to hydroquinone and rapidly undergoes lactonization thereby releasing the biomolecule [44]. These electro-active monolayers have been used to pattern and selectively release cells on electrode surfaces [20, 51, 110, 111].

As a platform for electro-responsive films, thiolated alkane monolayers on gold have several drawbacks. The thiol-gold interaction that drives monolayer assembly limits these films to gold or other surfaces that can be thiolated. Because the quinone chemistry is induced electrochemically, interference may occur from other reactions that take place in the same potential regime. Lastly, the system is sensitive to the potential applied, with voltages below -800 mV damaging the monolayer [110]. Wang et al. avoid some of the complexities of working with SAMs through the direct electrochemical desorption of thiolated DNA from gold, however this approach demands even higher potentials, -1.3 V, and still employs a thiol ligand to mediate adhesion to gold [104].

The non-specific adhesion of bacteria to certain electrode materials such as ITO arises from an interplay between Lifshitz-van der Waals and electrostatic interactions, described theoretically using Derjaguin-Landau-Verwey-Overbeek (DLVO) theory. The adhesion is a secondary minimum phenomenon, with bacterial desorption probability measurements yielding an average interaction energy of $\approx -3 \text{ KT}$ [102]. Poortinga et al., demonstrated that the non-specific adhesion of bacteria to an electrode could be overcome by applying a negative potential to the electrode, observing that the probability of desorption increased with increasing current density [88]. As a corollary result, Poortinga et al. observe that applying a positive potential to the electrode surface during cell adhesion drives the cell adhesion to a primary energy minimum and consequently the cells cannot be stimulated to desorb [88].

Employing Lifshitz-van der Waals adhesion to materials such as ITO as the basis

for building electroresponsive films again has drawbacks. This type of adhesion is relatively weak, meaning that cells constantly detach and reattach to the substrate even with no applied field. Furthermore, many materials that do not support Lifshitz-van der Waals interactions are eliminated from consideration as substrates for electroresponsive films.

3.2.3 Peptide Based Electro-responsive Materials

In this work, peptides are examined as electro-responsive materials. Initially, traditional phage and yeast display screening techniques were employed to identify peptides that exhibit a particular material affinity and are field responsive, however these techniques were unsuccessful in yielding such a sequence. The broad spectrum binding peptides, A08 and 2K1, which were shown to bind primarily due to electrostatic interactions, were used as the basis for further studies of electroresponsive behavior. Using high voltage (kV), short (ms) pulses, the A08 peptide was removed from an aluminum electrode, transferred through solution and reattached to the opposing electrode. Additionally, A08 yeast was removed from a sapphire surface placed in a high voltage electric field. At low voltage, the removal of the 2K1 MBP was shown from an ITO electrode.

3.3 Theory

Under the influence of an external potential, a charged particle suspended in an aqueous medium is influenced primarily by three forces: the electric force, \mathbf{F}_1 , is induced by the interaction between the applied field, \mathbf{E} , and the charge on the particle, q ; the hydrodynamic friction force, \mathbf{F}_2 , is produced by the viscous interaction between the particle and the surrounding medium (ν is the viscosity of the medium, a is the particle radius, and \mathbf{U} is the electrophoretic velocity); and the electrophoretic force, \mathbf{F}_3 , which is caused by the opposing, field induced motion of the oppositely charged ions in solution (ϵ is the dielectric constant of the medium and ζ is the potential of

the particle at its surface of shear).

$$F_1 = qE \quad (3.1)$$

$$F_2 = -6\pi\nu \quad (3.2)$$

$$F_3 = E(\epsilon\zeta s - q) \quad (3.3)$$

Combining these three equations yields the electrophoretic mobility of the particle, μ , and the particle velocity, v_d . The mobility of the particle is proportional only to the electrokinetic ζ -potential; all of the other parameters are features of the surrounding medium.

$$\mu = \frac{\zeta\epsilon}{6\pi\nu} \quad (3.4)$$

$$v = \mu E = \mu \frac{\zeta\epsilon}{6\pi\nu} \quad (3.5)$$

The behavior of a “free” peptide in an electric field is better described by a purely diffusional model rather than the Stokes drag model described above. The steady state migrational velocity is given by the Einstein-Smoluchowski equation (D is the diffusion constant, k_b is the Boltzmann constant and T is the absolute temperature). For a short peptide, the diffusion constant can be estimated using the Polson equation, which states that the diffusivity is proportional only to a constant, C , and the molecular weight, M [87]. For peptides with molecular weights greater than 1000, $C = 2.74 \times 10^{-5}$ [87].

$$v_d = \frac{qED}{k_b T} D = \frac{C}{M^{1/3}} \quad (3.6)$$

In a pulsed electric field, particles or peptides may not reach terminal velocity before the pulse ends. In such a case, the object will continually experience a net overall force due to acceleration and deceleration.

3.3.1 Overcoming Electrolysis of Water

When a continuous potential greater than ≈ 1.2 V is applied to water, electrolysis occurs at the electrodes and water is split into hydrogen and oxygen. While this phenomenon is important to the work in Chapter 4, electrolysis and other electrode reactions are problematic for constructing electro-responsive films. The violent formation of gas bubbles at the electrode surface can physically disrupt coatings or chemically damage the coating through oxidation or reduction reactions. Substantial electrochemical reactions at the electrode surface only begin to occur once the electrical double layer is formed. The electrical double layer consists of a layer of surface charge at the electrode and a second diffuse layer of charge formed by free ions in solution. All surfaces in solution have some form of double layer charge, but when the potential is changed at an electrode surface the double layer is altered, taking as long as several seconds to return to a steady state value. The application of potential as short pulses can inhibit the complete charging of the double layer, thereby minimizing the electrolytic breakdown of water. Using short electrical pulses, voltages significantly higher than 1.23 V can be applied without disruptive, damaging gas evolution occurring at the electrodes.

3.3.2 High voltage phenomena

Under the influence of large electric fields, water exhibits many phenomena that do not occur under typical conditions, potentially influencing peptide and particle motion and adhesion. When very large voltages are applied, water can undergo dielectric breakdown (glow discharge). Dielectric breakdown is a surface driven phenomenon, related to the current density-voltage ratio [101]. Dielectric breakdown and pre-breakdown phenomena dramatically change the flow characteristics and can also yield significant temperature changes in the solution [52]. Under the influence of somewhat lower electric fields (kV/cm) exhibits space charge injection phenomena [115]. Other strongly nonlinear phenomena can also occur, substantially modifying the mathematics of transport in aqueous solution at high voltages [7, 25].

3.4 Experimental Setup For Electrical Experiments

For constant voltage studies of phage survivability and phage biopanning with electric field elution, a constant voltage power supply was used. Experiments studying phage survivability in a pulsed electric field (D. S. Yun [114]) and the electrically driven removal and transit of the A08 peptide were performed using a Bio-Rad Micropulser electroporator. Electroporators are a tool used by biologists to introduce DNA into cells through pores that open on the cell surface due to large electric fields. An electroporator is a pulsed power supply that provides an exponentially decaying pulse at a specified voltage ranging from 100 to 5000 V and currents as high as 100 A. Within the instrument is a large capacitor that is discharged across two electrodes. The decay constant cannot be controlled, but is a function of the voltage, the internal capacitance, and the dielectric properties of the sample. Standard electroporation cuvettes (VWR) were used as electrodes. These electroporation cuvettes are polycarbonate with two rough aluminum electrodes spaced 2 mm apart. This experimental setup is shown in Figure 3-2.

Yeast selection experiments with electrical elution and yeast release from a bipolar electrode were performed on a setup that was designed to apply series of square wave, high voltage pulses. A low voltage pulse sequence was produced using an arbitrary function generator (Tektronix, AFG310), computer controlled through GPIB using Igor Pro (Wavemetrics). The low voltage signal was amplified by a factor of 1000 by a high voltage amplifier (Trek 5/80-L). The high-voltage amplifier outputs a low-voltage signal corresponding to the current in the system. The current was monitored using a Digital Storage Oscilloscope (Tektronix TDS 2002). The setup for producing arbitrary, high voltage wave forms is shown in Figure 3-3.

For 2K1-MBP electro-desorption experiments, a three electrode setup was used. The voltage was controlled by a bipotentiostat with an ITO working electrode, platinum wire counter electrode (Alfa Aesar), and an Ag/AgCl reference electrode (BASi).

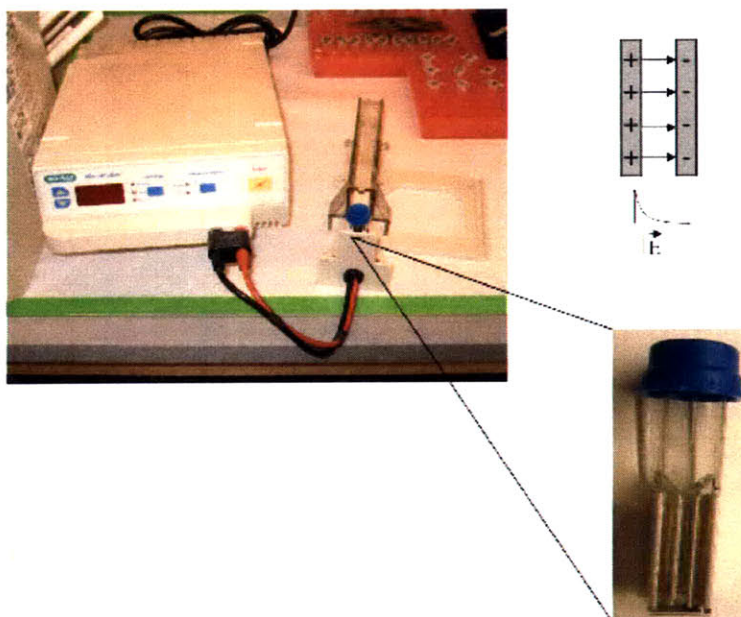


Figure 3-2: A Bio-Rad Micropulser electroporator was used for pulsed field experiments. This power supply produces an kV amplitude exponentially decaying voltage signal.

3.5 Bio-panning with Electrochemical Elution Pressure

As described in Section 2.3, peptide libraries displayed on either phage or yeast can serve as powerful tools to discover peptides that exhibit strong affinities for a particular material. In phage and yeast screening, clones that adhere to a particular substrate are eluted from the material surface either by acid elution or directly growing/amplifying the clone off of the surface. Acid elution, particularly, will bias the screen towards amino acids that change protonation state due to the acidic environment. In this section, an electric field or electric potential is used to elute bound phage or yeast from a material surface in an attempt to bias the selection process towards peptides that exhibit electro-responsive behavior. Figure 3-4 shows the selection procedure.

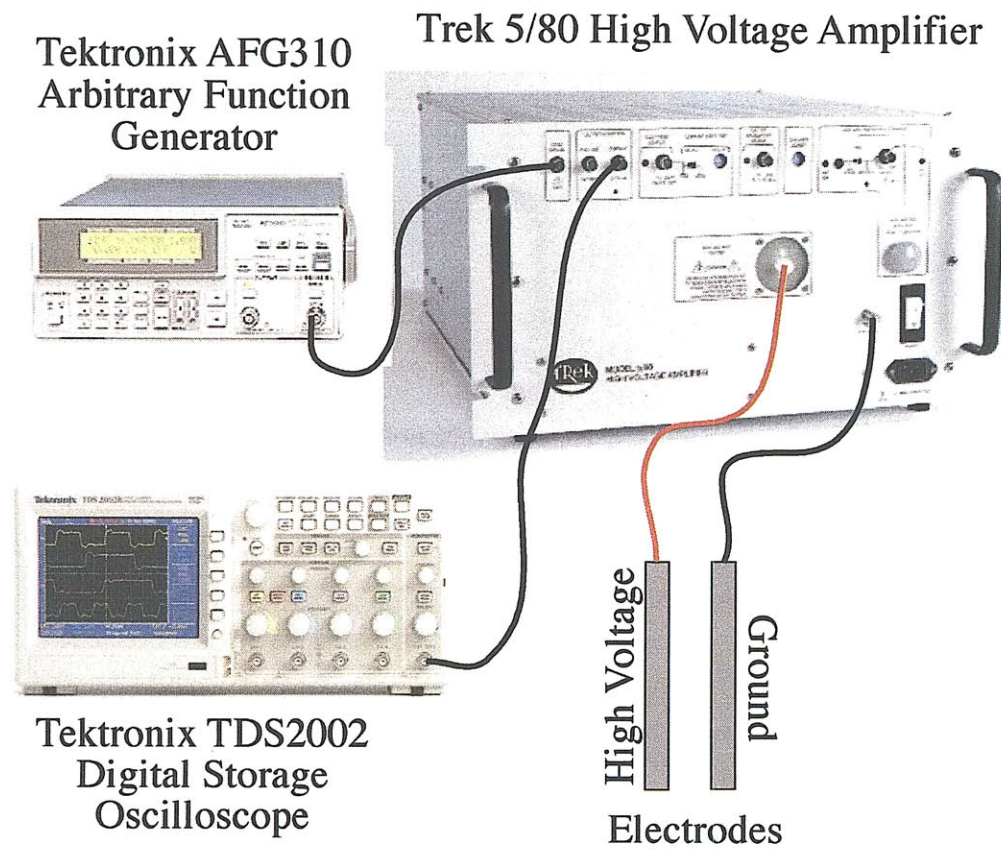


Figure 3-3: A system for producing arbitrary, high voltage pulses. The Trek high voltage amplifier increases the voltage waveform produced by the Tektronix function generator by a factor of 1000.

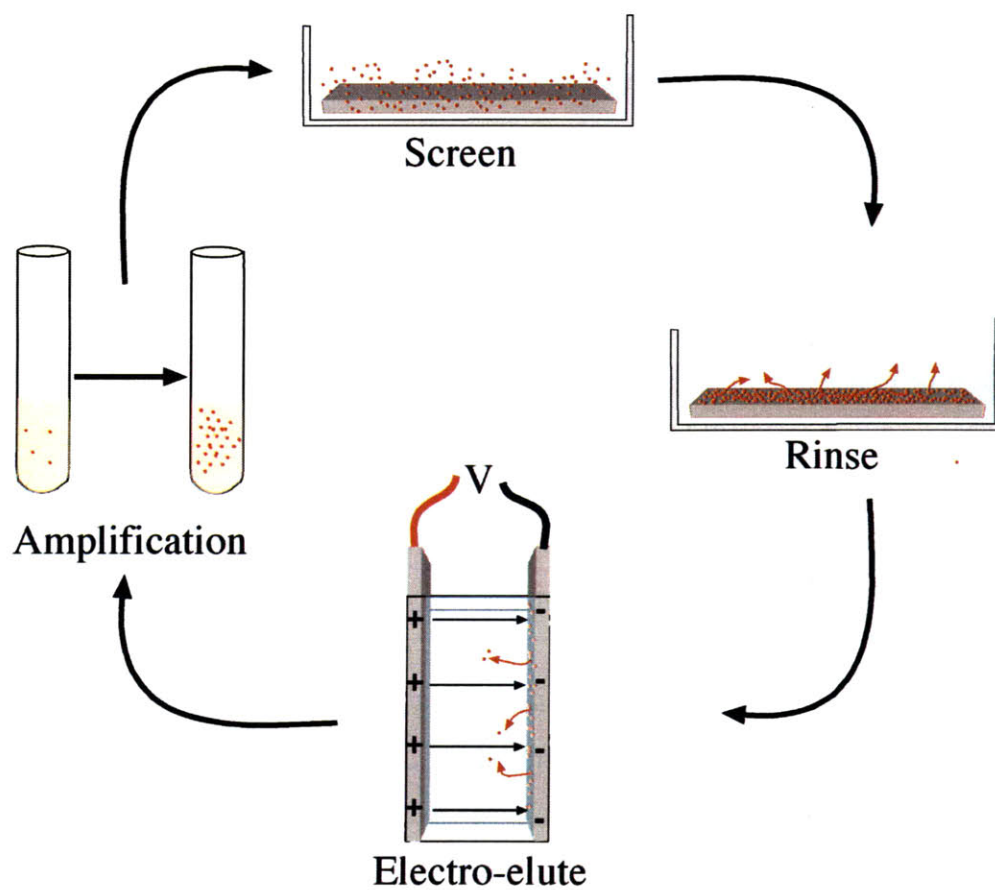


Figure 3-4: Phage/Yeast display screening procedure employed to identify peptide sequences that exhibit electro-responsive behavior on a particular material surface.

Electric Field	Time of Exposure	Phage In, PFU/ μ L	Phage Out, PFU/ μ L
50 V/cm	1 hour	74	24
50 V/cm	5 hours	4.9	25
5 kV/cm	10 minutes	2.9	3
9 kV/cm	10 minutes	3	2.6
15 kV/cm	10 minutes	4.2	4

Table 3.1: Phage survivability in an electric field with no current flow.

3.5.1 Phage Survivability

The biological framework used for peptide discovery must be able to withstand the electric fields or potential employed for elution of bound clones. A cylindrical capacitor setup, designed to inhibit current flow between electrodes, was employed to assay the survivability of bacteriophage in an electric field. A constant electric field was applied between the two electrodes.

The results, shown in Table 3.1, indicate that phage can survive continuous electric fields up to 15000 V/cm. Examining phage survivability under the influence of high voltage with current flow, a collaborator, Dr. Dong Soo Yun, observed that applying ten 1 ms, 1 kV exponentially decaying pulses to a phage solution decreased the phage titer by a factor of 100 [114].

Yeast proved even more resilient to electric currents than phage. Yeast bound to an aluminum surface were exposed to twenty 5 kV pulses and grown off the substrate. The optical density of yeast grown up from the aluminum surface after electrical exposure was actually higher than that of yeast not exposed to a field.

3.5.2 Phage and Yeast Screening with Electrical Elution

Several attempts were made using phage display to identify electro-responsive peptide sequences. Electro-elution using only electric fields and using electrode potentials with current flowing were both attempted. Voltage conditions varying from 1 V to 30 kV with a shielded electrode were tested to elute phage and platinum. Unfortunately, no enhanced electrical response was observed after several rounds of screening. It is likely that the electro-eluted phage were simply weak binders that would have been

removed after another wash step.

A similar problem was faced using yeast. To try and isolate a yeast clone with electro-responsive adhesion to aluminum, series of one hundred ± 5 kV, 10 ms pulses with 500 ms spacing were applied to the electrodes. The water solution and the ground electrode was placed in SD media to grow off cells removed from the biased electrode. After four screening rounds, the yeast exhibit no enhanced removal from the working electrode under an applied potential. During some individual screening rounds, a measurable removal of yeast is observed; however, this behavior is not sustainable through subsequent screening rounds. This transient appearance of electro-responsive behavior may be related, not to the sequence of the displayed peptide, but rather to the number of expressed peptides on the yeast surface, which may be variant among screening rounds. For electric field controlled yeast display screening to be successful the yeast display technique needs to be improved by increasing homogeneity in the number of displayed peptides per yeast.

The intrinsic negative surface charge of phage and yeast may be the most serious shortfall of these display techniques for discovering electro-responsive peptides. Examining the binding rules for common electrode materials such as gold, aluminum, and ITO, indicates that basic amino acids play an important role in mediating binding. A positive bias applied to the electrode would then be needed to release these peptides. Unfortunately, applying a positive bias will also attract the negatively charged bacteriophage or yeast cell to the electrode, countering the “releasing” effect of applying an electric potential. To overcome the negative charge of the PVII, the bacteriophage could be modified to express a positively charged sequence on the major coat protein, however positively charged peptide inserts inhibit phage assembly. The net negative charge of yeast cells could be overcome by increasing the overall number of displayed peptides on the yeast surface, yielding a yeast cell with an overall neutral or positive surface.

3.6 Electrically Controlling A08 Peptide Binding to Aluminum

The positively charged A08 peptide interacts with aluminum primarily due to charge interactions with the negative surface, making the peptide a good candidate to exhibit some type of electro-responsive behavior. A low voltage (>1 V), positively charged bias was applied to an aluminum electrode that had been labeled with the Alexa Fluor 488-modified A08 peptide. No peptide removal from the aluminum electrodes was observed (data not shown). Increasing the applied potential led to gas bubble formation and damage to the aluminum surface, which masked any electro-responsive behavior of the peptide.

The electroporator setup described in Section 3.4 was used to apply short, kilovolt pulses to A08 peptide bound to aluminum, with minimal damage observed to the underlying substrate. An aluminum electroporation cuvette (2 mm gap) was filled with a 500 μ M solution of A08 peptide in Millipore water and incubated for 1 hour. The cuvette was rinsed $3 \times$ and then refilled with Millipore water. A series of voltage pulses were applied to the electroporation cuvette and then the cuvette was split open and the electrodes imaged using the fluorescent microscope.

The application of twenty 2.5 kV pulses to the A08-modified electroporation cuvette resulted in removal of peptide from the positively biased electrode and an increase in peptide adhered to the negative electrodes, indicating that not only do the electrical pulses remove the peptide from the aluminum electrode, but the pulses are also able to transport the peptide through solution. Furthermore, the re-adhesion of the peptide to the negative electrode indicates that the functionality of the peptide was not destroyed by the electric pulses. Unlike bacteria deposited on ITO under the influence of a potential [88], the A08 peptide when transported to the negatively biased electrode did not bind irreversibly. Reversing the bias and applying an additional 30 pulses resulted in transport of the A08 peptide back to the electrode that was originally positive. Figure 3-5 shows fluorescence micrographs and a cartoon detailing the transfer of peptides between electrodes under a particular applied field.

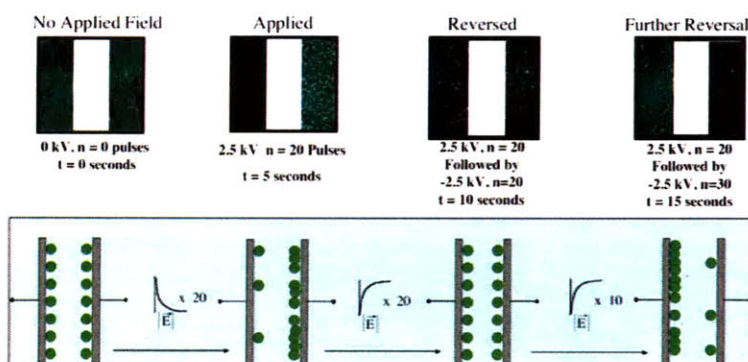


Figure 3-5: Fluorescence micrographs showing the pulsed electric field driven removal of the A08 from a positively biased electrode and the transfer of the peptide to the negatively biased electrode.

Figure 3-6 shows the results of reversing the potential after transporting a substantial fraction of peptide between electrodes. Applying an additional twenty reverse biased pulses re-equilibrates the peptide concentration between the two electrodes and applying an additional 10 pulses causes enhanced peptide binding on the electrode that was originally positive.

To determine the threshold voltage for peptide removal, A08-modified electroporation cuvettes were pulsed twenty times with 0 kV, 0.5 kV, 1.0 kV and 2.5 kV potentials, Figure 3-7. Little peptide removal was observed below 1.0 kV. Even though the fluorescence from the 0.5 kV samples was less than that of the 0 kV samples, this does not suggest that peptide was removed from the positive electrode, as the fluorescence intensity was the same for both the positively and negatively biased electrodes at 0.5 kV. Because of sample to sample differences, the difference between fluorescence intensities on the negative and positive electrodes is more important than the overall fluorescence amplitude. More peptide was transferred to the negative electrode at 2.5 kV than 1.0 kV, suggesting that the 1.0 kV is not able to transport the peptide through solution during the time of exposure.

The number of times A08-modified electroporation cuvettes were pulsed was varied to better understand the transport phenomena behind the movement of the A08 peptide between the positive and negatively biased electrodes, Figure 3-8. Beyond

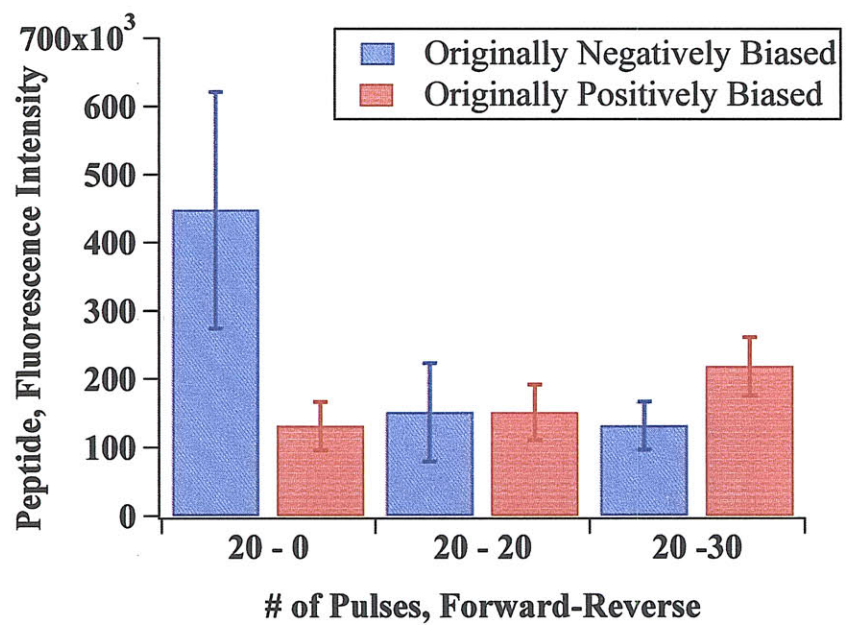


Figure 3-6: The effect of reversing the potential after peptide has been released from the positive electrode and transferred to the negative electrode. The ability to reversibly transfer the peptide between electrodes differentiates this system from the bacterial adhesion system described by Poortinga et al. [88].

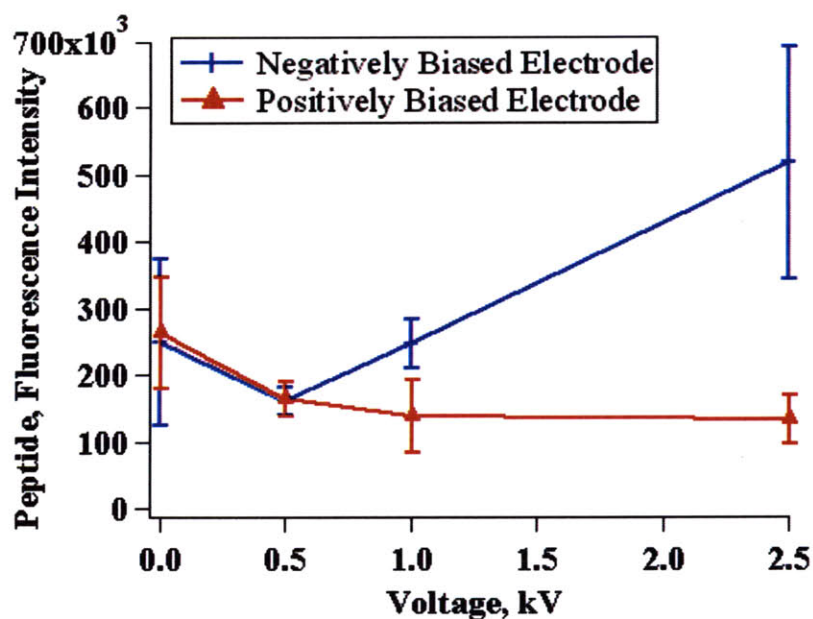


Figure 3-7: The influence of potential magnitude on the pulsed-field removal and transport of the A08 peptides in electroporation cuvettes.

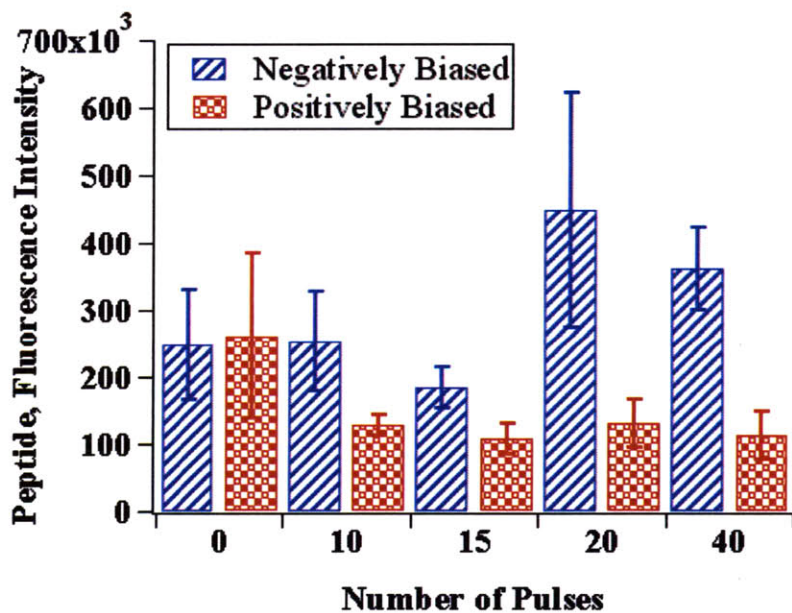


Figure 3-8: The number of 2.5 kV pulses required to transport the A08 peptide between electrodes.

10 pulses, no additional peptide appears to be removed from the positively charged electrode. Increased peptide adhesion to the negative electrode only appears after 20 pulses and applying additional pulses does not appear to further increase the amount of peptide on the negative electrode. Precise examination of the transport of the A08 peptide between electrodes is not possible using the electroporator as a power supply because variations in the conductivity of the water can lead to different pulse lengths. Furthermore, the field pulses are applied by manually pressing a button, meaning the time between pulses is not precisely controlled.

Using the high voltage amplifier system, a more precise characterization of the number of pulses required to transport the peptide between electrodes was conducted. The results of these experiments are shown in Figure 3-9. A 6.25 kV/mm field with 5 ms square wave pulses separated by 0.5 seconds was used for these experiments. From the number of pulses and the pulse duration, the time of transport can be computed. The time of transport can be compared to a theoretically derived number based on the drift velocity. The theoretical drift velocity, given by Equation 3.6, is dependent on the diffusion constant of the A08 peptide. The diffusion constant, calculated using Equation 3.6, is $2.32 \times 10^{-10} \frac{m^2}{s}$, yielding a drift velocity of 43 mm/s. To travel between electrodes the peptide would take ≈ 100 ms, or about 20 pulses. Considering the rough nature of this estimate, the possibility of diffusion between pulses, and other non-linear effects resulting from the high voltage, this result is in relatively close agreement to the 50 to 100 pulses it takes to completely transport the peptide experimentally.

3.7 Bipolar Electrode - Electrically Removing Yeast From Sapphire

When a semi-conducting or insulating material is placed in an electric field, a surface charge is induced in response to the applied field. This phenomenon was used to remove yeast from the surface of sapphire. Figure 3-10 shows a simulation (ANSYS) of

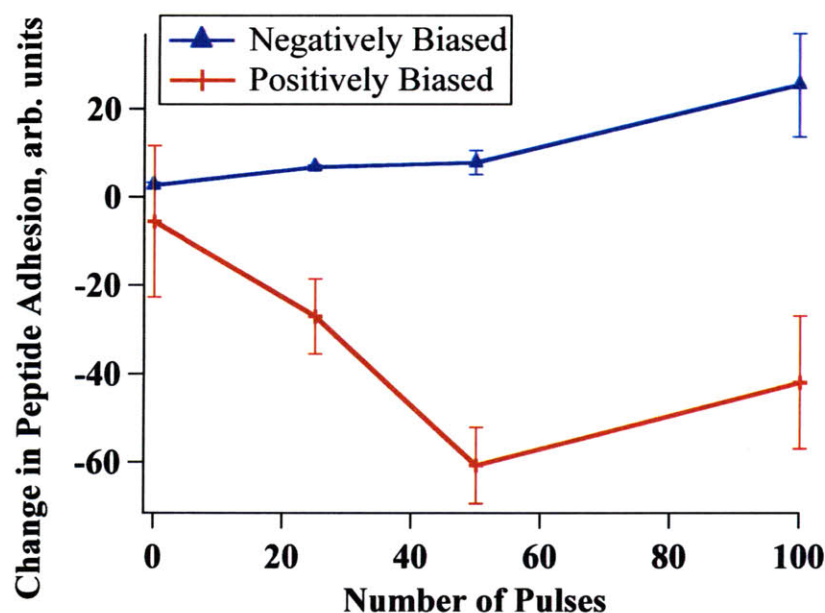


Figure 3-9: The number of 2.5 kV pulses required to transport the A08 peptide between electrodes.

the potential induced on the surface of a piece of sapphire suspended in water between two electrodes. The surface of sapphire is highly negatively charged, so electrostatics are expected to play an important role in the binding to sapphire. Krauland et al. demonstrated that electrostatics is the primary driving force controlling adhesion to sapphire [61]. Altering the charge of the sapphire surface is therefore expected to counteract the yeast affinity for the surface. Sapphire-binding yeast, expressing the peptide KRHKQKTSRMGK, was bound to the surface of sapphire. The high voltage pulse system was used to induce a charge on the sapphire surface to overcome the inherent negative surface charge. Figure 3-11 shows the amount of yeast removed from the sapphire surface by applying -5 kV pulses of different lengths. The number of pulses was selected so that the total time of exposure to the electric field was 1 second. Increasing the pulse length did not increase the fraction of yeast removed from the sapphire surface. No more than 20% of the yeast was removed using this bipolar electrode setup, suggesting that only yeast that were initially weakly bound to the sapphire surface could be detached by the induced charge.

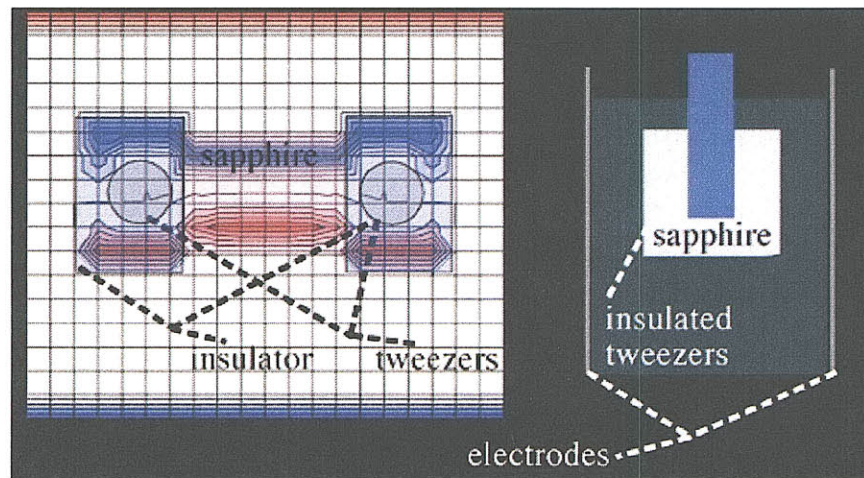


Figure 3-10: A simulation of field induced charge on a sapphire substrate.

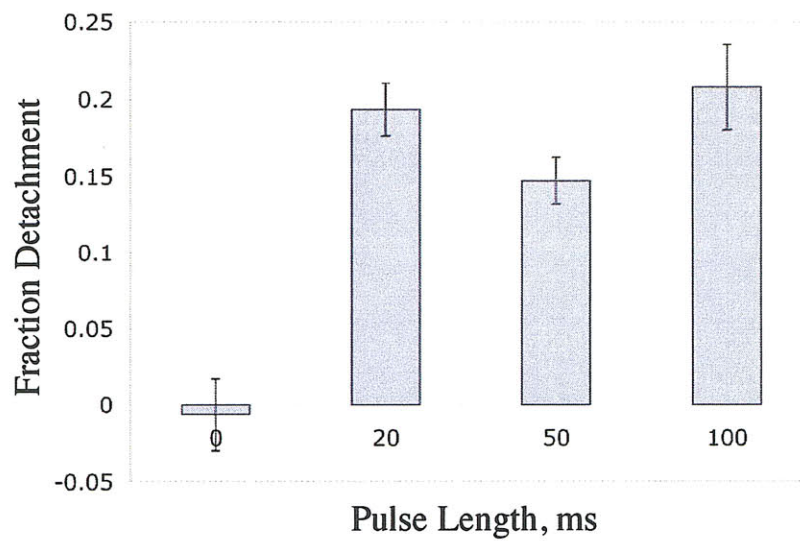


Figure 3-11: Yeast removal from a sapphire bipolar electrode by applying -5 kV electric field pulses.

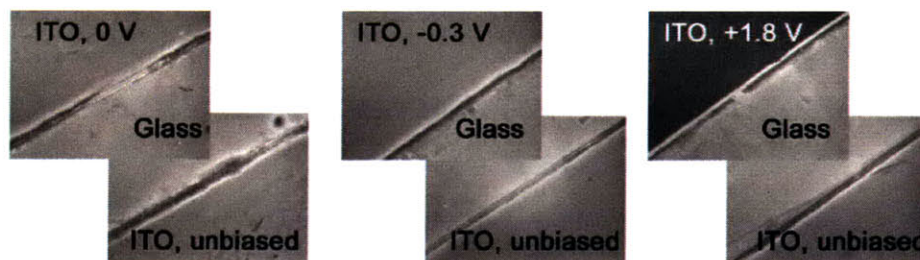


Figure 3-12: Result of applying different electric potentials to MBP-2K1 bound to ITO.

3.8 Removal of 2K1-MBP from ITO

The work in this section was a collaboration with Eric Krauland. Poortinga et al. observed that bacteria adsorbed on ITO could be removed by applying an electric potential to the electrode surface [88]. The 2K1 peptide and bacteria both adhere to ITO through Lifshitz-van der Waals and electrostatic interactions, so it seems probable that 2K1 could be removed from the ITO surface electrically in the same manner as bacteria. To test this hypothesis, affinity tagged protein MBP-2K1 was bound to a patterned ITO surface. The detailed procedure for patterning and cleaning of ITO is described in Appendix C.6. A well was formed on the surface of the ITO-coated slide using silicone gaskets, and 180 μL of PBS-T and with 20 μL of 10 $\mu\text{g}/\text{mL}$ MBP-2K1 was added to the well. The ITO surface was patterned with two strips, to one a potential was applied and the other served as a control. The active ITO strip was biased either with -0.3 V or +1.8 V. Application of 0 V or -0.3 V for 5 minutes did not alter the binding of the MBP-2K1 protein to the ITO, but +1.8 V for as little as 30 seconds significantly inhibited binding to the biased ITO substrate. Figure 3-12 shows the adhesion of immuno-labeled MBP-2K1 to ITO under different bias conditions.

3.9 Future Directions

Future experimental work should be focused on three goals. First, by examining the electroresponse of carefully designed peptide sequences, a better understanding of the role individual amino acids play in driving electroresponsive peptide behavior can be developed. Using this information, peptide sequences that respond to a particular electrical stimulus could be developed. The second research focus should be to understand the mechanisms of release and transport of the peptides under the influence of high voltage fields. The transport kinetics in water at these time scales and voltage magnitudes is poorly understood. A firm grasp on the kinetics would enable the engineering of precise microfluidic devices that can controllably deliver peptides or other particles. The final research focus should be to explore the electroresponsive behavior of quantum dots, polymers or other systems where the electroresponsive peptide acts as a linker to the material surface. Electroresponsive quantum dots could be used as highly controllable fluorescent markers, and polymers could serve as an electroresponsive coatings.

Chapter 4

Photocatalytic Water Oxidation

4.1 Summary

The oxidative splitting of water photosensitized by metalloporphyrins and with an iridium oxide catalyst (IrOx) is studied. Nanoscale arrays of porphyrin molecules are covalently attached to the surface of M13 bacteriophage. An IrOx-binding peptide expressed on the bacteriophage is used to co-assemble IrOx with the porphyrin to form photocatalytic hybrid nanowires. Oxygen production data indicate that the hybrid nanowire structure yields a dramatic improvement in catalytic performance, nearly a 7 fold increase in catalytic turnover.

The interaction between the IrOx-binding peptide and colloidal particles is characterized using 2D-NMR, FTIR and HPLC. Synthetic peptides are used to couple IrOx colloids and Zn(II) porphyrin, separating the two using several different spacer amino acid sequences. The oxygen evolution of these peptide/IrOx/porphyrin triples is measured to probe differences in energy transfer induced by different peptide sequences.

In search of a non-sacrificial electron acceptor to replace sodium persulfate, a cerium(IV) dipicolinate (Ce(IV) dipic) molecule is synthesized and characterized. Photocatalytic oxygen production using the Ce(IV)dipic complex as an electron acceptor indicates that this molecule performs at least as well as persulfate as an oxidant. An electrochemical flow cell is used to regenerate Ce(IV) dipic from Ce(III) dipic.

4.2 Porphyrin-Sensitized, Iridium-Oxide-Catalyzed Water Oxidation

In photosynthesis, organometallic chromophores (chlorophyll molecules) absorb light and transfer the energy to the Mn-oxo catalytic center. Synthetic systems, inspired by PSII, show photocatalytic oxygen production from porphyrin molecules and catalytic iridium oxide clusters [79]. The iridium oxide and porphyrin system was selected as a model photocatalytic system because iridium oxide is one of the highest efficiency catalytic metal oxide materials for the photo-oxidation of water [41] and porphyrins are relatively inexpensive, wavelength tunable, and easily functionalized.

4.2.1 Review of porphyrin/metal oxide photooxidation of water.

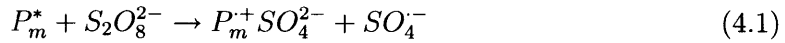
The early work of Harriman et al. suggested that while metalloporphyrin π -radical cations have high redox potentials, “these compounds appear to possess little promise as water oxidants in homogeneous photosystems” [42]. A year later, Harriman and coworkers showed that Zn(II) porphyrins with $\text{RuO}_2 \cdot \text{H}_2\text{O}$ were able to oxidize water to molecular oxygen [24]. In this second work, a colloidal RuO_2 catalyst was employed rather than a solid $\text{RuO}_2/\text{TiO}_2$ substrate, underscoring the importance of surface chemistry in catalytic processes. Harriman et al. screened sixteen different transition metal oxide materials as candidates to catalyze water oxidation sensitized by $[\text{Ru}(\text{bpy})_3]^{2+}$. Iridium oxide exhibited the highest rate of oxygen evolution ($2.7 \times 10^7 \text{ mol dm}^{-3} \text{ min}^{-1}$) and quantum yield (61%) of all the metal oxides tested [41]. While iridium oxide is rare and expensive, Harriman et al. also show that loading small percentages ($\approx 2\%$) of IrO_2 onto a TiO_2 support yields a better oxygen evolution rate ($\approx 3.5 \times 10^7 \text{ mol dm}^{-3} \text{ min}^{-1}$) than even bulk IrO_2 [41]. Examining the impact of the hydration state of IrO_2 , Harriman and coworkers observed that the hydrated $\text{IrO}_2 \cdot 2.08 \text{ H}_2\text{O}$ exhibits nearly as good catalytic activity as the fully oxidized material, indicating that colloidal IrO_2 particles may catalyze water oxidation.

Using the porphyrin Zn(II) tetrakis(4-sulphonatophenyl)porphyrin (ZnTSPP), Harriman et al. demonstrated that not only could porphyrin photosensitizers and colloidal iridium oxide particles (IrOx) cooperate to oxidize water, but that the initial quantum efficiency was very good, 72%. The ZnTSPP/IrOx system only works under alkaline conditions, but Pd(II) tetrakis(4-sulphonatophenyl)porphyrin (PdTSPP) was observed to exhibit even higher rates of reaction with IrOx over pH values from 3 to 9 [79]. Their results indicate that the porphyrin metal center rather than the ring structure is the predominant factor in determining the pH at which the porphyrin cooperates with IrOx to oxidize water most efficiently [79]. Harriman and coworkers developed a complete mechanistic model for the electron transfer kinetics and catalytic processes of the IrOx-Porphyrin system. These mechanisms serve as the basis for Section 4.2.2. Research using IrOx or porphyrins for the photo-oxidation of water languished for nearly a decade before being revisited by Mallouk and coworkers. Their work examines IrOx colloids with $[\text{Ru}(\text{bpy})_3]^{2+}$ photosensitizers. Mallouk and coworkers examine photocatalytic oxygen production from the IrOx- $[\text{Ru}(\text{bpy})_3]^{2+}$ system under differing buffer conditions [38], using different complexes to cap iridium oxide particles [45], and the electron transfer kinetics of the IrOx- $[\text{Ru}(\text{bpy})_3]^{2+}$ system [75]. The totality of the work described here as well as most work on photocatalytic water oxidation rely on a sacrificial electron-accepting molecule such as persulfate, a significant hurdle to incorporating an oxygen-evolving half reaction into a complete water splitting system, a problem discussed further in Section 4.7. The short-lived catalytic activity of the IrOx-porphyrin system was another problem that needed to be overcome. Better electronic coupling between the catalyst and photosensitizer can eliminate some of the corrosive side reactions that lead to the impairment of either the porphyrin or IrOx activity, an approach described in Section 4.5.

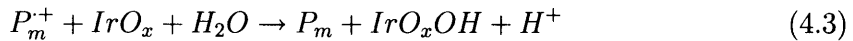
4.2.2 Mechanism of Porphyrin/Iridium Oxide Catalytic Water Oxidation

Upon absorbing a photon, a porphyrin molecule forms a singlet excited state. The singlet excited state of the porphyrin is a good electron donor but is very short lived (≈ 1.7 ns [40]), limiting the usefulness of the singlet state in intermolecular redox reactions [42]. The interactions of the paramagnetic metal cation with the porphyrin π -system enable spin-forbidden singlet-triplet transitions [39] that can yield the triplet state with very high quantum yield for certain metalloporphyrins (ZnTSPP $\phi_t = 0.85$ PdTSPP $\phi_t = 1.00$) [42]. The triplet state exhibits a much longer lifetime than the singlet state, with decay constants that are on the order of milliseconds rather than nanoseconds, providing time for intermolecular redox reactions to occur.

The porphyrin triplet excited state, P^* , reduces an electron-accepting species, such as persulfate or Ce(IV), yielding a porphyrin radical cation, P_m^+ [79]. With persulfate as a sacrificial electron acceptor, the quantum yield of P_m^+ can be doubled. Persulfate can undergo two-electron reduction to sulfate via a sulfate radical intermediate. The sulfate radical can oxidize a second porphyrin, yielding two P^+ per photon. The sulfate radical intermediate is also problematic, as reactions between the ground state porphyrin and sulfate radicals can destroy the porphyrin [79].



The catalytic oxidation of water takes place on the surface of the colloidal iridium oxide particles. Electron transfer from the IrOx surface to a porphyrin radical cation drives a hydroxyl group to bond with the IrOx, increasing the oxidation state of an Ir atom. After accumulation of four OH-groups on the catalyst surface, a dioxygen bond is formed, resulting in the release of O_2 and H_2O from the IrOx surface [79].



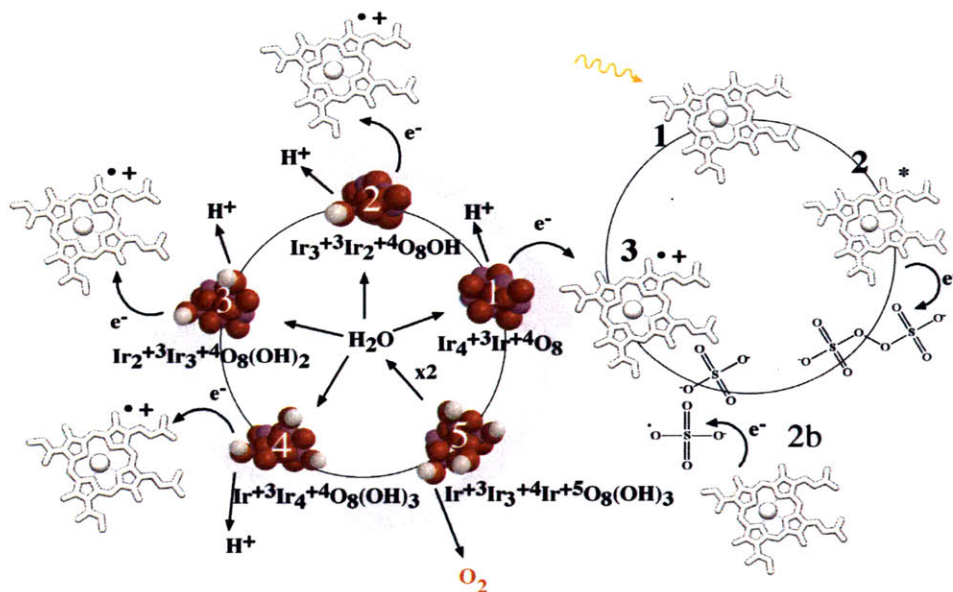
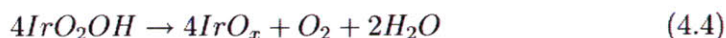


Figure 4-1: Photocatalysis of water with an IrOx colloid catalyst and porphyrin photosensitizer. The cycle on the right shows the absorption of light by the porphyrin (1), transfer of an electron to persulfate (2), and subsequent creation of a porphyrin radical cation (3). Also shown is the secondary pathway for creation of the radical cation through porphyrin oxidation by the persulfate radical anion (2b). The cycle on the left shows the accumulation of 4 OH residues on the catalyst surface and subsequent release of oxygen. Each step of the left cycle requires the product of the right hand cycle (3).



Harriman and coworkers, by studying IrOx clusters of 4 or 5 atoms, proposed a mechanism for catalysis at an IrOx surface. Iridium in the cluster is oxidized in two step: initially the cluster has an average oxidation state of +3.2, after the first step the oxidation state is +3.8, and after the second step the oxidation state is +4. When the cluster is oxidized further, one of the Ir atoms enters the +5 state, resulting in the oxidation of water. Figure 4-1 shows a schematic of the overall water splitting process.

In designing a porphyrin-catalyst couple for water photo-oxidation, there are a number of important properties that must be considered. These properties are listed

below:

- The lifetime of the radical cation must be long enough to allow electron transfer to the catalyst [42].
- The redox potential of the porphyrin radical cation should be around 1 V: lower energy will not be sufficient to oxidize Ir; higher and the colloid can be corroded [79].
- When using a persulfate electron acceptor, the concentration must be kept low, as persulfate can oxidize the ground state porphyrin, causing irreversible damage [79].
- The porphyrin:IrOx ratio is a delicate balance. If the porphyrin concentration is too high, two porphyrins can cooperate to form an Ir(VI) oxidation state, irreversibly damaging the colloid [79]. If the porphyrin concentration is too low, the oxidative equivalents needed to oxidize water will be isolated on separate particles, dramatically lowering catalytic efficiency.
- The charge relationship between the porphyrin and IrOx colloid is important. Physically adsorbed porphyrins on the surface of IrOx colloids can result in transfer of the singlet state to the IrOx and the subsequent oxidation of the porphyrin rather than water [80].

4.3 Methods for Iridium Oxide Synthesis

4.3.1 Electroporation

A technique to produce IrO₂ nanoparticles and phage-template nanowires using high voltage pulses was developed by Dr. Dong Soo Yun [114]. A Biorad electroporator, Figure 3-2, described in Section 3.4, was used to apply high voltage, high current pulses to an IrCl₃ precursor solution.

Background

The promotion of crystal growth through the application of external electrical potentials has been actively explored as a low temperature approach for materials synthesis [15, 6, 70]. Traditionally, studies of electrocrystallization have focused on processes occurring at solid/liquid interfaces and involving the production of nanoparticles or films on a solid substrate [15]. Electrocrystallization processes also typically involve long time exposure (seconds) to potentials and currents, which can also have detrimental effects on biological materials. The technique described in this section relies on short, high voltage (kV) pulses to synthesize iridium oxide nanoparticles. Using high voltage pulses enables the synthesis of colloidal nanocrystals rather than surface bound materials. Furthermore, this technique preserves the functionality of biological templates as demonstrated through the assembly of M13 bacteriophage-templated crystalline iridium oxide nanowires.

Theory

When considering traditional electrochemical reactions, the nature of the final product is governed primarily by the potential applied; to oxidize a material a more positive potential is required while the reduction requires a more negative potential. For the synthesis of nanocrystals using high voltage pulses, the chemical nature of the final product is strongly influenced by the initial pH of the precursor solution. Acidic conditions tend to initiate the formation of metallic nanoparticles, while basic conditions tend to lead to metal oxide particles.

The local environment of the metal ion is thought to play an important role in driving the reaction towards a metal versus a metal oxide. At low pH the metal precursor will be nearly completely dissociated, meaning that the ion will be weakly coordinated, making it easily reduced. In the presence of numerous hydroxyl ions, the metal ion precursor tends to complex with water and hydroxyl anions. In this case the metal ion is more strongly coordinated and also in close proximity to moieties that provide oxygen, required for metal oxide formation during electrochemical oxidation.

The importance of the groups coordinating the metal ion is indicated experimentally; the formation of oxide particles requires aging of the precursor solution after pH adjustment to allow for the complexation of the hydroxylated metal ion.

The chemical nature of the product may be determined by the production of strongly reducing or oxidizing intermediate products: formation of molecular hydrogen gas at low pH and at high pH the formation of OH radicals, H_2O_2 , and molecular oxygen gas. These intermediate products then may chemically oxidize or reduce the metal ion precursor. Experimentally, the complete formation of metal oxide or metal particles takes a short period of time after electropulsing, suggesting that chemical oxidation or reduction of the metal ion precursors may play an important secondary role in the synthetic process.

Crystalline phases can be promoted when the conductivity or permittivity of the crystalline phase leads to lower overall electrical energy than amorphous or polycrystalline phases, resulting in an energetic driving force towards the crystalline phase, a phenomenon well characterized as a means of synthesizing macroscale crystals from saturated solution [92, 96]. A simulation comparing spherical amorphous vs. crystalline iridium oxide particles in a large electric field (COMSOL) indicates that the energy of forming the crystalline phase is about 2% lower than the amorphous phase. In the synthesis of iridium oxide nanoparticles, the applied electrical signal serves three functions: 1) the oxidation or reduction of aqueous precursors; 2) the nucleation of particles; and 3) the promotion of crystalline phases.

Synthesis

Iridium oxide was synthesized from aqueous IrCl_3 precursor. At low pH, applying electrical pulses to the IrCl_3 precursor resulted in metallic Ir nanoparticles, but by neutralizing the IrCl_3 solution with NaOH and incubating for several days, crystalline IrO_2 was synthesized. Immediately upon the application of electric pulses, the solution changed color from brown to purple, with an absorbance peak appearing near 600 nm. The absorption spectrum indicated that the peak at 600 nm increased with increasing voltage, suggesting higher yield and larger particles. This conclusion was


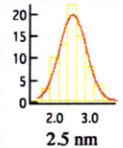
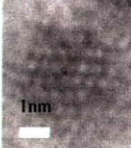

Precursor	Experimental Parameters		Color Change	Particle Size Distribution, Average Size	TEM
	Potential, kV	pH, before pulses	Precursor		
Product	# of Pulse	pH, after pulses	After Pulsing		
25 mM IrCl_3	1.0	7.5			
IrO_x	40	-			

Table 4.1: The conditions for synthesizing IrO_2 nanoparticles using electric pulses. The TEM image was taken by D. S. Yun.

confirmed by transmission electron microscopy (TEM). From the TEM micrograph, it was observed that the radius and size distribution of nanoparticles formed at 0.7 kV (10 pulses) was less than those at 1.0 kV (30 pulses). Elemental mapping by energy dispersive X-ray analysis (EDX) of the samples pulsed at 1.0 kV confirmed the formation of crystalline IrO_2 . Table 4.1 shows the conditions, color change, particle distribution, and TEM of IrO_2 nanoparticles created by the pulse technique.

Iridium oxide nanowires were synthesized by this electropulse method using a bacteriophage expressing the IrO_2 -binding sequence AGETQQAM [113] on the PVIII coat protein as a template. The procedure Yun used to select this clone is described in Appendix A.4. Bacteriophage displaying the IrO_2 -binding sequence on their major coat protein were mixed with the neutralized IrCl_3 precursor and exposed to electrical pulses. Immediately upon pulsing, the color of the solutions turned purple, indicating the formation of IrO_2 . Phage incubated with the precursor but with no electrical pulses for nearly 6 months exhibited no color change, indicating the electric field is necessary for oxidation of the IrCl_3 precursor and subsequent assembly of IrO_2 nanowires. After 10 pulses the phage exhibited a uniform distribution of IrO_2 nanocrystals along the viral length, but there was not 100% coverage of the viral surface as revealed by electron microscopy. After 30 pulses the entire bacteriophage

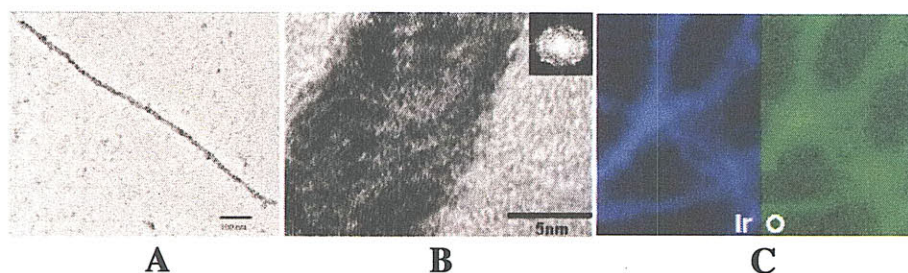


Figure 4-2: TEM images of (A) a single IrO₂ nanowire, (B) a HRTEM closeup showing the crystalline structure of the nanowire, and (C) EDX mapping showing the distribution of Ir and O atoms on the phage surface. TEM image A by Y. S. Nam and images B and C by D. S. Yun.

capsid is uniformly coated with IrO₂ nanocrystals. Plasmon elemental mapping and X-ray line scanning analysis of AGETQQAM-derived nanowires confirmed IrO₂ formation and verified that the wires are highly crystalline. These results indicate that the displayed peptide plays an important role in mediating the assembly of IrO₂ on the phage surface during the electrical pulse. Furthermore it is evident that the functionality of the M13 phage remains intact even under the high field conditions of this work. Figure 4-2 shows a single IrO₂ nanowire, a close-up showing the crystalline structure of the nanowires, and EDX elemental mapping. TEM analysis was performed by D. S. Yun.

Scale Up

The electropulse technique, while producing homogeneous, crystalline nanoparticles only yields 200 μ L of nanoparticles per batch, severely limiting their utility for applications such as photocatalytic water splitting. To produce larger quantities of nanoparticles, the Biorad electroporator was modified to enable the continuous application of electric pulses. The modification is described in Appendix C.7. Two different techniques were employed to produce larger quantities of nanoparticles. The first employed a syringe pump to flow precursor solution between co-axial electrodes. The intent was to control the flow rate such that the precursor solution would experience the appropriate number of pulses while transiting through the electrode setup.

Unfortunately, the application of the high voltage pulses caused significant electrically induced capillary flow, with fluid remaining between the coaxial electrodes for less than a single pulse.

The second technique for large batch electropulse production of IrO_2 involved placing two parallel plate electrodes, separated by a 2 mm gap, in a bath of precursor. The bath was stirred, circulating the precursor solution between electrodes during the continuous application of high voltage pulses. Several electrode materials were tested as the working and counter electrode. Non-noble metals such as aluminum and stainless steel oxidized rapidly under the influence of the high voltage pulses. Pt and Ir metal both worked well as working electrodes with a gold counter electrode, with Ir yielding particles about twice as fast as Pt, exhibiting a color change after 10 minutes for the Pt electrode and after only 5 min with an Ir electrode. TEM analysis (not shown) indicated some very large clumps of nanoparticles, but predominantly similar morphology for both nanowire and nanoparticles synthesized by the large batch method as synthesized using electroporation cuvettes. Figure 4.2 shows the two setups for larger batch production of IrO_2 nanoparticles using the electropulse technique. Typical conditions for the synthesis using the stirred cell technique are described in Appendix C.8.

Oxygen Evolution

The photocatalytic oxygen production of IrO_2 nanoparticles synthesized using Ir/Au electrodes in a stirred cell was tested using the ZnTSPP porphyrin as a photosensitizer and a borate buffer. The oxygen level was monitored using an electrochemical (Clark membrane) dissolved oxygen probe, detailed in Section 4.4.1. The experimental conditions for oxygen evolution are described in Appendix C.9. The oxygen production from the electro-pulse synthesized nanoparticles is shown in Figure 4.3. The results indicate a significant level of oxygen production when the sample is illuminated; however, these results were not easily reproducible because of oxygen diffusion into the system.

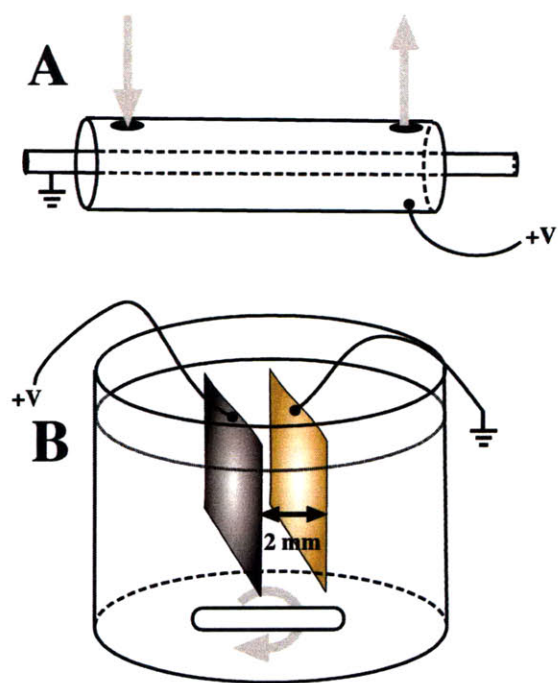


Table 4.2: Diagrams of (A) the cylindrical flow cell designed for continuous production and (B) the stirred cell for larger batch production of IrO_2 nanoparticles using HV electropulses.

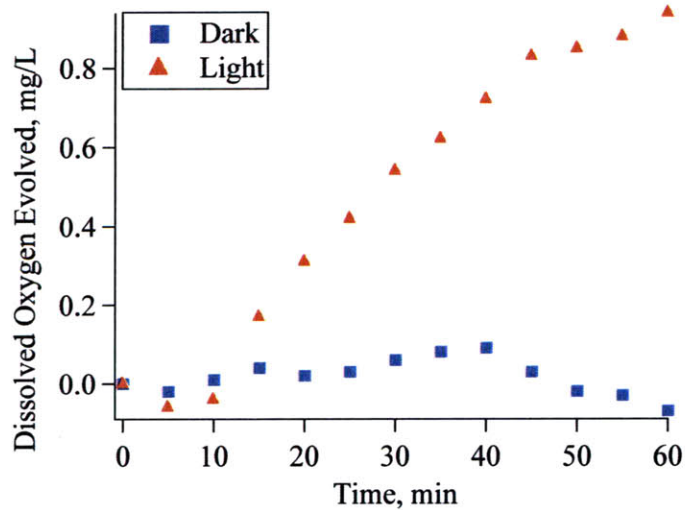


Table 4.3: Comparing the dissolved oxygen produced from electro-pulse synthesized nanoparticles with ZnTSPP in the dark and when illuminated.

Drawbacks of the Electropulse Synthesis

While the particles synthesized electrically by pulsing Ir salt precursor are crystalline and fairly uniform, the synthesis has several drawbacks. First, the aging step of the IrCl_3 precursor is very important and often not completely predictable. Typically, adjusting the pH of the IrCl_3 solution to 7.5 and then allowing the solution to age for several days produced good quality nanoparticles; however, sometimes upon pulsing no color change was observed. The initial pH of the solution or the precise incubation conditions may be important parameters governing the properties of the final synthesis. Additionally, while the continuous pulse system coupled with a stirred reaction vessel can dramatically increase the quantity of particles that can be synthesized, the precious metal electrodes foul very easily. As IrO_2 is being synthesized, Ir metal is deposited on the gold counter electrode. The deposition of iridium significantly attenuates nanoparticle yield and is nearly impossible to remove from the gold foil surface. Similarly the Ir metal working electrode forms an oxide coating over time that causes the nanoparticle reaction to cease. Lastly, this synthesis already requires very high voltages and very high currents, so further scaling of the synthesis would require extremely dangerous electrical conditions.

Alternative Electrochemical Synthesis

An alternative electrochemical synthetic approach for producing higher oxidation state iridium ion complexes based on the approach of Castillo-Blum et al. was attempted [18]. The materials synthesized by this electrochemical approach exhibited no oxygen production using a ZnTSPP porphyrin photosensitizer and oxygen production measured with the electrochemical dissolved oxygen probe.

4.3.2 Chemical Synthesis

Harriman and coworkers synthesized iridium oxide (IrOx) colloids synthetically using H_2O_2 as an oxidant and sodium citrate to stabilize the particles [40]. Harriman et al. remove excess citrate with a polymer resin and then cap the IrOx particles with

a 20kD MW PEG molecule. PEG was eliminated from most syntheses employed for the work described herein to enable peptide interaction with the IrOx colloids.

Colloid Size: DLS and Dialysis

Harriman et al. do not report the resultant particle size from the chemical synthesis technique described in their paper, they only state that the particles are larger in size and have a greater size distribution than 4-5 Ir atom colloidal clusters they prepare radiolytically. Dynamic light scattering (DLS) and dialysis of the IrOx colloids against different pore size membranes were used to assess the particle size of IrOx colloids synthesized without a PEG cap. A small number of large particles scatter more light than many small particles, so to examine the particle size of the smallest colloidal particles only the first ≈ 10 ms of the correlation decay was considered. DLS measurements were made using a DynaPro Titan Dynamic Light Scatterer. IrOx colloid samples were centrifuged prior to measurement to remove large particles. Fitting the correlation decay yields a particle size of 0.2 nm, with a distribution of less than 0.1 nm. A 0.2 nm particle corresponds to a cluster that is around 4-5 atoms, the same size as Harriman et al. report from the radiolytic preparation.

The IrOx colloid without PEG was dialyzed using 500 MW, 1000 MW, 2000 MW, 3500 MW and 10000 MW tubing. 1000 MW tubing has a pore size that is about 0.2 nm while 10000 MW tubing has a pore size that is about 1.5 nm. Table 4.4 shows the results of the dialysis experiments. Iridium oxide concentration was measured using ICP-AES (Jobin Yvon). The percentage-loss values reference the Ir concentration measured for the 500 MW dialysis tubing, assuming that only Ir ion salts dialyze out of the 500 MW. A 25 % drop in Ir concentration is seen between the 500 and 1000 MW dialysis tubing, suggesting that around 25 % of the colloid is below 1000 MW. While the MW labels of dialysis tubing refer to molecules such as peptides, 1000 MW is in good agreement of the MW of IrOx clusters containing 4 (896 MW) or 5 (1120) iridium atoms.

Table 4.4: Dialysis of IrOx Colloids using differing MW cutoff dialysis tubing.

MW Cutoff	Ir Conc, PPM	% Ir Loss
500	2.1×10^{-6}	- %
1000	1.6×10^{-6}	25 %
2000	1.5×10^{-6}	25 %
3500	1.6×10^{-6}	25 %
10000	1.6×10^{-6}	25 %

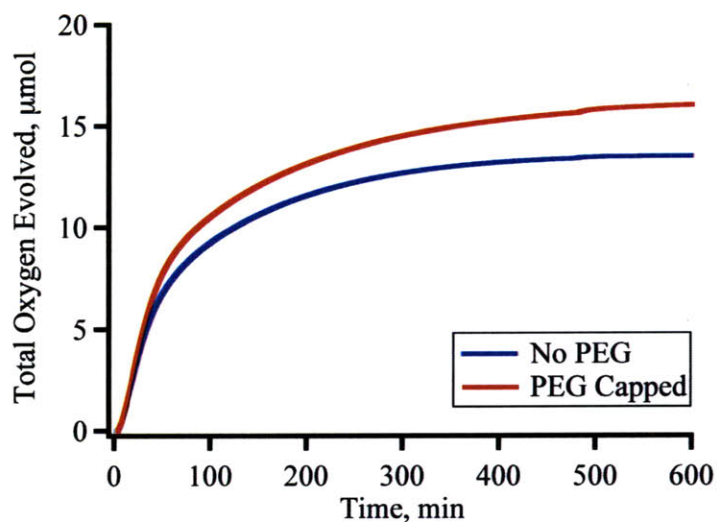


Figure 4-3: The oxygen production from IrOx colloids synthesized with and without a PEG capping molecule. Measured using the ZrO2000 analyzer, described in Section 4.4.3.

Oxygen Evolution: Colloids without PEG

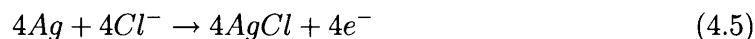
The difference in catalytic performance of the IrOx colloids with and without PEG is slight, Figure 4-3, though colloids were less stable without the PEG layer so were used within one week of synthesis. The chemical synthesis technique is detailed in Appendix C.10.

4.4 Methods for Continuously Quantifying Oxygen Production

Techniques such as gas chromatography can provide precise quantification of the oxygen concentration of a sample, but only provide single point measurements. A continuous oxygen measurement provides information about the kinetics of photocatalytic oxygen evolution, potentially revealing the limitations or benefits of particular experimental conditions. Three different techniques were investigated for continuous measurement of oxygen evolution: dissolved oxygen was measured using electrochemical and fluorescent probes, while gaseous oxygen was measured using a solid state zirconia analyzer.

4.4.1 Electrochemical Oxygen Detection

A VWR symPHony dissolved oxygen meter was used to measure the dissolved oxygen evolved from ZnTSP and IrOx. The probe used by the VWR meter is a polarographic electrode of the Clark-type. The sensor consists of two electrodes: an Ag/AgCl electrode and a Pt electrode, a KCl electrolyte, and a membrane such as polypropylene through which oxygen diffuses. The electrodes, when polarized with a potential of -600 mV vs the Ag/AgCl electrode, produce a current that is proportional to the oxygen concentration [27]. From the redox reactions at the Ag/AgCl anode, Equation 4.5, and the Pt Cathode, Equation 4.6, it is transparent that current flow between the electrodes relates to the partial pressure of oxygen.



As shown in Figure 4.3, the electrochemical measurement of dissolved oxygen can be used to probe the photocatalytic oxygen of water. Several problems occur with this technique, however. The most serious problem is that when chemically synthesized

IrOx colloids rather than electropulse synthesized IrO₂ nanoparticles were employed, anomalous results occurred, perhaps caused by diffusion of IrOx colloids across the membrane and subsequent redox reactions between the electrodes and the colloids. For unknown reasons, the dissolved oxygen system exhibited large sample to sample variation. Measurements of dissolved oxygen were plagued by leakage of atmospheric oxygen into the system. The leakage problem was minimized by performing dissolved oxygen measurements in a glove box, but remained problematic.

4.4.2 Luminescent Oxygen Measurement

Luminescent measurement of dissolved oxygen was performed with either a Hach LDO dissolved oxygen probe with sc100 meter or an Ocean Optics fiber optic luminescent oxygen detector. Each of these setups detects oxygen in the same manner, monitoring the change in lifetime of an oxygen-sensitive transition metal complex immobilized in a sol gel or polymer matrix. Molecular oxygen quenches the fluorescence of the transition metal dye with the resulting decrease in lifetime and intensity as a function only of O₂ concentration [17]. The Stern-Volmer equations can be used to determine the dissolved oxygen concentration based on the lifetime or intensity. The LDO detectors illuminate a ruthenium complex with a blue light source and measure the fluorescence decay using a photodiode.

The Hach LDO probe, Figure 4-4, was used to measure effectively the oxygen evolved photocatalytically from a solution of IrOx colloid and ZnTSPP, Figure 4-5. For measurement, the solution was in a large crystallization dish placed in a glove bag. A substantial quantity of reactants was required to accommodate the large size of the Hach probe. The probe exhibited good response to dissolved oxygen, though the large volume of sample required to make a measurement limited the utility of the probe.

The Ocean Optics system uses a bifurcated fiber to illuminate and measure emission from a RedEyeTM patch, a sticker containing a Ru-based oxygen responsive dye. The RedEye sticker is adhered to the inside of the sampling vessel, while the probe can illuminate and measure from outside the vessel. The advantage of the Ocean Op-



Figure 4-4: The Hach LDO dissolved oxygen probe, with the fiber lamp used to illuminate the sample.

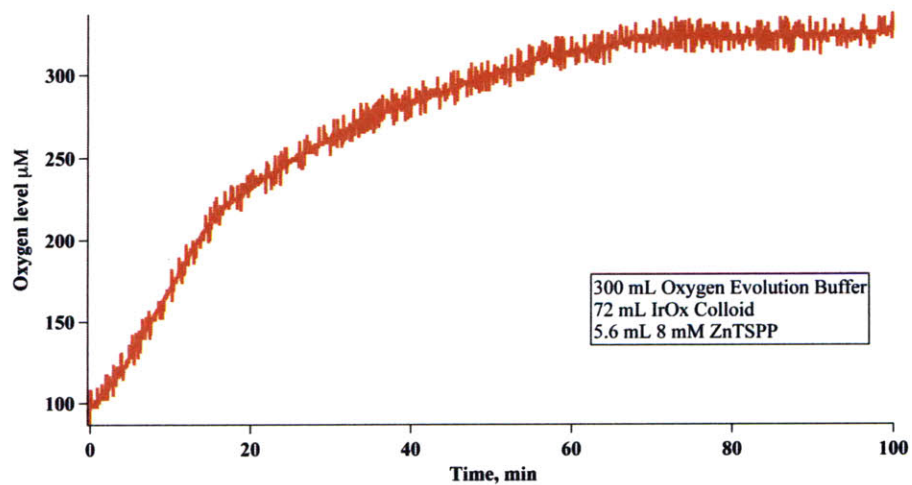


Figure 4-5: Oxygen evolution from IrOx and ZnTSPP measured using the Hach dissolved oxygen probe.

tics system is that it can be used in a continuous flow cell type geometry, enabling a setup where the oxygen-evolving solution is illuminated, oxygen is evolved, and then the non-sacrificial electron-accepting molecule can be electrochemically regenerated.

The Ocean Optics system had a number of problems that had to be overcome. The blue light used to excite the RedEye patch also interacted with the porphyrins in solution, either bleaching the porphyrin or stimulating oxygen production. This problem was overcome by coating the surface of RedEye patch exposed to the solution with a black silicone adhesive. The silicone adhesive is permeable to oxygen but blocks the light from interacting with the porphyrins in solution. Unfortunately, the silicone adhesive traps oxygen, dramatically increasing the time that a sample must be purged before measurement and reducing response times. The RedEye patches also have surface non-uniformities and patch to patch variation, resulting in fluctuations in lifetime and intensity measurements based on the exact positioning of the fiber in relation to the RedEye patch rather than oxygen concentration. Because of these problems, while qualitative observations in the change in oxygen level between a sample before and after illumination could be made, absolute measurements of oxygen concentration could not be achieved. Many of the problems relating to probe alignment may be overcome using a probe that has the coating directly on the tip of the probe, such as the Ocean Optics FOXY or FOSPOR probes. The FOXY and FOSPOR probes would still require a polymer overcoat to prevent leakage of light from the probe into the sample, limiting the response time of the probe.

4.4.3 Zirconium Based Gaseous Oxygen Analyzer

Gaseous oxygen concentration can be measured using a solid state oxygen analyzer employing a high temperature zirconia sensor to measure oxygen concentration. When heated to high temperature (≈ 700 °C), charged oxygen vacancies form in the zirconium oxide matrix. Introduction of molecular oxygen fills these vacancies, altering the electrostatic field in the zirconia [13]. Oxygen detectors using zirconia expose one end of the sensor to air while the other end is exposed to the sample being measured. Differences in oxygen level between the two halves of the sensor create a

voltage difference between two electrodes. The sensitivity range is very large, from ppb levels of O_2 all the way to 100% oxygen. The zirconia sensor is sensitive to reducing species, which can bind to oxygen atoms in the zirconia matrix, thereby reducing the apparent oxygen level, so care must be taken when measuring oxygen to eliminate all reducing gases, including water.

High purity nitrogen gas was bubbled through samples to collect oxygen from the aqueous colloidal mixture and transport the oxygen to a gaseous oxygen analyzer. Oxygen concentration was measured using a ZrO2000 Oxygen Analyzer (Alpha Omega Instruments). To compute the exact quantity of oxygen evolved, careful control of the flow rate is needed. The flow of gas was maintained at 0.2 L/min using a flow controller (Alicat Scientific). Water in the gas mixture can react with the sensor surface, providing an artificially low value for oxygen production. To remove water, the gas was dried using a Nafion exchange gas dryer (Permapure). Nafion membranes are permeable to hydrophilic substances such as water, but impermeable to oxygen and nitrogen. The gas dryer consists of a Nafion tube with the sample flowing internally and a dry nitrogen stream flowing at a high rate externally, causing any water in the sample gas stream to diffuse through the Nafion membrane. Figure 4-6 shows the complete setup of the oxygen analyzer. Appendix C.12 has some comments on data collection from the ZrO2000 analyzer.

The ZrO200 oxygen analyzer was used to quantify oxygen production for all experiments in Sections 4.5, 4.6, and 4.7. For some samples, illumination resulted in a drop in the observed oxygen level, suggesting the presence of a reducing species. While it is possible that a small amount of hydrogen was evolved in samples for which this drop in oxygen was observed, it is unlikely. Samples for oxygen evolution are mostly at high pH, making H_2 production energetically unfavorable. It is hypothesized that the drop in signal that is observed is due to production of oxygen radicals or hydroxyl radicals due to insufficient electron-accepting complexes.

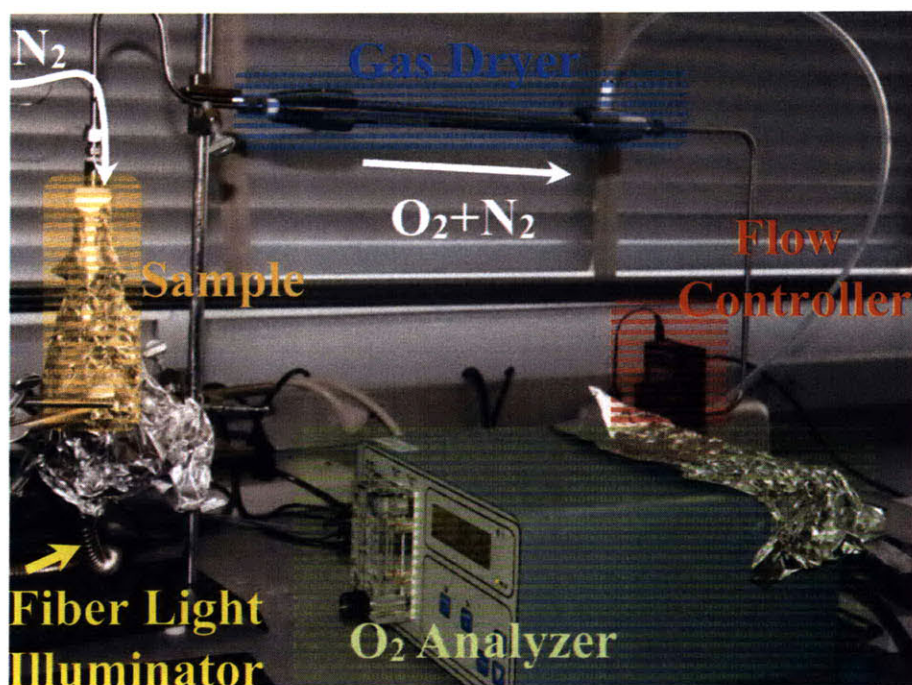


Figure 4-6: Oxygen was collected from samples by a stream of nitrogen and quantified using a gaseous oxygen analyzer.

4.5 Multi-scalar Framework For Oxygen Evolution

As described in Section 1.3.1, nanoscaled arrangements of chromophores can exhibit quantum mechanical effects that result in the highly efficient capture of light. Furthermore, for colloidal photocatalysis, the separation between the photosensitizing molecule and iridium oxide (IrOx) is critical to efficient electron transfer. Co-assembly of IrOx catalyst and Zn(II) porphyrin on the major coat protein of M13 bacteriophage provides a nanostructured porphyrin array with porphyrins in close proximity but not physically adsorbed on the IrOx catalyst. To assay the benefits of nanostructural assembly of porphyrins and porphyrin proximity to IrOx, the photocatalytic performance of the porphyrin/IrOx nanowires was compared to that of untethered porphyrins and IrOx colloids.

The colloidal stability of the porphyrin wires during photocatalysis is poor. Inspired by the immobilization of many PSII structures within a single chloroplast, the photocatalytic nanowires were assembled inside of polymer microgels. The polymer microgel enabled the regeneration of the IrOx catalyst using H_2O_2 .

The work in this section was a collaboration with Mr. Yoon Sung Nam. Most of the synthesis and characterization work of the phage nanowire structures was performed by Mr. Nam. The polymer microgels were synthesized by Prof. Daeyeon Lee.

4.5.1 Porphyrin/IrOx Nanowires

Each pVII protein on the M13 bacteriophage has two exposed lysine residues. Using carbodiimide chemistry, the porphyrin Zn(II) Deuteroporphyrin IX 2,4-bis-ethylene glycol (ZnD630-9) was coupled to primary amines on these lysine residues, creating porphyrin nanowires. ZnD630-9 was selected because it has similar optical and electrochemical characteristics to ZnTSPP and has pendant carboxylic acid groups enabling covalent coupling to primary amines. The number of porphyrins per virus was determined using ICP-AES to measure Zn and P, Section C.13, with Zn concentration corresponding to the number of porphyrins and P concentration (from DNA),

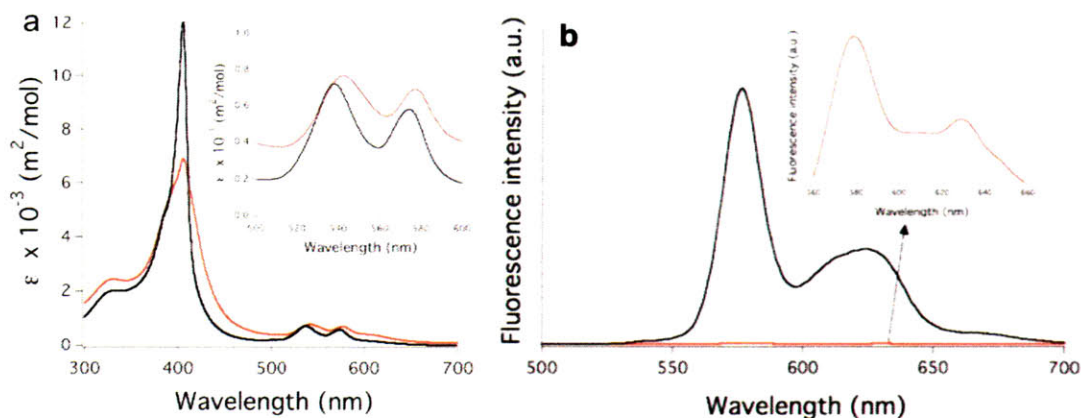


Figure 4-7: (a) Absorbance and (b) fluorescence of ZnD630-9 and ZnD630-9 conjugated to the M13 bacteriophage.

correlating to the number of viruses. The ICP measurement yielded a 0.39:1 Zn:P ratio, corresponding to ≈ 2700 porphyrins per phage or about 1 porphyrin per pVIII protein.

Conjugation of ZnD630-9 to the bacteriophage resulted in a decrease in intensity and broadening of the ZnD630-9 Soret band at 406 nm and broadening and red shift of the ZnD630-9 Q bands from 538 nm and 574 nm to ≈ 541 nm and 579 nm. The absorbance spectrum, measured by Y. S. Nam, is shown in Figure 4-7 a. The broadened absorbance is likely a result of porphyrin molecules experiencing slightly different local environments, while the Q-band red shift is commonly observed from porphyrin aggregates [98]. The fluorescence of the ZnD630-9 nanowires was nearly completely quenched, Figure 4-7 b. The fluorescence quenching may indicate that singlet states are converted more efficiently to triplet states when the porphyrins are assembled on the virus. The nanoscale assembly of porphyrins may enable cross-porphyrin singlet-triplet transitions.

Porphyrin - IrOx nanowires were assembled by coupling ZnD630-9 to bacteriophage containing the IrOx-binding sequence, AGETQQAM, and then incubating the porphyrin-virus conjugates with IrOx colloid, synthesized as described in C.10. Dual-functional nanowires with different IrOx:ZnD630-9 ratios were synthesized by vary-

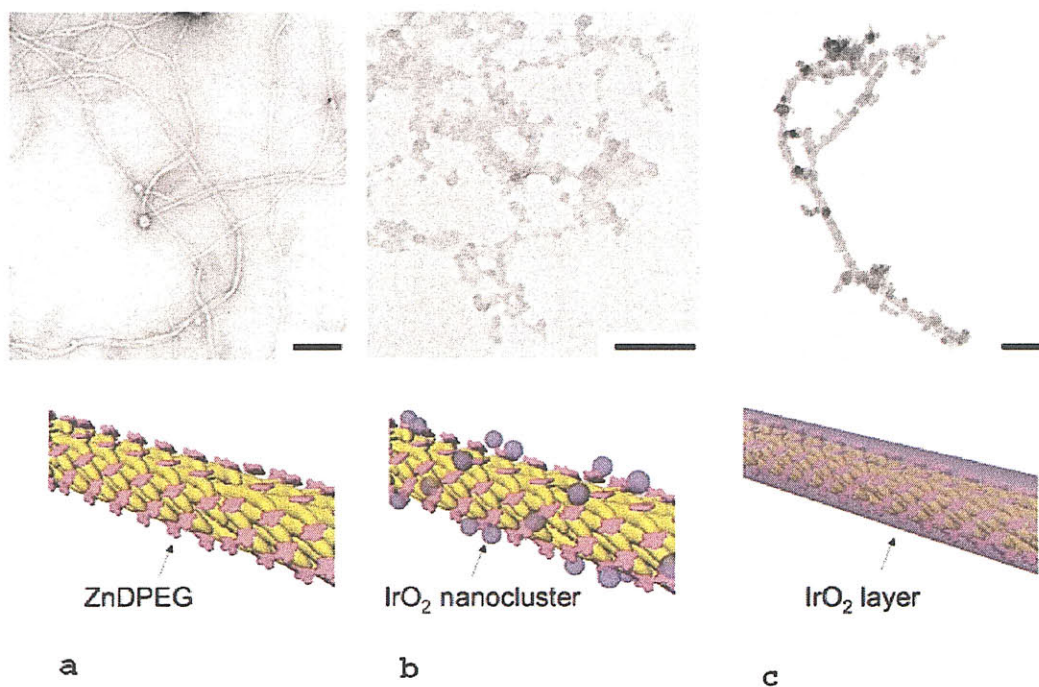


Figure 4-8: (a) Negatively-stained porphyrin nanowires, (b) 1:15 IrOx:ZnD630-9 nanowires, and 1:224 IrOx:ZnD630-9 nanowires. TEM images by Y. S. Nam

ing the amount of IrOx clusters while fixing the ZnD630-9 concentration. Figure 4-8 shows cartoons and TEM images of ZnD630-9 nanowires and hybrid IrOX-ZnD630-9 nanowires with different IrOx:ZnD630-9 ratios.

4.5.2 Oxygen Evolution from IrOx/ZnD630-9 Nanowires

The catalytic properties of the virus-templated IrOx/porphyrin nanowires was assessed by measuring the oxygen evolved upon illumination. The experimental conditions for oxygen evolution are described in Appendix C.14. For these experiments sodium persulfate was used as a sacrificial electron acceptor to quench the triplet excited state. Figure 4-9 a compares the total oxygen evolved from IrOx colloids and ZnD630-9 when freely dispersed in solution to that evolved from nanowire structures. Figure 4-9 b compares the total oxygen evolved from hybrid IrOx/ZnD630-9 nanowires with different IrOx:ZnD630-9 ratios.

Conditions	TON	TOR, s ⁻¹
ZnD630-9 and IrOx	179	0.07
ZnD630-9 and IrOx Phage	76	0.07
ZnD630-9 Phage and IrOx	313	0.35
1:41 ZnD630-9/IrOx Phage,	796	0.85
1:15 ZnD630-9/IrOx Phage	1143	1.57

Table 4.5: TON and TOR

The turnover number (TON) and turnover rate (TOR) provide metrics for assessing the performance of the catalyst. TON is the total number of water molecules the catalyst splits, while TOR is the number of water molecules the catalyst splits per unit time per surface active site. TOR was calculated based on the steady state rate of O₂ production, with an assumption that only 53% of Ir atoms are exposed on the surface of the catalyst [82]. Table 4.5 summarizes TON and TOR for different experimental conditions. The IrOx colloid and nanowires with uncoupled ZnD630-9 had similar turnover rates, but the IrOx nanowires had a lower turnover number, perhaps because of the smaller surface area of the nanowire geometry. The IrOx colloids with ZnD630-9 nanowires exhibited substantially higher turnover rates and superior turnover numbers, perhaps due to more efficient conversion of light energy into triplet states and radical cations. The coassembly of IrOx and ZnD630-9 on a bacteriophage template yielded the highest turnover rate and turnover number, suggesting that the close proximity of the dye and catalyst particles enhances electron transfer from the IrOx to the porphyrin radical cation. The ratio of IrOx to ZnD630-9 also proved important, with thinner IrOx shells exhibiting better catalytic performance. Since four oxidative equivalents must be accumulated in a localized region, it is possible that more IrOx simply results in greater dispersion of the accumulated charge across the iridium oxide surface. Alternatively, the photolysis of water requires an interface between dye, catalyst, and water. If the thickness of the catalyst is too great, charge may be trapped internally and unable to promote the splitting of water.

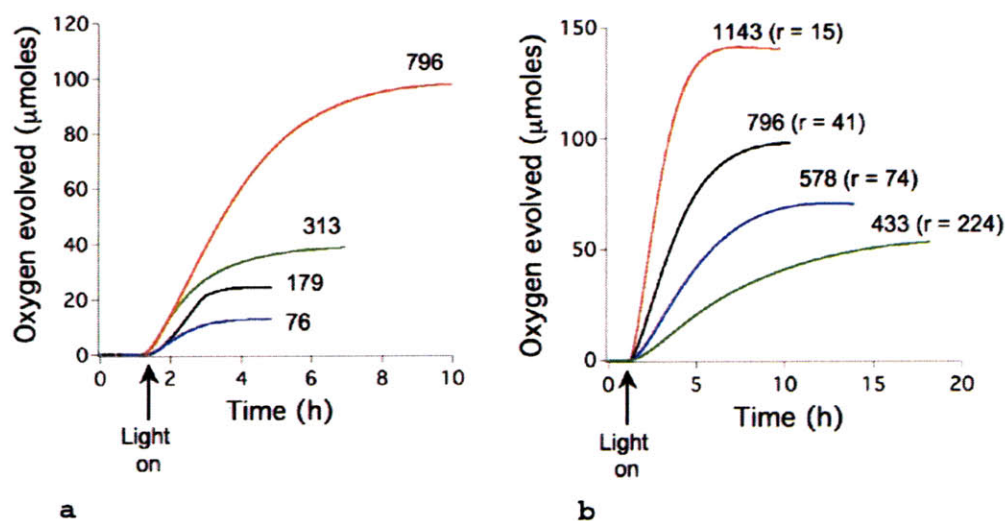


Figure 4-9: (a) Total oxygen production for IrOx with ZnD630-9 (black), IrOx mixed with wild type ZnD630-9-conjugated viruses (blue), virus-templated IrOx nanowires with ZnD630-9 (green), and ZnD630-9/IrOx hybrid nanowires (red). (b) Total oxygen production from IrOx/ZnD630-9 hybrid nanowires with different IrOx:ZnD630-9 ratios: 15 (red), 41 (black), 74 (blue), and 224 (green). The TON is recorded above each curve.

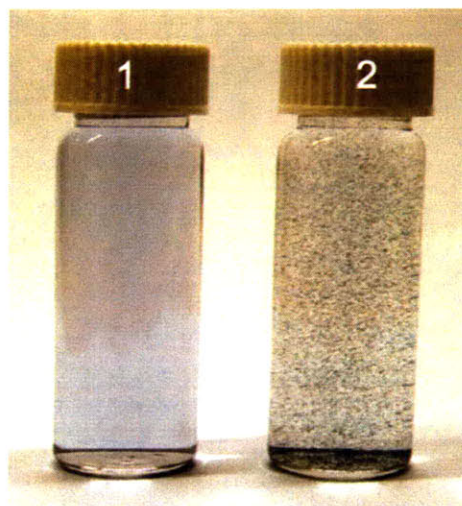


Figure 4-10: Hybrid IrOx/ZnD630-9 nanowires before and after oxygen evolution. (10 hours)

4.5.3 Quantum Yield

To determine the quantum yield for oxygen evolution of IrOx/ZnD630-9 nanowires and IrOx colloids with unbound ZnD630-9, samples were illuminated with a 150 Watt halogen lamp with a 550 nm bandpass filter giving a light intensity of 200 mW/cm². The total light absorbed by the porphyrin at this wavelength was measured using a light intensity meter. The quantum yield (ϕ) of 15:1 IrOx-ZnDPEG nanowires was ≈ 0.86 when a Rayleigh scattering approximation is assumed. The quantum yield is higher than that of IrOx nanoparticles with free ZnDPEG: $\phi \approx 0.47$. The higher quantum yield may be due, in part, to higher yield singlet to triplet state transitions because of the nanoscale assembly of the porphyrin molecules.

4.5.4 Microgels

During oxygen evolution there is substantial aggregation of IrOx/ZnD630-9 hybrid nanowires, Figure 4-10. To overcome the aggregation problem, the hybrid nanowires were encapsulated in a polymer hydrogel matrix. The polymer matrix immobilizes the IrOx/ZnD630-9 nanowires, preventing aggregation while maintaining a hydrated

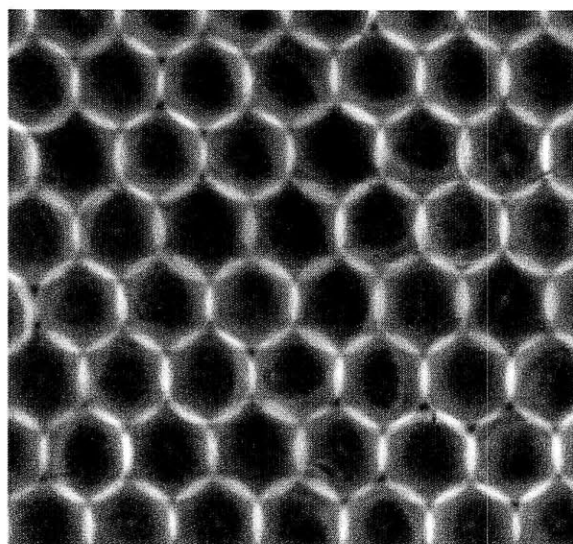


Figure 4-11: An ordered array of polymer microgels.

environment. Polyacrylamide microgels formed via a microfluidic technique [57] were used to encapsulate bacteriophage, Figure 4-11. The microgels were used as microreactors to assemble ZnD630-9 and IrOx on the encapsulated bacteriophage. Microgels were prepared encapsulating nanowires with 35:1 and 109:1 IrOx:ZnD630-9 ratios as determined by ICP-AES analysis. As with un-encapsulated nanowires, the lower IrOx:ZnD630-9 ratio microgels exhibited greater oxygen production, Figure 4-12 a.

As oxygen is evolved photocatalytically, the electron acceptor is consumed and protons are produced, lowering the pH of the oxygen-evolving buffer. Another advantage of encapsulating the catalytic material is that the catalytic microgels can be removed from the oxygen evolution buffer, the catalyst material regenerated, and the buffer replaced. After 90 minutes of illumination, microgels were removed from the buffer solution by centrifugation and re-suspended in 0.2% hydrogen peroxide to re-oxidize the catalyst. Based on TON, the second cycle yielded 94% of the oxygen evolved in the first cycle. By the fourth cycle the yield decreased to 56% of the oxygen in the first cycle, Figure 4-12 b. The combined TON after 4 reaction cycles was \approx 1.6 times higher than the TON from microgel encapsulated hybrid nanowires with no regeneration.

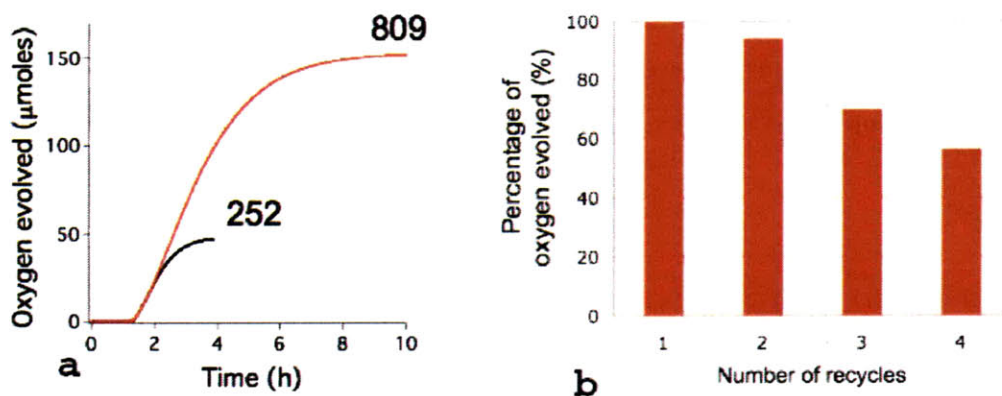


Figure 4-12: (a) Turnover numbers from encapsulated hybrid nanowires with two different IrOx:ZnD630-9 concentrations. (b) Relative oxygen production upon multiple cycles of catalytic microgel regeneration.

4.6 The IrOx Peptide

The results described in Section 4.5 indicate that the nano-scaled assembly of porphyrins on the bacteriophage play a predominant role in the improved catalytic efficiency of the hybrid nanowire system. Questions still remain, however, as to the role of the IrOx-binding peptide in improving catalytic performance. The peptide performs an important role in assembling IrOx such that it is in close proximity to the porphyrins, but it may also promote electron transfer between the porphyrin and the IrOx colloid. The conjugation of IrOx by the peptide may even decrease the catalytic efficiency of the colloid, a factor that could go unnoticed because of the performance gains achieved through the co-assembly of IrOx with the porphyrins. A better understanding the role of the peptide in promoting water splitting could enable further enhanced catalytic performance through rational design of peptides that can coordinate IrOx better, facilitating catalytic activity or electron transfer.

4.6.1 Characterization of the IrOx Binding Peptide

To understand the interactions between the peptide and the IrOx colloid, NMR, FTIR and HPLC were used to examine interactions between a synthetic IrOx-binding

peptide, KGGG-AGETQQAM, and the IrOx colloid. The IrOx-binding sequence was synthesized with a tri-glycine linker to a terminal lysine to allow carbodiimide conjugation to porphyrins. The N-terminus of the synthetic peptide was acetylated.

NMR

For 1D and 2D NMR characterization, the IrOx-binding peptide was dissolved in D₂O and IrOx colloid was synthesized in D₂O using D₂O₂ as an oxidant. Watergate techniques were used for solvent suppression for both 1D and 2D NMR techniques. The 1D NMR of the IrOx-binding peptide is shown in Figure 4-13. Peak assignments were made through examination of the 2D gCOSY spectrum, Figure 4-14, a technique probing through-bond interactions. The NMR spectra of the IrOx-binding peptide, IrOx-colloid and the IrOx-binding peptide mixed stoichiometrically with the IrOx colloid are shown in Figure 4-15. The NMR spectra of the IrOx colloid exhibits narrow peaks without using any solid-state NMR techniques, indicative of the small size of the IrOx clusters. Upon addition of the peptide to the IrOx colloid three differences are observed from the colloid and peptide spectra alone. First, the methionine CH₃ peak in the mixed system is lower in intensity in relation to the acetyl CH₃ peak, and additionally, a new peak appears in the mixed system at 2.678 ppm. If the IrOx clusters coordinate with the methionine sulfur atoms, this may lead to decreased electron density on the methionine causing a downfield shift in the methionine peak. In addition to this putative methionine shift, the IrOx colloid peaks labeled “A” in Figure 4-15 disappear in the mixed system, while new peaks, labeled “B”, appear, which may indicate coordination of the IrOx colloid by the IrOx-binding peptide.

To further probe the interactions between the IrOx-binding peptide and IrOx colloid, 2D gROESY NMR spectroscopy was used to probe through-space interactions between protons. The gROESY spectrum of just the IrOx-binding peptide, Figure 4-16, revealed no through space interactions due to interactions beyond primary peptide structure. In the gROESY spectrum of the mixed IrOx colloid/IrOx-binding peptide system, Figure 4-17, several new features emerge. The putative M CH₃ peak at 2.67 ppm appears to interact with the M CH₂ and Q CH₂ peaks at about 1.9 and 2.1

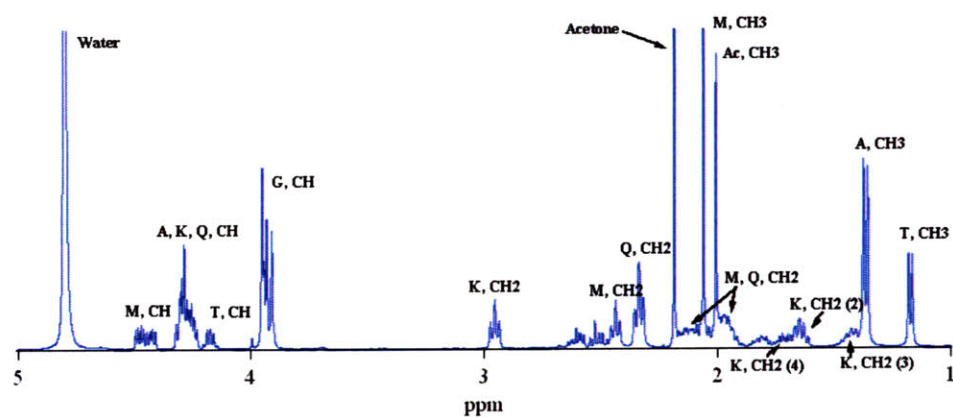


Figure 4-13: A 1D NMR spectrum of the IrOx-binding peptide, KGGG-AGETQQAM. Peaks have been assigned using 2D-gCOSY NMR, Figure 4-14.

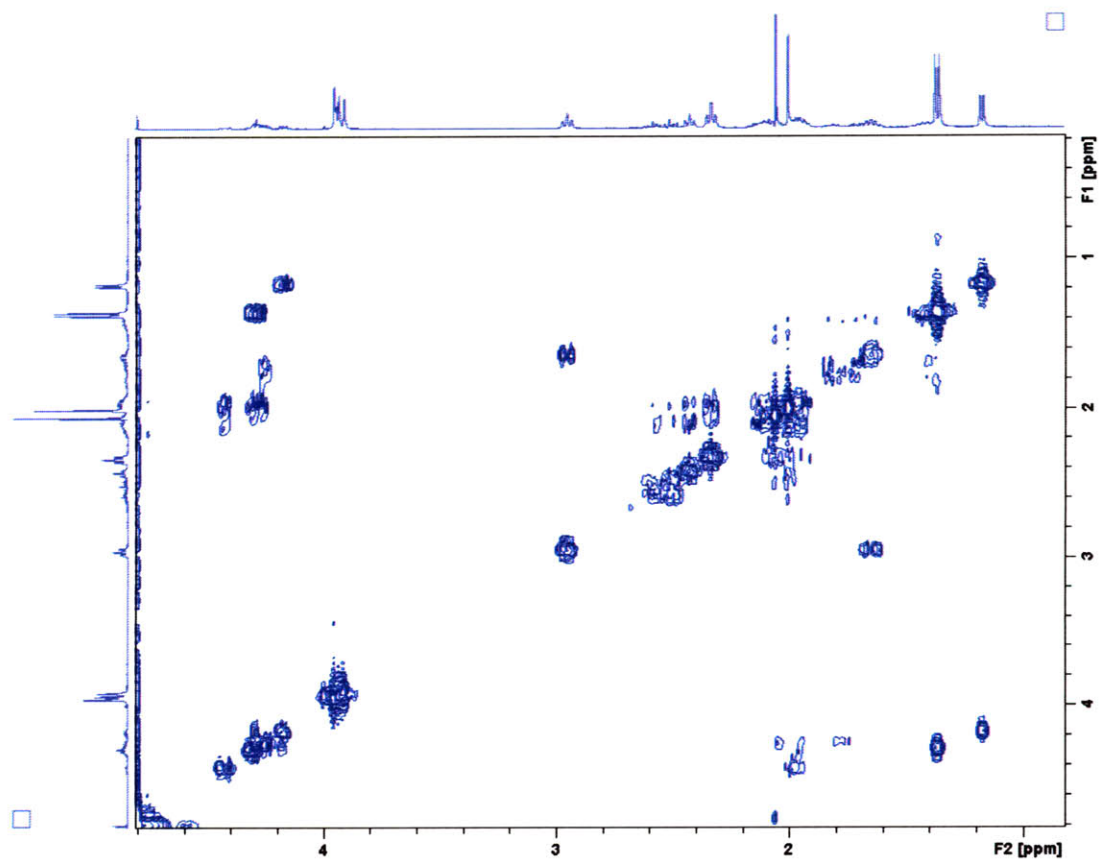


Figure 4-14: The 2D g-COSY spectrum of the IrOx-binding peptide, KGGG-AGETQQAM.

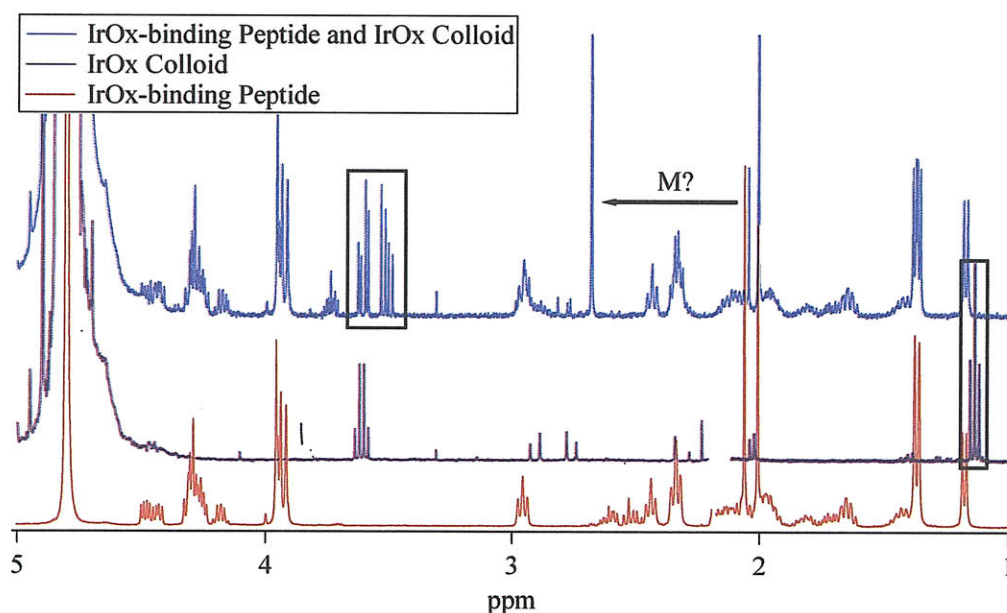


Figure 4-15: An overlay of the 1D NMR spectra of the IrOx-binding peptide, IrOx colloid and mixed colloid and peptide. The mixed spectrum suggests a downfield shift of the methionine residue.

ppm as well as the A CH₃ at 1.4 ppm. The Q CH₂ and M CH₂ peaks at about 2.3 and 2.4 interact with some peaks at around 3.0, but the cross peak does not show the triplet structure of K CH₂ so it is likely that the Q and M residues interact with the IrOx colloid peaks observed around 3.0. The M CH at about 4.4 ppm is observed to have an interaction with the Q CH₂ at about 2.3 ppm. The peaks in the region of 3.48-3.62 ppm thought to be from the IrOx colloid interact with each other, and perhaps the A CH₃ 1.4 ppm. The gROESY results suggest that the M and two Q amino acids play an important role in coordination between the IrOx-binding peptide and the IrOx colloids, perhaps creating a binding pocket among these residues explaining interactions between the alanine and putative IrOx peaks at 3.48-3.62 as well as interactions between the M and A CH₃ residues.

FTIR

Fourier transform infrared spectroscopy (FTIR) was used to characterize the IrOx colloid, IrOx-binding peptide, and mixed system. Samples were dried onto ZnS plates

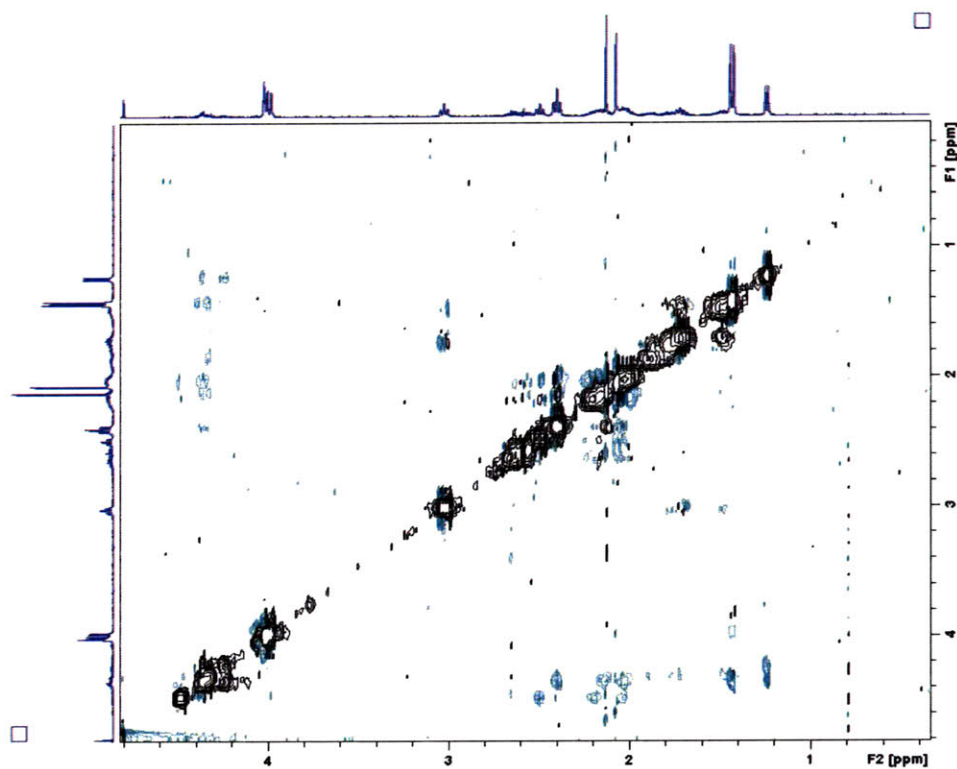


Figure 4-16: Through-space interactions of the IrOx Peptide, measured using gROESY 2D-NMR spectroscopy.

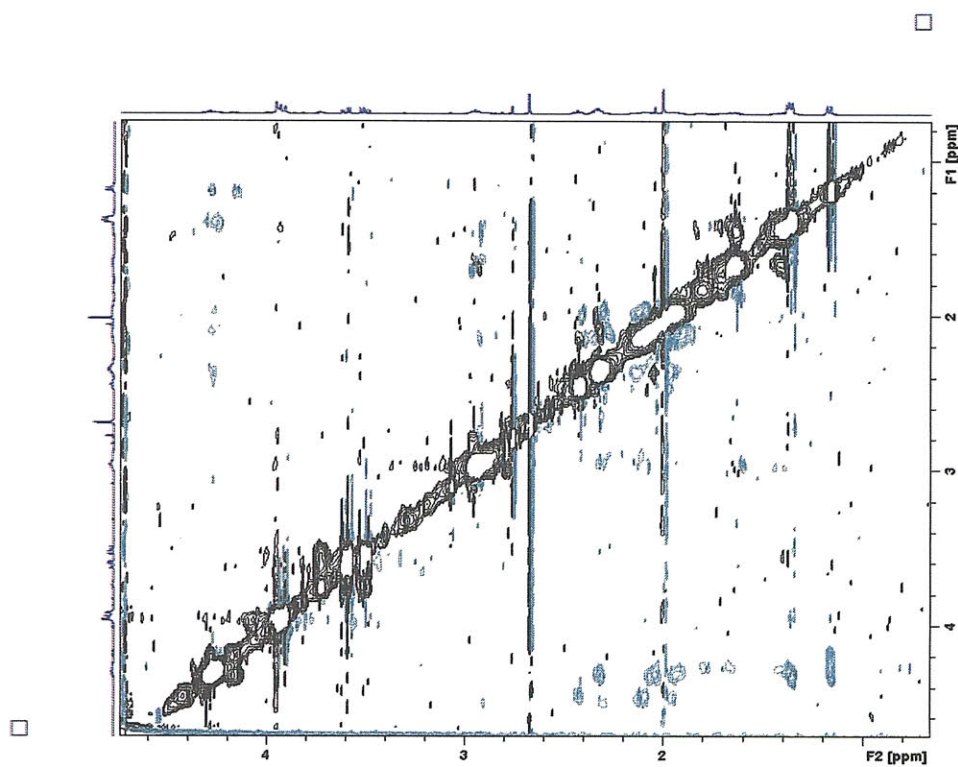


Figure 4-17: Through-space interactions in the combined IrOx-binding peptide / IrOx colloid system, measured using gROESY 2D-NMR spectroscopy.

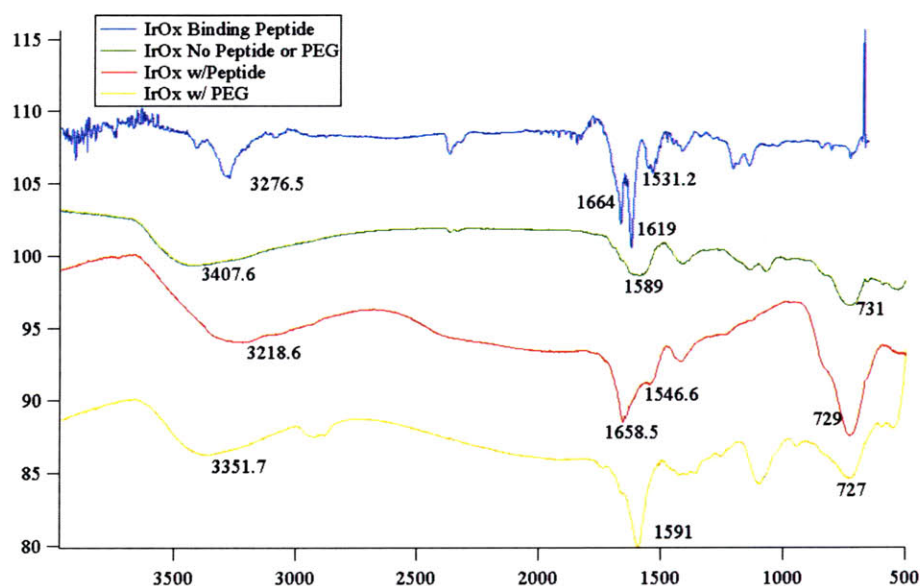


Figure 4-18: FTIR spectra of the IrOx colloid, PEG-capped IrOx colloid, IrOx Peptide/Colloid complex and IrOx-binding peptide.

and FTIR spectra recorded using a Nicolet Magna 860 Fourier Transform Infrared Spectrometer. Figure 4-18 shows the FTIR spectra from the colloid, colloid synthesized with PEG, IrOx colloid with IrOx-binding peptide, and IrOx-binding peptide. The FTIR of the IrOx-binding peptide shows a broad, but clearly defined peak at 3276.5, likely from the N-H stretch of the lysine and glutamine residues, perhaps broadened by the tyrosine alcohol. The IrOx colloid shows a broad peak at 3407.6, likely from water and hydroxyl groups on the colloid surface. When the peptide and colloid are combined, a broad band can be found at 3218.6, significantly shifted from either the colloid or the peptide independently. The FTIR of the PEG conjugated particles show no such shift, suggesting that interactions between the amide groups in the peptide and the hydroxyl groups on the colloid may be taking place.

HPLC

The IrOx-binding peptide and IrOx colloids were mixed at different Ir atom:peptide ratios. High performance liquid chromatography was performed on the different sam-

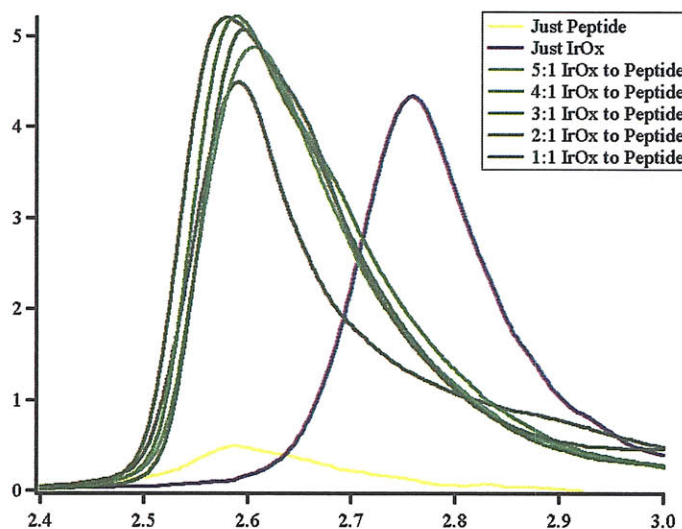


Figure 4-19: HPLC of the IrOx colloid coordinated to the IrOx-binding peptide at different ratios.

ples by Y. S. Nam, Figure 4-19. The signal is higher for samples containing IrOx than the sample with just peptide because the colloid exhibited higher absorbance at the 400 nm wavelength. The HPLC results clearly show that the IrOx-binding peptide coordinates IrOx colloids. When iridium ions are added in a 1:1 ratio with peptide, the IrOx peak shifts to about the same position as where the peptide peak is observed. Incrementally increasing the Ir:peptide ratio shifts the peak back towards the original colloid peak, but even at a 5:1 ratio, a substantial difference between the two peaks remains.

4.6.2 Peptide Mutants

The synthetic version of the IrOx-binding peptide was originally designed with IrOx-binding sequence, AGETQQAM, coupled to a lysine residue, needed for chemical conjugation, by a tri-glycine linker. The flexible GGG linker is used to minimize the influence coupling another molecule to the peptide has on the binding pocket. For catalytic water splitting some interaction is desired between the porphyrin and the IrOx colloid, so the structure of this linker was investigated to study whether structural

Linker Sequence	K to B.S. Distance	Radius of Gyration
GGG	28.8	11.5
AP	29.2	11.8
APAP	30.8	13.1
GPGP	31.7	13.9
GPGPGP	17.7	6.9
PPPPPP	14.2	7.7
E-IrOXPAPYPA	6.1	7.3
APYPAP	28.3	13.2

Table 4.6: The computationally determined radii of gyration and distance between linker and binding pocket for IrOx-binding peptides with different linker sequences.

changes to the peptide could promote better electron transfer between the colloid and porphyrin. The peptide linker was modified in three different ways, length, charge transfer, and functionalization. Tinker/FFE (Washington University) was used with an Amber force field to determine energy-minimized peptide structures in an aqueous environment. Glycine and alanine residues were used as spacer molecules along with structural proline residues to create peptides with different radii of gyration and distances between the IrOx binding site and lysine linking group. Tyrosine was used to study whether an aromatic residue could help facilitate charge transfer between the catalyst and dye. Additional lysines were added to the peptide sequence to probe the effect of the porphyrin/IrOx ratio. Table 4.6 lists the different linker molecules and their respective computed radii of gyration and distances from the lysine residue to the binding pocket. Sequence E-IrOxPAPYPA is essentially the mirror of APYPAP-IrOx, designed to have the tyrosine oriented in a slightly different configuration with respect to the binding pocket.

4.6.3 Oxygen Evolution Data

The iridium oxide-binding peptide was covalently attached to the ZnD630-9 and to the Zn(II) protoporphyrin IX (ZnPPIX) porphyrins in a 1:1 and a 2:1 ratio. Oxygen evolution was measured using a persulfate electron acceptor, Figure 4-20. In each case the peptide-conjugated porphyrin exhibited greater oxygen production. The

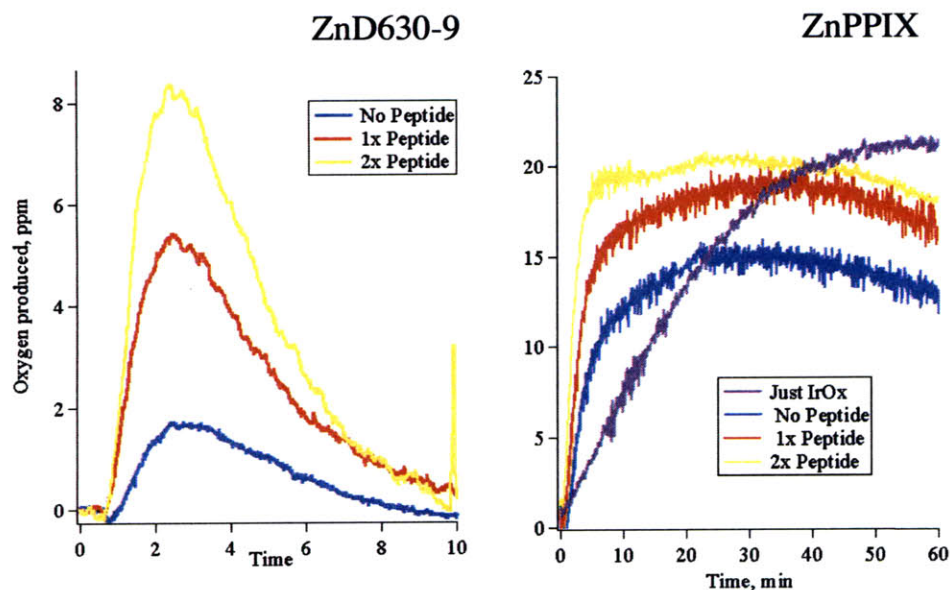


Figure 4-20: Oxygen production from IrOx - peptide - porphyrin complexes using ZnD630-9 (L) and ZnPPIX (R) peptides.

ZnPPIX porphyrin exhibited superior sustained oxygen production. Unfortunately, these samples foamed significantly during oxygen evolution, damaging the gas dryer. The side products of the coupling reaction had not been removed before the oxygen evolution experiment, perhaps acting as surfactants and creating the foam. The ZnPPIX porphyrin has poor water solubility and precipitated out over time. Surprisingly, conjugation of ZnPPIX to the peptide prevented this precipitation. In future experiments, the peptide-porphyrin conjugates were dialyzed overnight using 1000 MW tubing to remove unreacted reagents.

IrOx-binding peptides containing the different linkers in Table 4.6 were synthesized and tested for oxygen-producing capabilities. Due to a mix-up on synthesis, the IrOx-binding sequence was transmuted to AGEQQ TAM. By all indications, this peptide still coordinates the IrOx colloid. The values in Table 4.6 were calculated for the modified IrOx-binding sequence. Because of variation in the IrOx colloid synthesis and its poor stability when not PEG-capped, each peptide was run in parallel with the IrOx-binding peptide containing the KGGG linker so that evolved oxygen values

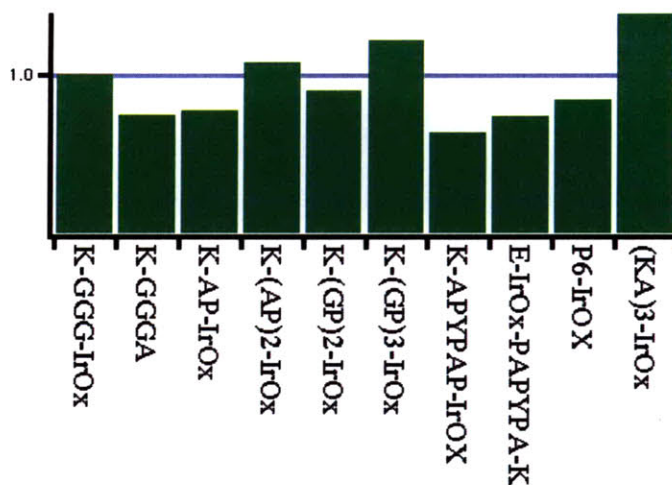


Figure 4-21: Oxygen production from peptides with containing different linker sequences. Oxygen concentration was normalized to that of a simultaneously run K-GGG-IrOx sample.

could be internally normalized to a constant reference. Figure 4-21 shows oxygen production levels referenced to that of the K-GGG-IrOx peptide.

The oxygen production results show no clear connection between either the computed distances between the porphyrin conjugation site and the IrOx-binding site or the peptide radius of gyration. This result is not surprising considering that these simulations did not account for either the presence of IrOx colloid or the porphyrin. There does seem to be some impact of the overall length of the linker sequence, with an increase in oxygen production both going from AP to (AP)₂ and from (GP)₂ to (GP)₃. The (AP)₂ and (GP)₃ residues are both longer than and exhibit better oxygen production than the GGG linker. The best oxygen production was observed using the (KA)₃ linker. These samples contained a smaller total number of peptides, but had 3 porphyrins per peptide rather than just one. This result suggests that the porphyrin:peptide ratio is an important factor in efficient oxygen production.

4.7 Development of a Non-Sacrificial Electron Acceptor

Some of the most effective herbicides bind to the quinone coordinating pocket of PSII [99], because when the quinone is displaced, electrons can no longer be removed from the catalytic core of PSII, photosynthesis stops, and the plant dies. The electron acceptor serves an equally important role in the synthetic IrOx/Porphyrin system: quenching the porphyrin triplet state and accepting an electron from the porphyrin to yield a reactive porphyrin radical cation. The radical cation oxidizes the surface of the IrOx catalyst enabling water oxidation. Without an electron acceptor, the triplet state would either decay non-radiatively or through phosphorescence with no energy transferred to the catalyst surface.

The most commonly used electron acceptor for photocatalytic water oxidation is the persulfate anion. Persulfate has a very high oxidation potential, ≈ 2 V, enabling persulfate to quench the triplet states of some porphyrin molecules that have large (negative) redox potentials [79]. Persulfate has the added advantage that a single persulfate molecule can produce two radical cations, as described in Section 4.2.2, doubling the potential quantum yield of oxygen evolution. Persulfate, however, is a sacrificial electron acceptor. The addition of an electron to persulfate cleaves a covalent bond, inhibiting the simple re-oxidation of the persulfate acceptor. Persulfate is problematic because it can yield sulfate radical anion species that can damage either the porphyrin or the catalyst material. Furthermore, persulfate can undergo dark reactions with ground state porphyrins, causing damage to the porphyrin molecule [79]. Direct oxidation of water by persulfate has been observed under some conditions, potentially leading to erroneous measurement of catalytic performance [48].

Reversibility is an important feature for a good electron accepting material. In PSII, plastoquinone accepts an electron, but it also transports the charge across the thylakoid membrane. In a synthetic system for solar splitting of water, an electron acceptor serves to transport the electron from the O_2 half reaction to the H_2 half reaction, where the acceptor is re-oxidized, leaving the molecule ready to accept

another electron. The irreversible nature of persulfate prevents its use in this capacity, illuminating the need for non-sacrificial electron-accepting compounds. Potential non-sacrificial electron acceptors must be able to readily undergo reversible one electron redox reactions. The redox potential, if possible, should be similar to that of persulfate because, as Harriman and coworkers show, the triplet states of some porphyrins are barely quenched by persulfate [79].

4.7.1 Currently Used Non-sacrificial Electron Acceptors

Metal cation redox couples such as Ce(III)/Ce(IV) and Fe(II)/Fe(III) are suitable non-sacrificial electron acceptor candidates because they can be easily and reversibly reduced. Ce(IV) is widely used as a non-sacrificial electron acceptor for photocatalytic water splitting [4, 30, 72]. The Ce(III)/Ce(IV) couple was recently used in a photochemical cell to shuttle charge between platinized titania photoelectrodes enabling the simultaneous production of hydrogen and oxygen [59]. Fe(III) and Hg(II) have each been examined as electron acceptors in photocatalytic systems using metal oxide catalyst with or without a $[\text{Ru}(\text{bpy})_3]^{2+}$ photosensitizer [23, 4, 72].

4.7.2 Identifying Promising Electron Accepting Materials

Photocatalytic water oxidation sensitized by metalloporphyrin dyes typically functions under alkaline conditions, with Harriman and coworkers identifying only Pd(TSP) that was able to photo-oxidize water efficiently at neutral pH [79]. Accordingly, while Harriman et al. observed that Fe(III) was able to quench the triplet state of porphyrins at less than pH 3.0 [42], there have been no reports to date of water photo-oxidation sensitized by porphyrins employing non-sacrificial electron acceptors.

All of the non-sacrificial electron acceptors described in Section 4.7.1 were used to generate oxygen at low pH. Ce(IV), Fe(III), and Hg(II) are all unstable in water at elevated pH, forming insoluble hydroxide or oxide species and precipitating out of solution. Often chelate molecules, organic ligands that can coordinate metal ions, are used to protect metal ions from hydrolysis. Of these potential metal ion electron

acceptors, Ce(IV) was selected for further experiments because it has the highest redox potential and can be up to 12-coordinate, offering many sites for coupling the ion to organic ligands.

4.7.3 Cerium(IV) Chelate Complexes

Two organic molecules were used to conjugate Ce(IV) ions, 2,6-pyridine dicarboxylic acid (dipic) and diethylene triamine pentaacetic acid (DTPA). Dipic, naturally occurring in bacterial spores [89] is a tridentate ligand, able to coordinate metal ions through the pyridine nitrogen and the two carboxylic acid groups. DTPA has five binding sites per ligand with each acetic acid group able to coordinate to metal ions. The coordinated ring structure of dipic makes the molecule rigid, while DTPA is flexible. The geometry of DTPA makes it unlikely that every binding site interacts with the metal ion. While cerium ions can be up to 12 coordinate, steric constraints make it unlikely that all of these sites can be bound by chelating ligands simultaneously.

Chelation of lanthanides is a common way of improving their properties and stability. Cerium ions chelated by ethylenediaminetetraacetic acid (EDTA) and DTPA have been synthesized and characterized, showing promise for redox flow battery applications [73]. The dipic ligand has been used to improve the optical characteristics of lanthanides by decreasing fluorescence quenching due to water and to improve lanthanide dispersion in sol gel glasses [66]. Cerium ions chelated by dipic with a number of different coordinations have been synthesized. D. L. Hoof et al. report Ce(III) coordinated by two dipic ligands, with one ligand singly protonated yielding a complex that 5-coordinates Ce(III) [47]. Katada et al. report a number of different Ce(IV) dipic complexes, exhibiting between one and three ligands per Ce(IV) ion. Some of these structures exhibited nine-coordinate complexation of Ce by dipic, but none exhibited a crystal structure where every Ce(IV) ion was nine-coordinate. These Ce(IV) dipic ligands are used as catalysts for DNA hydrolysis [55]. Brouca-Cabarrecq et al. report a "zero-dimensional" Ce(III) dipic structure that has three dipic ligands each fully coordinated with a central Ce(III) ion [14].

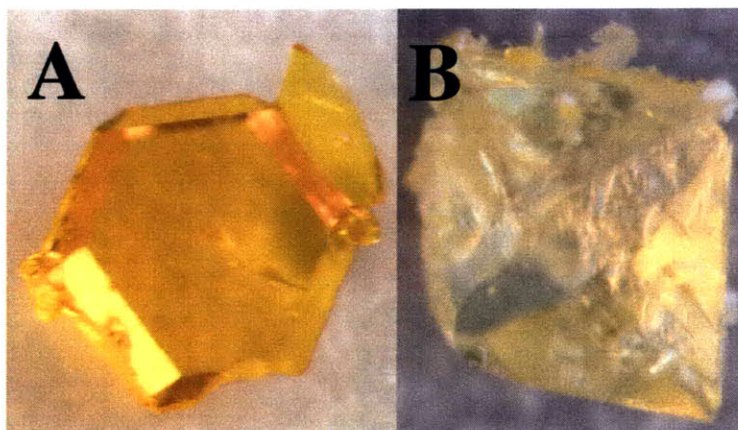


Figure 4-22: (A) A crystal of Ce(III) dipic. (B) A crystal of Ce(IV) dipic.

Synthesis

Ce(III) and Ce(IV) dipic were synthesized from Ce(III) or Ce(IV) ammonium nitrate and dipicolinic acid. The cerium salt was added to a boiling, neutralized aqueous solution of dipicolinic acid. Upon cooling, the solution was adjusted to pH 8.0 to fully deprotonate the dipicolinic acid, thereby enabling complete coordination to the cerium ions. The precise conditions for pH adjustment are important; if the pH is adjusted too rapidly or with too strong a base, precipitation of cerium hydroxide will occur. The detailed product is described in Appendix C.15. The product was left to crystallize. Ce(III) dipic formed orange crystals, 1-20 mm in size, with 97% yield, while Ce(IV) dipic formed yellow crystals, 1-20 mm in size, with 67% yield. Figure 4-22 shows the photographs of Ce(III) dipic and Ce(IV) dipic crystals. The lower yield for the Ce(IV) complex may be a result of the greater instability of the Ce(IV) cation in water. Ce(IV) DTPA was synthesized from Ce(IV) ammonium nitrate and DTPA in the same manner as Ce dipic. When left to crystallize, Ce(DTPA) yields a homogeneous gel. The synthesis of Ce(IV) DTPA is detailed in Appendix C.16.

Characterization

The absorbance spectrum of Ce(III) dipic, Ce(IV) dipic, and Ce(IV) DTPA, Figure 4-23, was measured using a DU-800 spectrophotometer. The peak at 270 nm corre-

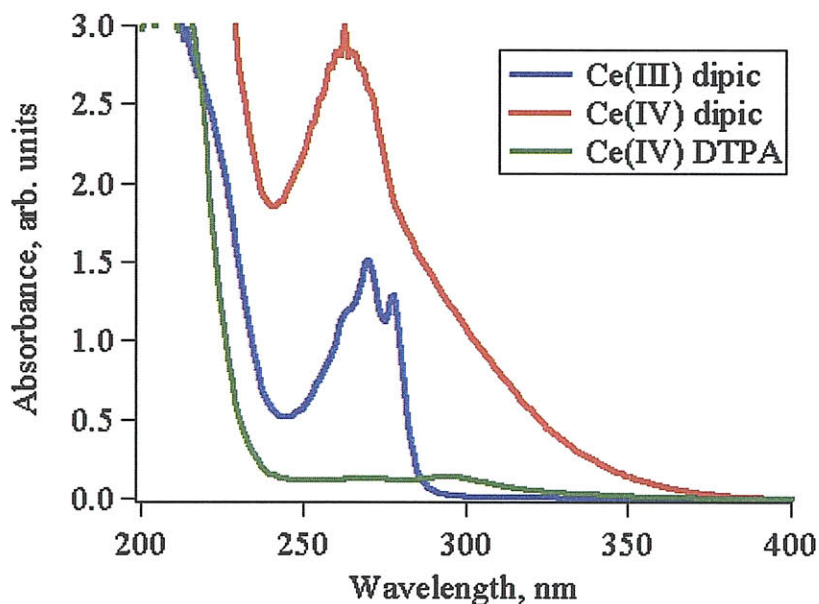


Figure 4-23: Absorbance of Ce(III) dipic, Ce(IV) dipic, and Ce(IV) DTPA.

sponds to the dipicolinate ligand, while the broad band at 300 nm is from Ce(IV). The X-ray crystal structure of the Ce(III) dipic and Ce(IV) dipic was performed by Dr. Peter Mueller. The crystal structures confirmed that the Ce cation is coordinated by three tridentate dipic ligands in both cases. Unfortunately, while the crystal quality was high, a full crystal structure could not be solved for Ce(III) dipic. Ce(IV) Dipic crystallizes in the monoclinic space group P21/n with one molecule of 2, two sodium ions and six water molecules per asymmetric unit. Five of the water molecules, the sodium atoms and the Ce(IV) dipic form an indefinite three-dimensional supramolecular framework, held together by various O-Na interactions, giving rise to Na_2O_2 four-membered rings. The framework is further stabilized by ten crystallographically independent hydrogen bonds. The sixth water molecule fills in remaining voids and is held in place by two additional hydrogen. Figure 4-24 shows the core crystal structure of Ce(IV) dipic with hydrogen atoms, sodium ions, and water molecules omitted for clarity. Additional crystallographic data is included in Appendix C.17.

Ce(III) and Ce(IV) dipic were characterized using ^1H NMR. The NMR spectrum of Ce(IV) dipic shows a triplet centered at 8.365 ppm and a doublet centered at

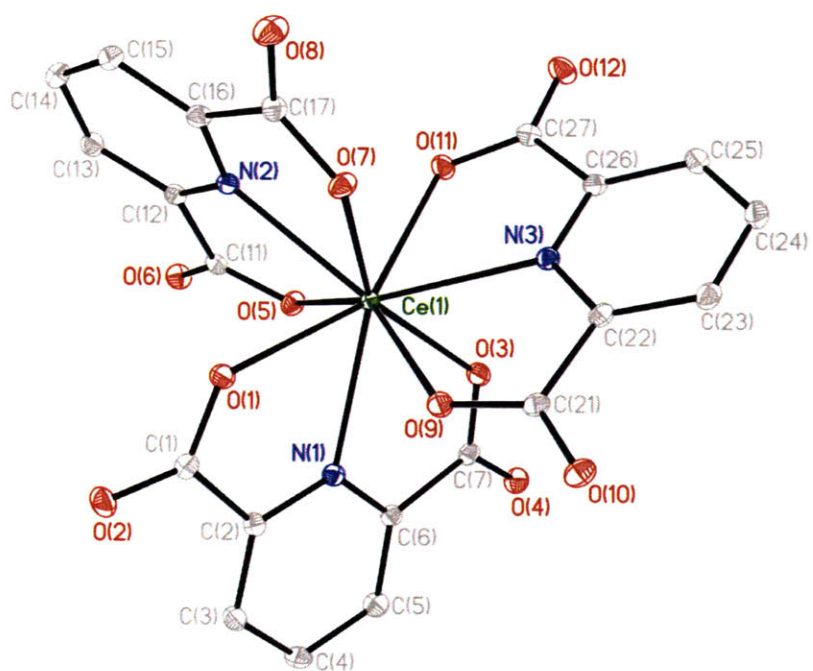


Figure 4-24: Thermal ellipsoid drawing (50% probability level) of the crystal structure of Ce(IV) dipic. Hydrogen atoms, sodium ions and water molecules omitted for clarity. X-ray crystallography by P. Mueller.

8.214 ppm, while the NMR spectrum of Ce(III) dipic shows a broad triplet at 10.655 and a broad doublet at 10.512, Figure 4-25. The differences between NMR signals from Ce(III) and Ce(IV) dipic arise because Ce(III) is paramagnetic while Ce(IV) is diamagnetic. Coupling organic ligands to paramagnetic species often results in NMR peak broadening as seen for Ce(III) dipic. Furthermore, a significant downfield shift in the NMR signal from Ce(IV) to Ce(III) dipic is expected because Ce(III) is paramagnetic and Ce(IV) is diamagnetic.

In an effort to explain oxygen evolution observed for Ce(III) dipic, NMR spectra of Ce(III) and Ce(IV) were collected after the addition of the iridium oxide colloid. A small peak from Ce(III) in the Ce(IV) dipic sample and small peaks from Ce(IV) in the Ce(III) dipic sample after the addition of IrOx. (Expanded in Figure C.18). To confirm that the small peaks were caused by interactions with the IrOx colloid not residual H₂O₂, NMR spectra of Ce(III) and Ce(IV) incubated with H₂O₂ were recorded. That the H₂O₂ had no influence on the appearance of these second peaks suggests an equilibrium exchange between the iridium and cerium charge states, established upon addition of the iridium oxide. Details of the NMR measurement are given in Appendix C.18.

Cyclic voltammetry measurements were performed using a three electrode setup with a glassy carbon working electrode, platinum counter electrode, and Ag/AgCl reference electrode. Ce(III) and Ce(IV) dipic show similar redox characteristics with an oxidation peak at about 1.0 V and a reduction peak at about 0.1 V. Ce(III) dipic shows good cycling characteristics and relatively small shift in peak locations with large changes in scan rate. The large peak separation is indicative of slow redox kinetics, perhaps indicating that there is a ligand induced effect. While Ce(IV) dipic has similar CV behavior to Ce(III) dipic, the oxidation peak is smaller, which is reasonable as Ce(III) will be present only in small quantities. The CV response of the uncoupled dipicolinic acid ligand (adjusted to pH 8.0 with NaOH) exhibits current that is an order of magnitude less than the traces with cerium present, indicating the CV response of Ce(III) and Ce(IV) dipic is primarily due to the cerium cation. For Ce(IV) DTPA, the anodic and cathodic peaks are closer together, indicating faster

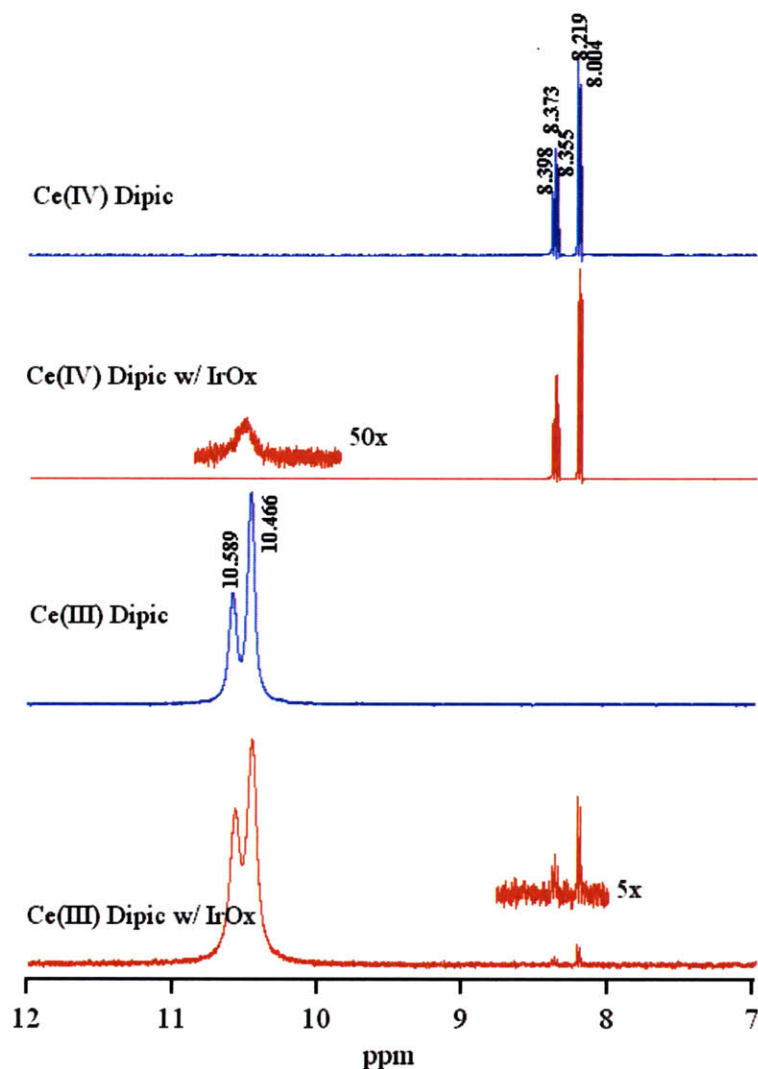


Figure 4-25: NMR spectra of Ce(III) dipic and Ce(IV) dipic dissolved in D₂O, shown before and after addition of iridium oxide colloid. The broadening observed for the Ce(III) dipic sample is an effect often seen for organic molecules coupled to paramagnetic species. After IrOx addition the NMR plot of Ce(IV) shows a small peak at about 10.5 ppm, the position of the Ce(III) dipic peak. Similarly, after IrOX addition the Ce(III) dipic NMR plot shows a small peak at about 8.2 ppm and 8.4 ppm, the position of the Ce(IV) dipic peak. These small peaks are expanded above. Expansion of Ce(III) and Ce(IV) dipic prior to IrOx addition did reveal any peaks.

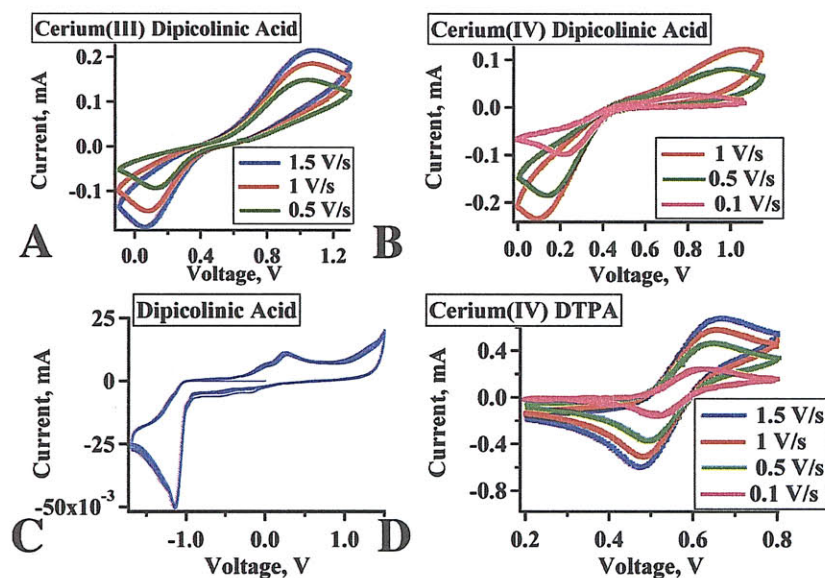


Figure 4-26: Cyclic voltammetry of cerium complexes, measured using a three electrode setup with a glassy carbon working, platinum counter, and Ag/AgCl reference. (A) Ce(III) dipic, (B) Ce(IV) dipic, (C) Dipicolinic acid neutralized with NaOH. (D) Ce(IV) DTPA.

redox kinetics. The Ce(IV) DTPA redox curve is centered about the same place as the Ce dipic complexes. The CV curves are shown in Figure 4-26.

Oxygen Production

The three cerium complexes were tested as electron acceptors in the photocatalytic system described in Section 4.2.2. Oxygen evolution was performed using IrOx as a catalyst and ZnD630-9 and measured using the gaseous oxygen analyzer. The precise experimental conditions for oxygen evolution can be found in Appendix C.19. Some oxygen production is observed from Ce(III) dipic, perhaps a result of the equilibrium between Ce(III) and Ce(IV) established upon addition of iridium oxide that is indicated by NMR. The peak rate of oxygen production from Ce(IV) dipic was 0.24 $\mu\text{mol}/\text{min}$, 2.6 times more oxygen than produced using persulfate as an electron acceptor under identical conditions. Measurement of the UV-Vis absorbance of the oxygen-evolving solution after oxygen production indicates nearly complete conver-

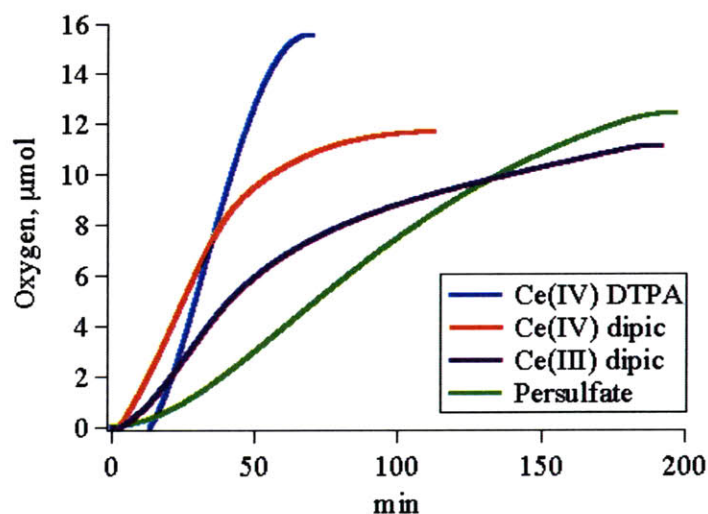


Figure 4-27: Oxygen evolution using Ce(III) and Ce(IV) dipic, Ce(IV) DTPA, or persulfate electron acceptors.

sion of Ce(IV) to Ce(III). The peak rate of oxygen evolution from Ce(IV) DTPA was even higher, $0.39 \mu\text{mol}/\text{min}$, than from Ce(IV) dipic, however precipitation of the electron acceptor and catalyst occurred upon addition of iridium oxide. The oxygen production profile comparing sodium persulfate and the cerium complexes as electron acceptors is shown in Figure 4-27. Ce(IV) dipic was able to serve as an electron acceptor for the photo-oxidation of water across a wide pH range. Oxygen production was demonstrated at pH 5.5 with tris(2,2-bipyridyl) ruthenium(II) chloride, at pH 8 with Pd(II) protoporphyrin IX (PdPPIX), at pH 9 with 1:1 PdPPIX:ZnD630-9, and at pH 11 with ZnD630-9, each with Ce(IV) dipic as an electron acceptor. Each particular dye was selected for its ability to efficiently catalyze water under the particular pH conditions. Figure 4-28 depicts the total levels of oxygen evolved at each pH.

Regeneration

The non-sacrificial nature of Ce(IV) dipic was demonstrated by converting Ce(III) to Ce(IV) in an electrochemical cell. A three electrode cell with a glassy carbon working electrode was used to oxidize Ce(III) to Ce(IV) at 1.0 V (Ag/AgCl), with

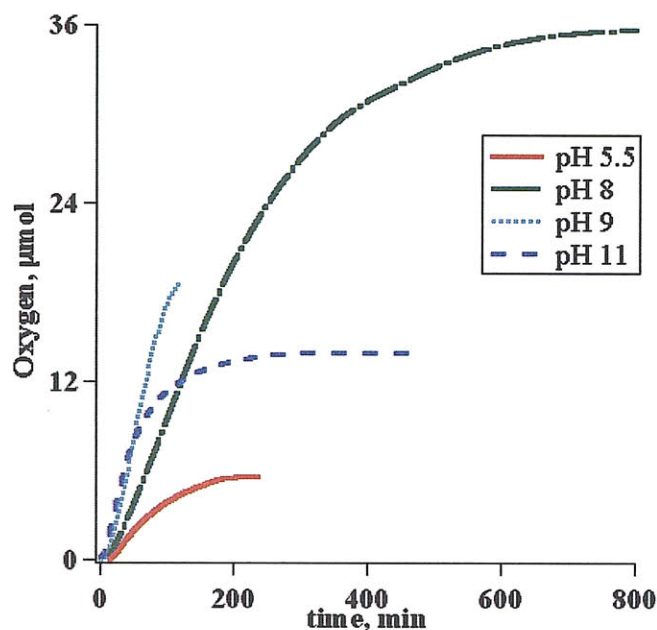


Figure 4-28: Oxygen evolution across a wide pH range using Ce(IV) dipic as an electron acceptor.

conversion of Ce(III) to Ce(IV) quantified by the absorbance of the solution at 294 nm. Experimental details concerning the setup and the calibration used to quantify conversion of Ce ions is described in Appendix C.20. After about 4 hours, $\approx 36\%$ of Ce(III) had been converted Ce(IV) (Figure 4-29). Higher levels of conversion could not be attained, perhaps because of oxidation of the glassy carbon electrode.

To try and achieve greater conversion of Ce(III) to Ce(IV), a flow cell setup, similar to that proposed by Raju et al. [90], was employed. The flow cell, a schematic of which is shown in Figure 4-30, contained a DSA-O2 ($\text{IrO}_2\text{-Ta}_2\text{O}_5$ coating) anode and stainless steel cathode separated by a Nafion cation exchange membrane. The anodic potential was held at +3.5 V while a solution of Ce(III) dipic in lithium borate buffer was circulated over the anode. A more detailed description of the flow cell can be found in Appendix C.20. Figure 4-29 shows the conversion of Ce(III) to Ce(IV), as determined from the 294 absorption. After a little more than 2 hours more than 60% of Ce(III) dipic is converted to Ce(IV) dipic. The upper limit to Ce(III) oxidation

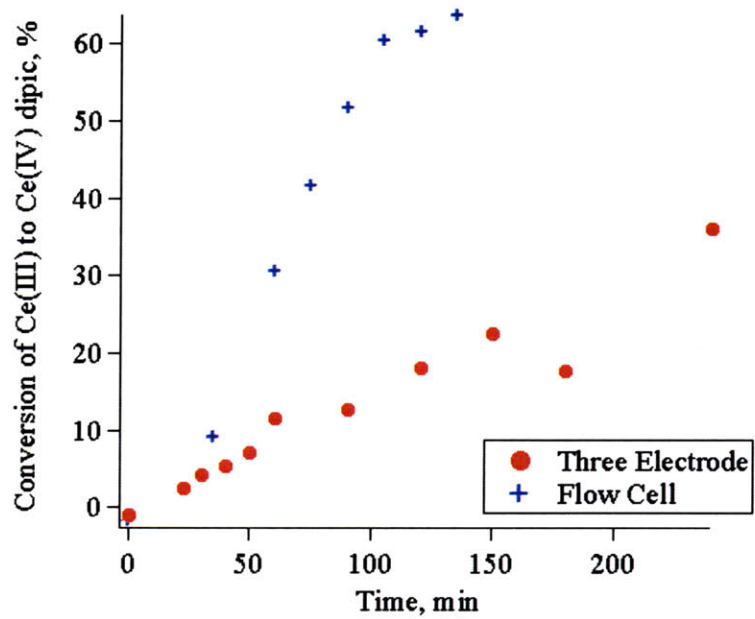


Figure 4-29: Electrochemical conversion of Ce(III) dipic to Ce(IV) dipic, showing time course of conversion using a three electrode setup at 1 V and an electrochemical flow cell at 3.5 V. Ce(IV) concentration quantified by absorbance at 294 nm.

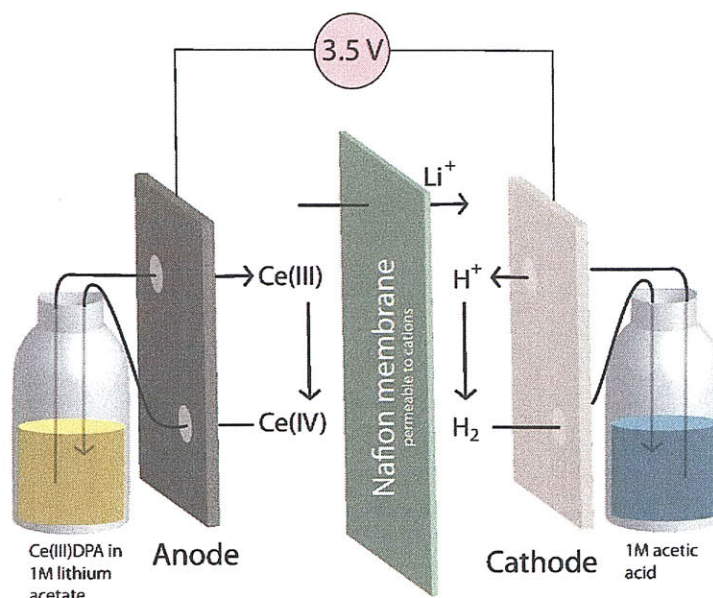


Figure 4-30: A diagram of the two compartment flow cell (Electroanalytica) used to convert Ce(III) to Ce(IV). Image by S. Cui.

in the flow cell setup may be caused by competition with water oxidation at the electrode as the Ce(III) dipic concentration decreases.

The regenerated Ce(IV) dipic was tested as an electron acceptor for photocatalytic water oxidation. The regenerated Ce solution had to be readjusted to pH 11, as the electrochemical regeneration resulted in a large pH drop. Figure 4-31 shows the oxygen production of the regenerated acceptor in comparison to Ce(III) dipic and Ce(IV) dipic. The absolute magnitude of the oxygen production of Ce(IV) dipic differs slightly from Figure 4-27 due to batch to batch variation in the synthesis of the iridium oxide catalyst. The total oxygen produced using the regenerated electron acceptor is nearly as much as is produced using Ce(IV) dipic.

4.7.4 Other Electron Acceptor Candidates.

Prior to selecting the Ce(IV) dipic electron acceptor, a number of other electron acceptor candidates were investigated, including potassium ferricyanide, hematite

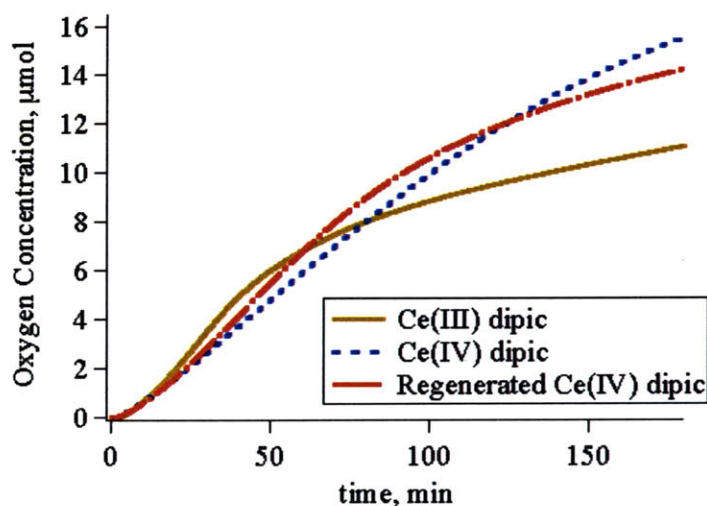


Figure 4-31: A comparison of oxygen produced from regenerated Ce(IV) dipic versus Ce(III) dipic and fresh Ce(IV) dipic.

nanoparticles, iron(III) fluoride, cerium(IV) sulfate, and CeO₂ nanoparticles. Each of these materials, when mixed with IrOx colloid but no porphyrin, exhibited oxygen production when illuminated with no UV filter. Iron(III) fluoride, when used in conjunction with a Zn(TSPP) photosensitizer, exhibited a decrease in oxygen level upon illumination and subsequent increase in oxygen level when the light was turned off. The decrease in oxygen level is an artifact of the analysis method, suggesting either the evolution of a reducing gas such as hydrogen (unlikely because of the high pH) or perhaps formation of oxygen or hydroxyl radicals that interfere with the zirconia oxygen sensor. Some oxygen evolution was observed from α -iron oxide and Ce(IV) sulfate with ZnTSPP, but less oxygen was produced with these “acceptors” than when no acceptor was used. Potassium ferricyanide exhibited initial oxygen production that attenuated rapidly, and again when the light was turned off, the oxygen level rose. While none of these candidates proved to be suitable sodium persulfate replacements, potassium ferricyanide was the most interesting candidate because it remained soluble throughout oxygen evolution and, while exhibiting some strange properties, did evolve some oxygen. Alternative iron complexes may be interesting future candidates as non-sacrificial electron acceptors.

4.8 Future Directions

“Two roads diverged in a yellow wood,” the oft quoted line from Robert Frost’s “The Road Not Taken” seems an appropriate beginning to the discussion of the future directions of this work. Much is yet to be learned about the chemistry and photophysics at the center of this work. Developing a precise understanding of the interactions between peptides and the iridium oxide colloid or conclusively determining whether triplet states are formed at higher quantum efficiency in nanostructured porphyrin arrays could enable more stable and efficient catalytic structures. Alternatively, future work could focus on ways to couple this photo-oxidative system to frameworks for hydrogen generation. This second path is likely to primarily involve engineering challenges, dependent on cleverly designed devices to effectively incorporate the colloidal photocatalytic nanowire system for water oxidation into existing photoelectrochemical technologies in an efficient manner. Specific future directions on several different components of this work are described in the sections that follow.

4.8.1 Light harvesting

One of the benefits of a dye-sensitized system for photo catalytic water splitting is that multiple different dyes can be employed, each working most efficiently at a different wavelength. Systems with a single photoconverter have maximum theoretical solar conversion efficiency of about 30%, however the introduction of a second photoconverter optimized for a different portion of the solar spectrum increases the maximum theoretical efficiency to about 41% [5]. The bacteriophage provides an ideal framework for utilizing multiple photosensitizers. As a proof of concept, PdP-PIX and ZnD630-9 were co-assembled on the bacteriophage to create dual porphyrin nanowires that absorb more of the solar spectrum, Figure 4-32. Palladium porphyrins have the added benefit that they are able to photosensitize the oxidation of water at pH 7 and below. The PdPPIX porphyrin has poor water solubility and thus is not a good candidate for conjugation to phage. The synthesis of other Pd porphyrins, such as PdD630-9, enable higher quality dual porphyrin nanowires and potentially enable

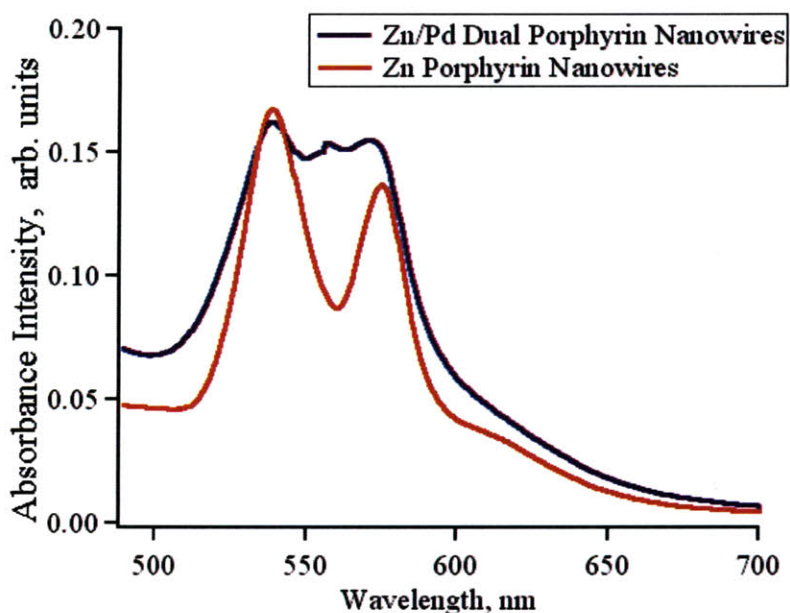


Figure 4-32: Comparing the absorbance spectra of the ZnD630-9 nanowires and dual porphyrin nanowires.

water splitting under less alkaline conditions. Further improvements in the light harvesting structure could be made through the design and synthesis of porphyrins that will yield more organized assemblies on the phage. A highly organized porphyrin array could enable the quantum coherent exciton transfer that has been reported in the Fenna Matthews Olson bacteriochlorophyll complex [33].

4.8.2 Catalyst

The iridium-based catalyst used in this work has limited real-world potential due to the rarity and expense of iridium. Others have shown good catalytic activity using cobalt oxide and other less expensive materials [41], and templating these materials on phage could provide further improvements to their catalytic performance. The biological approach taken in this work inspires the reassessment of manganese-oxo complexes as potential catalyst materials. Manganese is cheap, plentiful and nature demonstrates that it can oxidize water. Furthermore, researchers have not had the framework used in this work available to them. The bacteriophage can provide a

protein scaffold to support and stabilize a particular Mn-oxo structure, while the close proximity of dye molecules and potentially of electron acceptors enables efficient energy transfer to the catalytic site. Manganese is 50 times more abundant than cobalt and 2.5 million times more abundant than iridium. The cost savings from using Mn could compensate for substantially reduced efficiency or stability.

4.8.3 Peptide

Given the purported benefits of nano-scaled arrangement of porphyrins, it is unlikely that a synthetic porphyrin system can exhibit superior photocatalytic performance to phage-assembled hybrid nanowires. Synthetic peptides can serve as a tool to study energy transfer between a catalyst molecule and dye in a more controlled environment. The results described in Section 4.6 indicate that the separation between the dye and catalyst has an impact on the catalytic efficiency. Quantum mechanical simulations of the porphyrin-peptide-IrOx system could provide further insight into the peptide sequences with geometry yielding the optimal spacing between porphyrin and catalyst. While the addition of aromatic residues showed no enhanced oxygen production, more sophisticated models may yield peptide sequences that can better facilitate electron transfer.

4.8.4 Electron Acceptors

Ce(IV) dipic fills the void of non-sacrificial electron acceptors that are compatible with porphyrin photosensitizers, enabling porphyrin-based systems to be coupled to hydrogen-evolving half reactions. Some concerns remain that the high oxidation potential of Ce(IV) dipic will result in energy loss upon reoxidation of the electron acceptor. Potentially, modifications to the dipic ligands could tune the redox potential of a Ce(IV) electron acceptor to the potential needed to create a porphyrin radical cation state, thereby wasting as little energy as possible upon reoxidation.

In PSII the quinone electron acceptor is affixed to the protein complex until it accepts an electron, at which point the molecule is released into the thylakoid mem-

brane. The electron transport between porphyrin and catalyst has been minimized through co-assembling on the bacteriophage. Electron transport between the excited triplet state and the electron acceptor is still controlled by the concentration of electron acceptor in solution. By designing a peptide sequence that can coordinate Ce(IV) dipic but release Ce(III) dipic, the electron acceptor could be coupled to the bacteriophage backbone, dramatically reducing the time for energy transfer between electron acceptor and dye and potentially minimizing the non-radiative decay of the triplet state and the transfer of the triplet energy to molecular oxygen. The release of the electron acceptor upon reduction opens up the binding site for a fresh Ce(IV) complex.

4.8.5 Hydrogen

The work presented in this chapter focused on the problem of developing a system that can oxidize water. While substantial work still remains to optimize the oxygen production half-reaction, the biggest future challenge is to develop ways to couple the oxygen-evolving half reaction to a hydrogen-evolving half reaction. The dream of a completely photocatalytic system that produces hydrogen and oxygen is still quite far in the future. Recently, many researchers have taken the approach of building photoelectrochemical cells. Mallouk and coworkers recently reported a complete system for water oxidation using a TiO_2 film loaded with $[\text{Ru}(\text{bpy})_3]^{2+}$ dye and iridium oxide nanoparticles [112]. Water oxidation occurs at the IrO_2 surface and electrons are removed by applying a potential between the TiO_2 and the hydrogen-evolving platinum electrode. The multi-scalar microsphere system could be coupled with a non-sacrificial electron acceptor such as Ce(IV) dipic and incorporated into a system such as this fairly easily. Most of the difficulty comes from designing the system so light and electricity are used efficiently. Optimizing electrode design, semipermeable membranes, and cell geometry are all engineering challenges that must be overcome to build an efficient photoelectrochemical cell for the splitting of water.

Appendix A

Phage Display Protocols

A.1 Solutions and Media for Phage Display

A.1.1 LB Medium

- Difco Luria-Bertani (LB) broth, Miller (BD), 25 grams.
- Millipore water, 1 L.
- Autoclave in 2 L Erlenmeyer flask.

A.1.2 Agarose Top

- LB Broth, 25 grams.
- Agarose (OmniPur, EMD), 7 grams.
- Millipore water, 1 L.
- Autoclaved in 2 L Erlenmeyer flask.
- Divided into 50 mL conical tubes.

A.1.3 TBS

- Tris-HCl (OmniPur, EMD), 50 mM (7.88 g).

- NaCl, 150 mM (8.77 g)
- Millipore water, 1L
- Autoclave in 2 L bottle.
- Adjust to pH 7.5

A.1.4 TBS-Tween

- Add 10 μ L (0.1%) or 300 μ L (3%) Tween-20 to 100 mL TBS buffer.
- Sterile filter TBS-T solution.

A.1.5 PEG/NaCl

- Polyethylene glycol, 8000 MW (PEG-8000) (Fluka), 20% w/v (20 grams).
- NaCl, 2.5 M (14.6 grams).
- Millipore water, 80 mL.
- Autoclave in 250 mL bottle.
- Separates upon autoclaving, mixed while cooling, becoming homogeneous with a slight haze.

A.1.6 Glycine-HCl

- Glycine (Mallinckrodt), 0.2 M (2.23 g).
- Millipore water, 100 mL.
- Adjusted to pH 2.2.

A.1.7 Tris-HCl

- Tris-HCl (OmniPur, EMD), 1.0 M (2.23 g).
- Millipore water, 100 mL.
- Adjusted to pH 2.2.

A.1.8 Preparation of LB/IPTG/TET plates

- LB Broth, 25 grams.
- Bacto Agar (BD), 15 grams.
- Millipore water, 1L.
- Autoclave in 2 L Erlenmeyer flask.
- Add 1 mL Isopropyl β -D-1-thiogalactopyranoside / bromo-chloro-indolyl-galactopyranoside (IPTG/X-GAL) solution (XTRA-Blue plus X-gal, QBiogene).
- Add 1 mL, 20 mg/mL tetracycline (TET) solution.
- Pipetted \approx 10 mL solution per petri dish (100 mm \times 15 mm) in laminar flow hood.

A.1.9 Strain Maintenance

- Streak out ER2738 *E. coli* (NEB) on a LB-agar plate using a flame-sterilized inoculation loop.
- Incubate at 37°C overnight.
- Plate can be stored for up to about 1 week at 4 °C.
- Stock ER2738 stored at -20 °C.

A.2 Phage Display

A.2.1 Biopanning - Round 1

- Start titer culture. (Early in day)

Add 20 mL LB, 20 μ L TET solution to a 200 mL Erlenmeyer.

Pick a single ER2738 colony off of a plate using a flame-sterilized inoculation loop and add to LB

Incubate at 37 ° for around 6 hours.

- Biopanning

Add 1 mL of 0.1% TBS-T into a micro-centrifuge tube containing the sterilized substrate.

Add 10 μ L of phage library (briefly vortexing before use).

Rock gently for 60 minutes at room temperature.

While sample is incubating, begin the titering steps.

Remove sample from rocker, and rinse 10 times with 1 mL TBS-T, each wash using a separate tube.

Add 0.5 mL glycine-HCL to elute bound phage and rock for 8 minutes.

Immediately pipet solution to new tube and neutralize with 150 μ L Tris-HCl.

Prepare serial dilutions of eluted phage solution. (100 μ L LB with 10 μ L of solution from previous vial).

Amplify eluted phage solution.

A.2.2 Biopanning - Subsequent Rounds

- Add amplified phage to substrate at same concentration as first round.

- Decrease time of exposure to substrate or increase Tween concentration to increase stringency.

A.2.3 Titering

- At least an hour before titering, prepare agarose top.

Microwave agarose top until liquid, but without boiling.

Prepare 4 mL aliquots in 15 mL round-bottomed culture tubes.

Place in 55 °C oven.

Place plates in 37 °C oven.

- Measure OD of bacteria using UV-Vis at 600 nm.
- If the OD > 0.5, add bacteria into micro-centrifuge tubes in 200 μ L aliquots.
- Add 10 μ L of each dilution to bacteria tubes.
- Incubate at room temperature for 5 minutes.
- Remove plates from incubator. If titering a large number of samples, remove no more than 6 at a time.
- Remove agarose-top-containing culture tubes 1 or 2 at a time from oven.
- Transfer infected bacteria to culture tubes.
- Vortex.
- Pour onto labeled, pre-warmed plate, spreading evenly.
- Allow to cool for 5 minutes.
- Invert and incubate overnight at 37 °C.
- Each phage should yield a blue, circular plaque on plate.
- Clear circles indicate wild type colonies.

- Count number of plaques on each plate.
- Plates can be stored at 4 °C for several months.

A.2.4 Amplification

- Dilute overnight culture 1 to 100 in LB (250 μ L culture in 25 mL LB).
- Add 500 μ L of eluted phage to dilution.
- Incubate at 37 °C in shaker for 4.5 hours.
- Transferred to a 50 mL Oak Ridge centrifuge tube.
- Spin for 10 minutes at 10,000 RPM at 4 °C.
- Transfer the supernatant to a fresh tube and re-spin.
- Transfer top 80 % of supernatant to a fresh tube and add 1/6 volume of PEG/NaCl..
- Precipitate phage overnight at 4 °C.
- Spin PEG-NaCl precipitate for 15 minutes at 10,000 RPM.
- Pour off supernatant and re-spin briefly.
- Remove any additional liquid.
- Suspend pellet in 1 mL TBS
- Transfer to a microcentrifuge tube and spin for 5 minutes.
- Transfer the supernatant to a fresh tube and re-precipitate with 1/6 volume of PEG/NaCl.
- Incubate on ice for 1 hour.
- Spin for 10 minutes and discard supernatant.

Table A.1: Titer on sapphire, Phage, pfu/ μ L

Face	Rnd 1	Rnd 2	Rnd 3
A	15000	10000	1400
C	19000	2000	22000
R	17000	10000	7000

- Re-suspend pellet in 200 μ L TBS.
- Titer amplified bacteriophage.

A.2.5 Amplification of Clones for Sequencing

- Dilute overnight culture 1 to 100 in LB.
- Dispense 1 mL diluted culture to 15 mL culture tubes.
- Using a pipet tip pick an individual plaque and add to culture tube.
- Incubate at 37 °C for about 4.5 hours.
- Isolate DNA using a Qiagen QIAprep Spin M13 Kit.
- Submit DNA for sequencing

A.3 Phage display against the A, C, and R faces of sapphire.

A.4 pVIII Library Selection against IrO₂ powder

A type 8 phage display library was used to select phage that displayed peptides with an affinity for IrO₂. Unlike traditional plasmid techniques for modifying the pVIII, the type 8 library provides 100% expression of peptides on the N-terminus of each pVIII protein [64]. After three rounds of biopanning against IrO₂ powder (Sigma-Aldrich, 99.9%) two different dominant IrO₂ peptide binding motifs were identified: EQPANSLP and AGETQQAM [114].

Appendix B

Peptide Sequences

B.1 Copper

Several unsuccessful attempts were made to screen against copper wire. Initially, the standard method of acid elution was employed to extract phage from the copper surface. The solution post-elution was blue from dissolved copper ions resulting in *E. coli* death due to copper toxicity. In further screening rounds EDTA and sodium phosphate were employed in an attempt to chelate copper ions, however this still was unsuccessful. Additionally, rather than employing acid elution, direct growth off of the copper surface was attempted to minimize the dissolved copper. This direct grow-off technique was also unsuccessful. The inability of phage to infect *E. coli* and the inhibited *E. coli* growth may be attributed to copper ions that attach to the phage surface and are introduced into the *E. coli* cells upon infection subsequently killing the infected cell.

B.2 Sapphire Peptide Sequences

The enhanced or reduced probability of observing an amino acid with a particular chemical composition at each position of the pIII peptide insert in sequences selected from the A, C and R faces of sapphire.

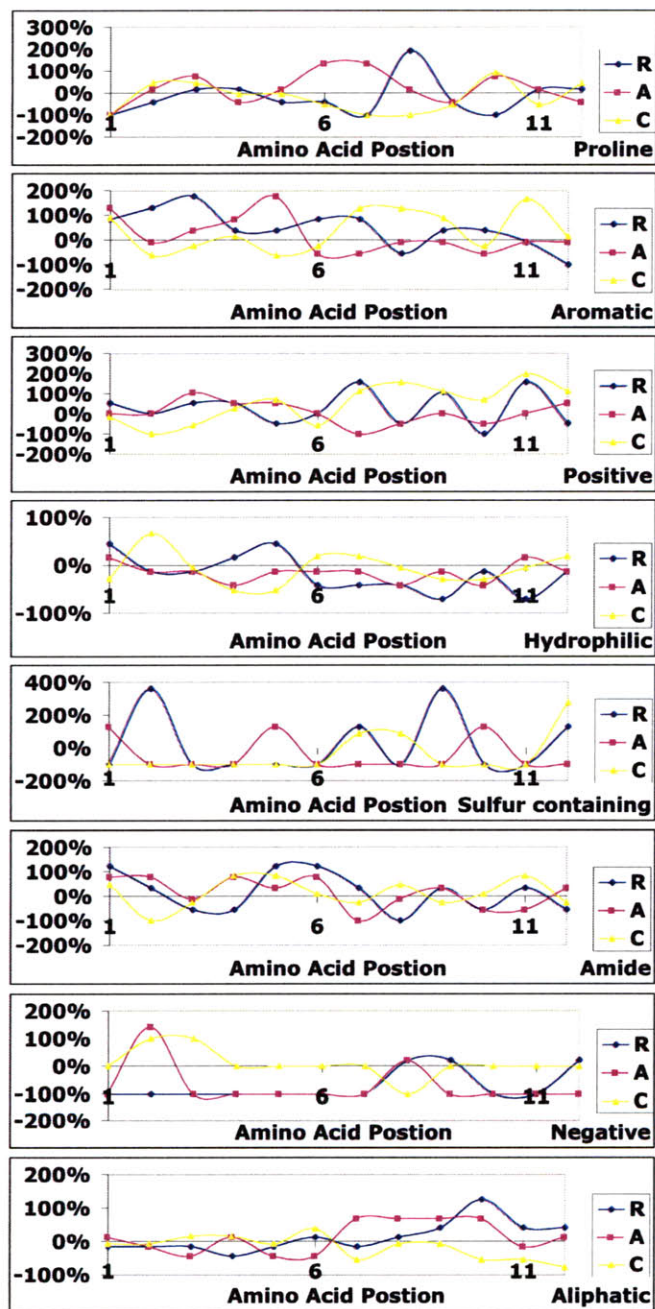


Figure B-1: The enhanced or reduced probability of observing an amino acid with a particular chemical composition at each position of the pIII peptide insert in sequences selected from the A, C and R faces of sapphire.

B.3 Additional peptide sequences

Face	Round	1	2	3	4	5	6	7	8	9	10	11	12	Freq
A	3	H	S	S	W	W	L	A	L	A	K	P	T	1
A	3	H	A	H	S	W	P	P	A	H	Q	L	H	1
A	3	G	L	P	P	Y	S	P	H	R	L	A	Q	1
A	3	S	H	S	H	K	I	L	L	Q	L	T	N	1
A	3, 4	M	P	A	V	M	S	S	A	Q	V	P	R	4
A	4	N	L	R	Q	L	P	L	P	P	P	T	P	1
A	4	A	T	W	S	H	H	L	S	S	A	G	L	1
A	4	Q	H	P	Q	Y	N	P	S	Y	Y	W	L	1
A	4	F	E	R	H	Q	P	L	F	G	A	R	S	1
A	4	A	N	Y	F	L	P	P	V	L	S	S	S	1
A	4	Y	S	P	A	S	K	S	P	V	P	S	L	1
A	4	A	P	R	L	P	Q	S	L	L	P	Q	L	1
A	4	S	D	N	V	H	T	W	Q	A	M	F	K	2
A	4	Y	Q	L	R	P	N	A	E	S	L	R	F	1
C	3	D	S	S	N	P	I	F	W	R	P	S	S	1
C	3	T	A	D	H	Q	T	Y	S	I	R	A	L	1
C	3	I	T	G	I	I	P	F	T	E	R	S	P	1
C	3	S	S	T	L	D	A	R	M	R	W	E	R	1
C	3, 4	L	L	A	D	T	T	H	H	R	P	W	T	2
C	4	H	E	P	T	R	V	I	A	P	E	H	P	1
C	4	Q	T	G	G	I	G	M	R	S	G	I	R	1
C	4	L	V	S	R	H	T	Y	S	H	P	H	M	1
C	4	F	P	H	I	S	S	K	G	T	T	H	T	1
C	4	W	S	P	G	Q	Q	R	L	H	N	S	T	1
C	4	G	F	E	H	K	D	Q	R	F	T	R	E	1
C	4	W	A	P	P	L	F	R	S	S	L	F	Y	1
C	4	W	P	A	N	I	L	S	H	G	P	K	H	1
C	4	N	P	F	N	Q	G	L	H	A	Q	H	P	1
C	4	N	S	Q	F	P	N	S	W	F	S	P	M	1
C	4	K	S	L	S	R	H	D	H	I	H	H	H	1
C	4	T	D	T	P	Q	S	Y	G	W	K	T	R	1
R	3	S	A	H	N	P	T	R	P	I	N	P	L	1
R	3	G	F	K	P	L	Q	L	P	P	W	R	D	1
R	3	S	H	A	A	S	N	K	W	I	F	Q	V	1
R	3	T	A	G	K	V	T	A	S	L	I	G	R	1
R	4	H	M	R	L	S	Q	W	P	L	L	K	P	1
R	4	N	W	T	Y	T	P	R	L	H	L	V	S	1
R	4	H	Q	V	K	I	A	S	A	H	A	H	T	1
R	4	H	M	F	S	Y	A	H	V	R	Y	V	V	1
R	4	I	P	W	T	Q	H	M	A	M	S	P	M	1
R	4	S	H	P	W	N	A	Q	R	E	L	S	V	1
R	4	Q	I	P	R	Q	F	F	P	M	L	A	T	1
R	4	A	T	W	S	H	H	L	S	S	A	G	L	1
R	4	T	S	Y	W	Q	W	S	P	H	T	H	Q	1
R	4	W	Y	Y	P	Y	I	H	D	L	G	R	P	1
R	4	A	P	R	L	P	Q	S	L	L	P	Q	L	1

Table B.1: Sequences selected from the A, C and R faces of sapphire using the 12-mer pIII library.

Sample:	Biopan #:	1	2	3	4	5	6	7	8	9	Freq
Pt	BP3-2	C	M	A	T	S	A	P	R	C	4:8
Pt	BP3-2	C	M	T	S	T	R	H	S	C	1:8
Pt	BP3-2	C	P	S	H	T	N	P	N	C	1:8
Pt	BP3-2	C	L	Q	S	K	L	H	S	C	1:8

Table B.2: Sequences selected for platinum using the 12-mer phage library.

Sample	Biopan#	1	2	3	4	5	6	7	8	9	Freq
ITO-1	BP2	C	T	Q	I	T	S	L	H	C	1:1
ITO-1	BP2	C	V	S	W	P	H	V	S	C	1:1
ITO-1	BP2	C	H	A	P	T	L	Q	L	C	1:1
ITO-1	BP2	C	T	S	T	S	P	Q	S	C	1:1
ITO-1	BP3	C	H	H	N	H	K	K	N	C	2:4
ITO-1	BP3	C	H	Q	K	Y	L	N	T	C	1:4
ITO-1	BP3	C	M	M	N	Q	P	S	I	C	1:4
ITO-1	BP4	C	Q	L	G	T	P	N	T	C	1:10
ITO-1	BP4	C	H	H	N	H	K	K	N	C	9:10
ITO-2	BP1	C	A	Q	L	N	A	I	Y	C	1:4
ITO-2	BP1	C	I	K	Q	V	Q	Q	N	C	1:4
ITO-2	BP1	C	S	L	S	S	K	T	Q	C	1:4
ITO-2	BP1	C	Y	G	L	R	L	P	Q	C	1:4
ITO-2	BP2	C	S	S	P	F	S	T	Y	C	1:4
ITO-2	BP2	C	H	V	M	P	H	P	Q	C	1:4
ITO-2	BP2	C	K	T	M	T	K	N	A	C	1:4
ITO-2	BP2	C	P	K	D	A	V	Q	P	C	1:4
ITO-2	BP3	C	L	P	P	A	T	H	S	C	1:4
ITO-2	BP3	C	K	K	H	H	D	M	H	C	1:4
ITO-2	BP3	C	K	P	T	K	H	H	F	C	1:4
ITO-2	BP3	C	V	A	H	Q	Y	S	D	C	1:4
ITO-2	BP4	C	N	L	K	N	P	K	H	C	1:8
ITO-2	BP4	C	K	A	H	T	Q	K	H	C	1:8
ITO-2	BP4	C	S	T	K	H	K	G	H	C	1:8
ITO-2	BP4	C	T	A	R	S	P	A	P	C	1:8
ITO-2	BP4	C	H	K	H	P	N	K	H	C	1:8
ITO-2	BP4	C	H	K	P	H	K	S	H	C	1:8
ITO-2	BP4	C	A	K	W	A	H	Q	H	C	1:8
ITO-2	BP4	C	H	L	T	S	T	N	T	C	1:8
ITO-2	BP5	C	K	A	H	T	Q	K	H	C	4:8
ITO-2	BP5	C	T	V	K	H	P	K	H	C	1:8
ITO-2	BP5	C	K	P	H	H	K	T	T	C	2:8
ITO-2	BP5	C	K	G	H	H	M	T	H	C	1:8

Table B.3: Sequences selected for ITO using the C7C phage library (samples 1 and 2).

Sample	Biopan#	1	2	3	4	5	6	7	8	9	Freq
ITO-3	BP1	C	L	G	L	K	P	Q	T	C	1:4
ITO-3	BP1	C	T	T	D	T	R	R	H	C	1:4
ITO-3	BP1	C	T	Q	A	L	I	G	F	C	1:4
ITO-3	BP1	C	P	R	A	L	T	S	T	C	1:4
ITO-3	BP2	C	R	L	P	W	L	G	R	C	1:4
ITO-3	BP2	C	S	G	Q	Y	K	V	V	C	1:4
ITO-3	BP2	C	N	Q	A	R	T	P	S	C	1:4
ITO-3	BP2	C	R	H	G	D	T	N	L	C	1:4
ITO-3	BP3	C	Q	G	?	?	?	?	F	?	1:4
ITO-3	BP3	C	T	P	S	R	H	T	V	C	1:4
ITO-3	BP3	C	N	M	K	K	G	L	N	C	1:4
ITO-3	BP3	C	K	V	L	P	S	T	R	C	1:4
ITO-3	BP4	C	I	S	Q	S	P	K	T	C	1:4
ITO-3	BP4	C	H	K	P	H	K	H	W	C	1:4
ITO-3	BP4	C	P	H	H	H	R	G	M	C	1:4
ITO-3	BP4	C	P	P	T	H	P	R	H	C	1:4
ITO-3	BP5	C	T	P	S	R	H	T	V	C	1:3
ITO-3	BP5	C	H	K	P	H	K	H	W	C	2:3
ITO-4	BP1	C	L	H	L	K	P	H	S	C	1:4
ITO-4	BP1	C	L	L	E	D	Y	A	V	C	1:4
ITO-4	BP1	C	A	P	V	D	G	H	P	C	1:4
ITO-4	BP1	C	L	S	T	H	G	S	S	C	1:4
ITO-4	BP2	C	P	P	M	H	G	A	T	C	1:4
ITO-4	BP2	C	K	P	V	K	L	Q	R	C	1:4
ITO-4	BP2	C	L	H	T	P	Q	F	V	C	1:4
ITO-4	BP2	C	L	Q	T	P	N	R	Q	C	1:4
ITO-4	BP3	C	F	T	E	N	F	R	H	C	2:4
ITO-4	BP3	C	G	S	A	S	L	A	S	C	1:4
ITO-4	BP3	C	Q	H	T	R	H	H	V	C	1:4
ITO-4	BP4	C	P	F	P	A	S	H	H	C	2:8
ITO-4	BP4	C	W	Q	H	R	T	N	H	C	3:9
ITO-4	BP4	C	F	T	E	N	F	R	H	C	2:8
ITO-4	BP4	C	L	A	L	A	G	Q	T	C	1:8
ITO-4	BP5	C	W	Q	H	R	T	N	H	C	1:8
ITO-4	BP5	C	H	R	D	T	A	N	Q	C	1:8
ITO-4	BP5	C	F	T	E	N	F	H	R	C	1:8
ITO-4	BP5	C	K	P	H	K	M	G	F	C	3:8
ITO-4	BP5	C	P	F	P	A	S	H	H	C	1:8
ITO-4	BP5	C	A	P	H	P	S	R	S	C	1:8

Table B.4: Sequences selected for ITO using the C7C phage library (samples 3 and 4).

Sample	Biopan #	1	2	3	4	5	6	7	8	9	Freq
AI BP-1	3	C	T	K	T	L	W	G	S	C	2:10
AI BP-1	3	C	S	G	N	Y	P	K	L	C	2:10
AI BP-1	3	C	K	A	D	Q	M	H	A	C	1:10
AI BP-1	3	C	V	A	P	S	R	A	T	C	2:10
AI BP-1	3	C	L	S	Q	P	H	W	R	C	1:10
AI BP-1	3	C	P	S	L	S	K	H	S	C	1:10
AI BP-1	3	C	S	G	N	S	E	A	L	C	1:10
AI BP-1	3(2)	C	F	S	K	P	H	N	W	C	1:10
AI BP-1	3(2)	C	S	G	N	Y	P	K	L	C	2:10
AI BP-1	3(2)	C	T	S	Q	S	Q	H	M	C	1:10
AI BP-1	3(2)	C	L	T	A	Q	G	L	F	C	1:10
AI BP-1	3(2)	C	V	A	P	S	R	A	T	C	2:10
AI BP-1	3(2)	C	N	S	K	V	L	W	G	C	1:10
AI BP-1	3(2)	C	S	P	Y	T	R	A	A	C	1:10
AI BP-1	3(2)	C	Q	S	P	T	R	W	T	C	1:10
AI BP-1	4	C	D	Q	R	H	P	Q	Q	C	1:10
AI BP-1	4	C	S	P	Y	T	R	A	A	C	1:10
AI BP-1	4	C	T	K	T	L	W	G	S	C	3:10
AI BP-1	4	C	N	K	T	Q	P	L	T	C	1:10
AI BP-1	4	C	V	A	P	S	R	A	T	C	2:10
AI BP-1	4	C	M	E	S	S	R	S	S	C	1:10
AI BP-1	4	C	S	G	N	Y	P	K	L	C	1:10
AI BP-1	5	C	T	K	T	L	W	G	S	C	3:10
AI BP-1	5	C	V	A	P	S	R	G	T	C	7:10
AI BP-6	3	C	K	P	W	T	K	T	S	C	1:8
AI BP-6	3	C	T	T	G	D	T	R	L	C	1:8
AI BP-6	3	C	G	S	T	P	K	A	S	C	1:8
AI BP-6	3	C	S	N	A	P	R	L	I	C	1:8
AI BP-6	3	C	N	H	T	A	P	H	F	C	1:8
AI BP-6	3	C	Q	H	A	W	H	K	G	C	1:8
AI BP-6	3	C	T	T	H	W	S	P	T	C	1:8
AI BP-6	3	C	S	R	M	N	F	E	C	S	1:8
AI BP-6	4	C	N	S	G	I	W	P	R	C	1:7
AI BP-6	4	C	R	S	S	Q	E	H	L	C	1:7
AI BP-6	4	C	P	H	P	N	T	F	T	C	1:7
AI BP-6	4	C	S	P	V	Y	R	S	W	C	1:7
AI BP-6	4	C	E	Q	S	L	F	S	N	C	1:7
AI BP-6	4	C	H	P	T	S	Q	N	V	C	1:7
AI BP-6	4	C	P	F	S	G	S	G	N	C	1:7
AI BP-7	3	C	V	N	S	T	Q	G	V	C	1:3
AI BP-7	3	C	K	P	N	Q	S	F	F	C	1:3
AI BP-7	3	C	I	N	T	K	M	P	S	C	1:3
AI BP-7	4	C	L	W	S	K	T	S	T	C	1:2
AI BP-7	4	C	H	K	S	S	T	T	S	C	1:2

Table B.5: Sequences selected for aluminum using the C7C pIII phage library.

Sample Biopan #	1	2	3	4	5	6	7	8	9	10	11	12	Freq		
AI BP-2	3	Q	G	L	E	Y	T	Q	N	L	T	P	K	T	1:9
AI BP-2	3	M	S	E	H	Q	Y	P	Y	H	P	N	R	1:9	
AI BP-2	3	Y	Y	P	A	S	S	T	I	Q	S	R	P	1:9	
AI BP-2	3	D	S	L	W	L	K	L	S	N	L	H	S	1:9	
AI BP-2	3	S	G	H	Q	L	L	L	N	K	M	P	N	1:9	
AI BP-2	3	D	R	A	P	L	I	P	F	A	S	Q	H	1:9	
AI BP-2	3	L	L	A	D	T	T	H	H	R	P	W	T	1:9	
AI BP-2	3	L	T	L	D	S	N	S	M	L	P	R	L	1:9	
AI BP-2	3	S	S	T	S	H	M	M	I	N	G	F	H	1:9	
AI BP-2	4	S	M	T	V	H	K	L	P	H	H	S	T	1:9	
AI BP-2	4	L	L	A	D	T	T	H	H	R	P	W	T	3:9	
AI BP-2	4	Y	Y	P	A	S	S	T	I	Q	S	R	P	1:9	
AI BP-2	4	T	M	G	F	T	A	P	R	F	P	H	Y	1:9	
AI BP-2	4	N	P	A	K	T	D	I	P	P	L	H	Q	1:9	
AI BP-2	4	H	M	P	T	K	S	A	S	Q	T	Y	F	1:9	
AI BP-2	4	N	L	M	L	P	H	A	T	V	N	Y	P	1:9	
AI BP-3	3	N	L	M	L	P	H	A	T	V	N	Y	P	1:10	
AI BP-3	3	L	P	I	P	S	S	L	G	G	P	F	P	2:10	
AI BP-3	3	M	P	S	L	S	P	N	Y	Y	W	P	F	1:10	
AI BP-3	3	T	P	Q	S	D	L	L	A	P	T	S	S	1:10	
AI BP-3	3	T	Y	H	S	T	M	W	L	S	Y	K	V	1:10	
AI BP-3	3	L	?	T	E	G	M	?	?	?	?	?	P	1:10	
AI BP-3	3	I	P	T	T	W	L	A	H	R	N	L	A	1:10	
AI BP-3	3	T	I	P	S	K	A	L	T	K	S	F	Y	1:10	
AI BP-3	3	S	P	R	A	Q	T	D	P	L	H	L	P	1:10	
AI BP-3	4	S	T	Q	V	S	K	I	H	R	S	P	F	2:8	
AI BP-3	4	H	I	Y	E	T	G	W	A	P	R	T	G	1:8	
AI BP-3	4	L	P	I	P	S	S	L	G	G	P	F	P	1:8	
AI BP-3	4	S	V	S	V	G	M	K	P	S	P	R	P	2:8	
AI BP-3	4	A	T	W	S	H	H	L	S	S	A	G	L	1:8	
AI BP-3	4	L	T	L	D	S	N	S	M	L	P	R	L	1:8	
AI BP-4	3	K	I	F	N	P	S	S	A	T	S	L	L	1:7	
AI BP-4	3	Q	H	A	N	H	Q	A	W	N	N	L	R	2:7	
AI BP-4	3	Q	S	N	Y	T	R	Y	I	P	A	S	L	2:7	
AI BP-4	3	T	K	N	M	L	S	L	P	V	G	P	G	1:7	
AI BP-4	3	T	A	Y	S	Y	S	P	E	P	R	V	N	1:7	
AI BP-4	4	Q	S	N	Y	T	R	Y	I	P	A	S	L	1:8	
AI BP-4	4	Q	H	A	N	H	Q	A	W	N	N	L	R	1:8	
AI BP-4	4	S	A	H	G	T	S	T	G	V	P	W	P	1:8	
AI BP-4	4	E	S	S	Y	S	W	S	P	A	R	L	S	2:8	
AI BP-4	4	G	Q	S	P	H	S	Y	Q	P	R	T	Y	2:8	
AI BP-4	4	S	I	T	P	P	G	M	W	S	Q	S	R	2:8	
AI BP-5	3	G	H	L	I	P	L	R	Q	P	S	H	Q	2:8	
AI BP-5	3	D	T	I	Q	D	R	Q	I	K	G	Y	L	1:8	
AI BP-5	3	H	R	S	A	S	Y	E	P	P	M	Y	L	1:8	
AI BP-5	3	L	I	Q	P	P	R	Y	S	T	T	V	S	1:8	
AI BP-5	3	E	P	W	L	D	S	R	Y	S	P	L	S	2:8	
AI BP-5	3	Y	D	V	R	F	S	P	L	H	R	L	H	1:8	
AI BP-5	4	L	I	Q	P	P	R	Y	S	T	T	V	S	1:3	
AI BP-5	4	N	P	H	I	T	P	W	W	L	T	N	L	1:3	
AI BP-5	4	N	W	S	P	H	S	D	T	S	A	F	H	1:3	

Table B.6: Sequences selected for aluminum using the 12-mer pIII phage library.

Appendix C

Experimental Procedures

C.1 Conjugation of peptides to Amino Qdots

① Buffer Exchange. Total time: 30 minutes

Transfer 1 nmol ($125\mu\text{L}$) Amino Qdots into ultrafiltration unit. (100 kD 4mL Amicon Ultra (Millipore))

Fill remaining volume with PBS, pH 7.4.

Spin at 4000g for 15 minutes.

Refill with PBS, Spin at 4000g (2000 rpm) for 15 minutes. (Until volume reduced to $250\mu\text{L}$)

② Bis[sulfosuccinimidyl] suberate (BS3) reaction. Total time 30 minutes.

Transfer qdots to glass vial.

Add 0.6 mg of BS3 ($1\mu\text{mol}$)

React 30 minutes on rotator.

③ Removal of excess BS3

Remove top cap of NAP column and pour off excess liquid. Remove bottom Cap

Perform 5 buffer exchanges with pH 7.4 PBS (at least 15 mL total). The buffer exchange takes about 15 minutes, so start while dots react with BS3.

Allow equilibration buffer to completely enter the gel bed.

Add sample to column; allow to completely enter gel bed.

Add 250 μ L of PBS, allow to enter gel bed.

Place a test tube under column to collect sample, and elute with 1.0 mL PBS.

④ React with peptide

Add 4 μ mol of peptide (for AO8 7.4 mg) dissolved in 1 mL H₂O to sample.

Mix gently to react for 2 hours.

⑤ Purification

Add sample to ultrafiltration unit. Fill remaining volume with borate buffer (50 mM, pH 8.3). Spin at 4000 g (2000 rpm) for 15 minutes. Repeat 3 times.

Filter through 0.2 μ m syringe filter.

C.2 Procedure for assembling Qdots on an aluminum substrate.

The aluminum substrate was washed for 2 minutes in Liquinox, rinsed 3x with Millipore water, washed for 2 minutes in ethanol and then rinsed again 3x with Millipore water. Qdots were diluted to 10 nM in PBS-Tween (0.1%). The Qdots were incubated with the aluminum substrate overnight, about 12 hours, and rinsed for 30 minutes in PBS-T. Fluorescence was observed on an Olympus IX-51 inverted microscope using a TRITC fluorescence filter and Q-Color 3 camera.

C.3 Conjugation of peptide to p(HEMA-co-MAA)

① Dissolution of pHEMA-co-MAA

Dissolve pHEMA-co-MAA in methanol. (0.1 grams in 15 mL of methanol)

Mix to fully dissolve.

Add 0.5 mL Millipore water to polymer solution

Mix for up to 1 hour to fully dissolve.

② EDC reaction.

Add to 2 mg EDC (dissolve 1 mg in 50 uL H₂O, add 10uL to Polymer mixture)

React for 30 minutes.

③ Peptide addition.

Add solution to 6 mg AO8

React for 1 hour.

④ Purification. Total time: 1 minutes

Add solution to 1 mL H₂O

Spin Down, 30 sec, high speed.

Resuspend in 200 μ L Methanol.

C.4 Conjugation of peptide to carboxylate microspheres.

① Preparation of Microspheres

Polysciences 4.5 μ m, 2.62% in water, microspheres were warmed to room temperature.

500 μ L of microparticles centrifuged at 3500 rpm for 10 minutes.

Pellet resuspended in 0.4 mL of coupling buffer.

Particles re-centrifuged for 10 min at 3500 rpm and resuspended in 0.17 mL coupling buffer.

② **EDC reaction.**

Dissolved 20 mg EDC in 100 μ L coupling buffer.

Added the EDC solution to particles, vortexed.

③ **Peptide addition.**

Added lysine-functionalized peptide, either 0, 0.1 or 1.0 μ mol

Vortexed and incubated 1 hour.

④ **Purification.**

Centrifuged 10 min at 3500 rpm

Rinsed in 0.4 mL wash buffer

Centrifuged 10 min at 3500 rpm

Resuspended in wash buffer.

C.5 Cleaning Sapphire

- Ultrasonicate sapphire pieces 2-3 min. in Millipore water.
- Soak for 30 min. in 10%w/v hydrochloric acid.
- Ultrasonicate for 2-3 min. in Millipore water.
- Ultrasonicate for 2-3 min. in ethanol.
- Dab dry with a Kim Wipe.

C.6 Patterning and Cleaning of ITO Substrates.

① Patterning of ITO Slides

ITO coated glass slides (Delta Technology, 13-30 $\Omega\cdot\text{cm}$) were masked with silicone tape.

Unmasked ITO was removed using aqua regia solution, 100 mL H_2O , 80 mL HCl , 35 mL HNO_3 for 15 minutes.

The slides were rinsed with water and the silicone tape removed.

② Cleaning ITO Slides

The slides were cleaned in piranha solution, 3:1 H_2SO_4 : 30 % H_2O_2 , for 10 minutes.

Rinsed several times in ultra-pure water.

Sonicated in ultra-pure water.

Sonicated in 70 % ethanol in water.

C.7 Modification of Biorad Electroporator to enable continuous pulses

The signals from the “pulse” button on the front face of the electroporator feed into a printed ribbon cable that plugs into the display board. The first two wires control the “pulse” button. These two wires were soldered to the posts of a BNC plug. The signal, monitored by an oscilloscope, is high until the button is pressed, and then low for ≈ 300 ms, independent of the voltage setting. The signal suggests that pressing the button discharges a capacitor, which stimulates the application of a pulse. The BNC terminal can be connected to a function generator to control the application of pulses. Alternatively, a timing circuit designed by B. Neltner that stays high for 3.84 seconds and then goes low for 400 ms will drive the pulsing.

C.8 Conditions for IrO_x NP and NW synthesis using the stirred high voltage pulse cell.

- Samples were pulsed at 1 kV with a 2 to 2.5 mm gap for approximately 10 minutes. There was an ≈ 4 second gap between each pulse.
- 3 mL of 25 mM IrCl₃, neutralized to pH 7.5, and aged for several days was used for each batch.
- Between 30-300 μ L of 5×10^9 phage were used in nanowire syntheses.
- Samples were dialyzed vs 10 mM NaOH overnight in 10kD tubing, yielding a deep purple solution.

C.9 Conditions for oxygen evolution experiment with electro-pulse synthesized nanoparticles.

- Oxygen Evolution Buffer, 1 L
 - 1.19 gm sodium persulfate
 - 71.0 gm sodium sulfate
 - 0.12 gm sodium hydroxide
 - 0.124 gm boric acid
- 10 mL of buffer and 500 μ L of 1:10 IrO₂/ZnTSPP (final concentration, 80 μ M)
- Sample in 20 mL glass vial, sealed with parafilm and purged with N₂ for ≈ 1.5 hours.
- Illuminated with a 30 W fiber light (Dolan-Jenner).
- O₂ monitored using VWR dissolved oxygen electrode.
- The final results were normalized in reference to diffusion of oxygen into the system.

C.10 Procedure for the Chemical Synthesis of IrOx nanoparticles. Adapted from [40]

- Dissolved 0.15 grams of $\text{Na}_2\text{IrCl}_6 \cdot \text{H}_2\text{O}$ (Alfa Aesar) in 125 mL HPLC grade water.
- Added 0.25 grams of sodium citrate (Alfa Aesar).
- Heated, while stirring in a loosely covered amber glass jar, using an oil bath at 90 °C for 4 hours

The solution changed from yellow-brown to blue-gray.

- Left to cool overnight.
- Stirred with 10g Amberlite MB1 ion-exchange resin (Aldrich) for 30 minutes.
- The Amberlite resin was removed by vacuum filtration.
- The solution was diluted by adding 50 mL of water.
- (Optional) 40 mg of 20K MW PEG dissolved in 12.5 mL of water added to coat particles.
- 5 mL of 6% hydrogen peroxide added to fully oxidize colloid surface.
- The solution was purged with N_2 and allowed to sit overnight.

C.11 Recipe for Oxygen Evolution Buffer

- Sodium Sulfate

71.0 grams sodium sulfate (0.5 M) - All persulfate experiments

Sodium sulfate was not used with CeDipic. It is only needed to inhibit the degradation of persulfate.

- Sodium Borate
 - 1.52 grams Sodium Borate (4 mM) - Most Experiments
 - 2.50 grams Sodium Borate (6.6 mM) - Phage NW experiments
 - 6.08 grams Sodium Borate (16 mM) Peptide/CeDPA experiments
- Adjust to pH 11 with NaOH
- 1L Millipore Water

C.12 Data collection from the ZrO2000 Oxygen Analyzer

The ZrO2000 analyzer outputs a current signal corresponding to the O₂ concentration. The range of oxygen levels to which current signal corresponds are set using the oxygen analyzer. For this work, 4-20 mA current range and oxygen range of 0 ppm to 200 ppm were set. Note, with gaseous oxygen concentrations, 1 ppm O₂ is equivalent to 1 μ L of oxygen per L of nitrogen. The current signal was converted to a voltage signal using a $\approx 300 \Omega$ resistor, the voltage was digitized using a NI USB-6212 data acquisition card, and data recorded using IgorPro (WaveMetrics). The current output circuitry was highly prone to induced currents by external electrical noise. These currents could cause feedback in the instrument, disrupting the sensor temperature control loop. To minimize induced currents, output wires were wrapped around a large ferrite bead. Aluminum foil was used to further shield the instruments.

C.13 Inductively Coupled Plasma - Atomic Emission Spectroscopy

Concentrations of P, Zn, and Ir in aqueous solution were determined using inductively coupled plasma atomic emission spectroscopy (ICP-AES). Measurements were

performed at the MIT CMSE using an Horiba Jobin Yvon ACTIVA ICP-AES. The 213.618 emission was used for P, 213.656 emission was used for Zn, the 224.268 emission was used for Ir. The ZnDPEG-conjugated viruses were pretreated in 0.33 M HCl at room temperature overnight.

C.14 Conditions for oxygen evolution with hybrid IrOx/Porphyrin Nanowires

The buffer described in Appendix C.11 was used with a freshly prepared 27 mM solution of sodium persulfate. The solution was connected to the oxygen analyzer and purged for 4 hours with nitrogen before illumination by a 300 W Xe fiber lamp with a 400 nm high pass filter (ThorLabs). The total oxygen was calculated by integrating the transient oxygen curve recorded in IgorPro.

C.15 Synthesis of Ce(III) and Ce(IV) dipic

Cerium(III) dipic, was synthesized by dissolving dipicolinic acid (DPA) (99% Sigma Aldrich) in HPLC grade water (EMD OmniSolv) at 0.3 M concentration. 2M NaOH was added to bring the final concentration to about 0.5 M NaOH. The solution was brought to a boil and stirred magnetically until the DPA was fully dissolved. A solution of 0.75 M cerium(III) ammonium nitrate tetrahydrate (reagent grade, Alfa Aesar) was added to the DPA solution, giving a final Ce(III) concentration of about 0.05 M. The solution was allowed to cool and then adjusted to pH 8.0 dropwise with 0.2 M NaOH. It is critical that this step be performed slowly and that the NaOH not be more concentrated than 0.2 M or cerium hydroxide will precipitate from solution. The product was left to crystallize at room temperature. Cerium(IV) dipic was synthesized in the same manner as Ce(III) dipic using 0.75M cerium(IV) ammonium nitrate (reagent grade, Alfa Aesar). The product was left to crystallize at room temperature.

C.16 Synthesis of Ce(IV)DTPA

Cerium(IV) DTPA was synthesized by dissolving diethylenetriaminepentacetic acid (DTPA) (99% Sigma Aldrich) at 0.1 M in HPLC grade water. This solution was brought to a boil and cerium(IV) ammonium nitrate was added giving a final concentration of 0.1 M Ce(IV). The solution was cooled and the pH was adjusted to pH 8.0 with 2 M NaOH. No precipitation was observed. This was used as a stock solution for further experiments as no crystals form when the solution is left to crystallize.

C.17 X-ray crystallographic characterization of Ce(IV) dipic

Low-temperature diffraction data were collected on a Siemens Platform three-circle diffractometer coupled to a Bruker-AXS Smart Apex CCD detector with graphite-monochromated Mo K α radiation ($\lambda = 0.71073$ Å), performing ϕ and ω -scans. The structure was solved by direct methods using SHELXS [94] and refined against F^2 on all data by full-matrix least squares with SHELXL-97[95] using established methods [76]. All non-hydrogen atoms were refined anisotropically. All hydrogen atoms (except hydrogen atoms on oxygen, which were taken from the difference Fourier synthesis and refined semi-freely with the help of distance restraints) were included into the model at geometrically calculated positions and refined using a riding model. The isotropic displacement parameters of all hydrogen atoms were fixed to 1.2 times the U value of the atoms they are linked to. Details of the data quality and a summary of the residual values of the refinements are listed in Table C.1. All atoms of the asymmetric unit are depicted in Figure C-1.

C.18 Conditions for NMR analysis of Ce dipic

For NMR spectroscopy, samples were dissolved in D₂O at about 0.1 M. NMR data were collected on a 400 MHz Bruker Avance spectrometer (MIT Department of Chem-

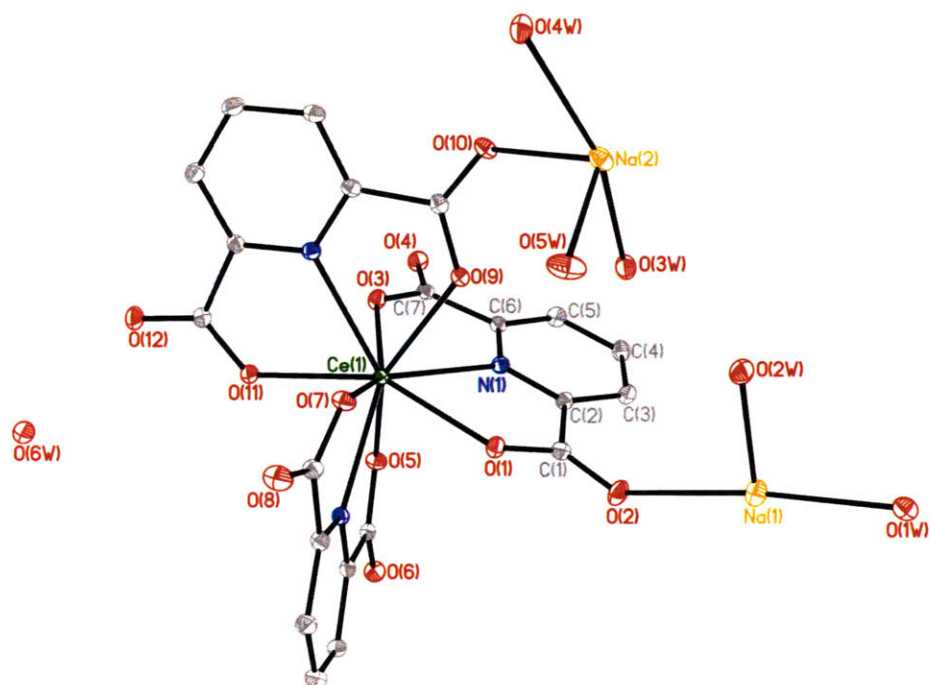


Figure C-1: Thermal ellipsoid representation at the 50% probability level of all non-hydrogen atoms contained in the asymmetric unit in the structure of Ce(IV) dipic. Hydrogen atoms are omitted for clarity. X-ray crystallography by P. Mueller.

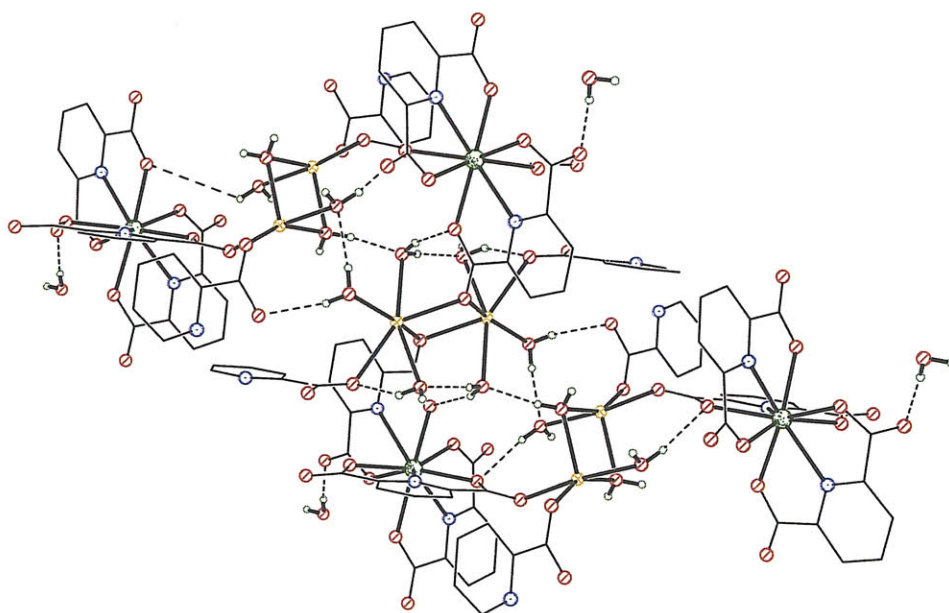


Figure C-2: Ball-and-stick representation of the three-dimensional supramolecular framework of Ce(IV) dipic supported by 12 crystallographically independent hydrogen bonds (dashed lines). Hydrogen atoms bound to carbon were omitted and carbon atoms were drawn with zero-radius for clarity. Color codes for the atom types are as in Figure C-1. X-ray crystallography by P. Mueller.

Identification code	09014
Empirical formula	C21 H21 Ce N3 Na2 O18
Formula weight	789.51
Temperature	100(2) K
Wavelength	0.71073 Å
Crystal system	Monoclinic
Space group	P2(1)/n
Unit cell dimensions	a = 10.1867(10) Å a = 90°. b = 22.127(2) Å b = 95.051(2)°. c = 12.4864(12) Å g = 90°.
Volume	2803.6(5) Å ³
Z	4
Density (calculated)	1.870 Mg/m ³
Absorption coefficient	1.745 mm ⁻¹
F(000)	1568
Crystal size	0.40 x 0.30 x 0.20 mm ³
Theta range for data collection	1.84 to 29.57°.
Index ranges	-14j=hj=14, -30j=kj=30, -17j=lj=17
Reflections collected	73410
Independent reflections	7865 [R(int) = 0.0350]
Completeness to theta = 29.57°	99.9 %
Absorption correction	Semi-empirical from equivalents
Max. and min. transmission	0.7216 and 0.5420
Refinement method	Full-matrix least-squares on F ²
Data / restraints / parameters	7865 / 27 / 442
Goodness-of-fit on F ²	1.058
Final R indices [I ₂ sigma(I)]	R1 = 0.0197, wR2 = 0.0487
R indices (all data)	R1 = 0.0217, wR2 = 0.0501
Largest diff. peak and hole	0.724 and -0.389 e.Å ⁻³

Table C.1: Crystal data and structure refinement for 09014.

istry Instrumentation Facility, NIH Grant #1S10RR13886-01) with Watergate solvent suppression using the 3-19-9 scheme. NMR spectra were collected for Ce(III) dipic and Ce(IV) dipic with and without iridium oxide colloid.

C.19 Conditions for oxygen evolution experiments involving cerium chelates

For photocatalytic water oxidation experiments a solution of photosensitizer, iridium oxide catalyst and electron acceptor was added to 15 mL of buffer solution. Iridium oxide colloid (5 mL of 100 ppm iridium solution), dye (25 μ L, either 8 mM Pd(II) protoporphyrin IX (Frontier Scientific), 8 mM Zn(II) deuteroporphyrin IX 2,4-bis-ethylene glycol (D630-9) (Frontier Scientific), or 80 mM tris(2,2-bipyridyl)dichlororuthenium(II) hexahydrate $[\text{Ru}(\text{bpy})_3]^{2+}$ (Sigma-Aldrich) in DMSO), and electron acceptor (155 μ mols) were added to the buffer solution. $[\text{Ru}(\text{bpy})_3]^{2+}$ was used at higher concentration because of its smaller extinction coefficient. Appropriate buffers were selected for each pH range: at pH 9 and 11, 4mM borate buffer was used; at pH 8, 4mM Tris buffer; and at pH 5.5, 0.1 M sodium acetate with 50 mM sodium sulfate. The sample was placed in a tall, 60 mL glass vial (I-CHEM) and purged with nitrogen gas. The sample was illuminated with a 300 W xenon lamp (Di-Star) using a 515 nm high pass filter (Thor Labs) to isolate the photocatalytic behavior of the organometallic dye, and oxygen was measured using the ZrO2000 oxygen analyzer.

C.20 Experimental Methods for Electrochemical Oxidation of Ce(III) dipic.

C.20.1 Three Electrode Setup

A bi-potentiostat was used to control the voltage of the three electrode setup used to convert Ce(III) to Ce(IV). A 50 x 50 mm, 1 mm thick type 1 glass carbon plate (Alfa Aesar) was used as a working electrode, platinum mesh (Alfa Aesar) was used

as a counter electrode, and an Ag/AgCl reference electrode (BASi) was used. The reaction was performed in a 70 x 50 mm crystallization dish. The starting solution of 100 mL Ce(III) dipic was prepared at 0.1M in HPLC grade water with no additional electrolyte. Upon the application of the 1 V bias, small gas bubbles formed immediately on the platinum mesh and large bubbles slowly nucleated on the glassy carbon electrode. The current began at 0.6 A and decreased over time.

C.20.2 Redox Flow Cell

A redox flow cell (Electroanalytica) was assembled with a DSA-O2 (IrO₂-Ta₂O₅ coating) anode and stainless steel cathode separated by a Nafion cation exchange membrane. Several different bias conditions were tested, with 3.5 V exhibiting the most rapid conversion of Ce(III) to Ce(IV). In the anodic compartment, \approx 50 mL Ce cation solution is recirculated converting Ce(III) to Ce(IV). To balance charge, lithium ions transit across the cation permeable Nafion membrane. In the cathodic chamber 1L of 1.0 M acetic acid is recirculated and protons are converted to hydrogen gas. The concentration of Ce(III) dipic was the same as used for oxygen evolution experiments, 0.123g / 15 mL = 100 mM. A lithium borate buffer was used rather than sodium borate because lithium can more readily diffuse across the membrane.

C.20.3 Absorbance, Calculation of Ce(III) to Ce(IV) conversion.

Figure C-3 shows absorbance curves for Ce(III)/Ce(IV) dipic mixtures. Figure C-4 shows absorbance curves from the electrochemical conversion of Ce(III) to Ce(IV) dipic.

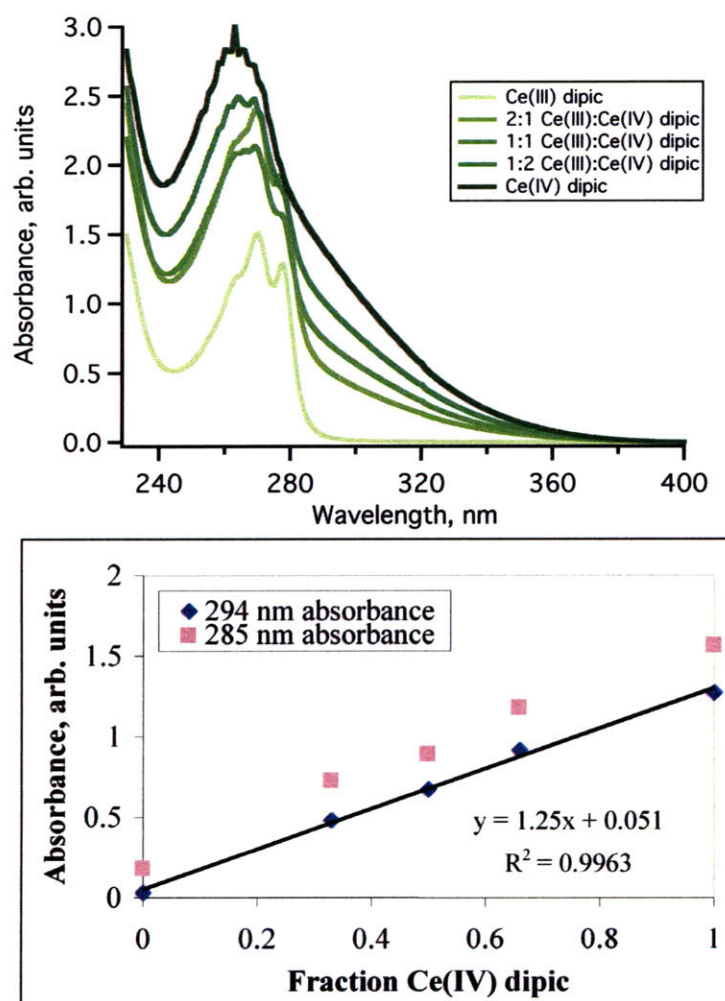


Figure C-3: Absorbance calibration for Ce(IV) dipic concentration.

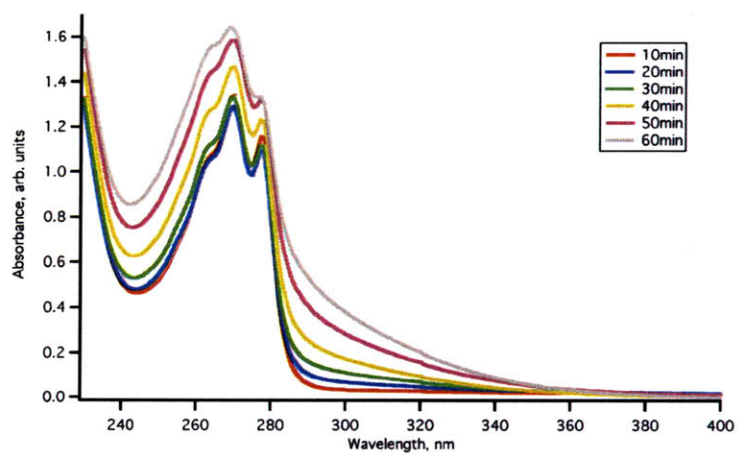


Figure C-4: Absorbance of Ce dipic solution during electrochemical conversion of Ce(III) to Ce(IV) dipic using a electrochemical flow cell.

Bibliography

- [1] Y. Arica and V. N. Hasirci. Immobilization of glucose oxidase in poly(2-hydroxyethyl methacrylate membranes). *Biomaterials*, 8:489–495, 1987.
- [2] Fraser A. Armstrong. Why did nature choose manganese to make oxygen? *Phil. Trans. R. Soc. Lond. B*, 363:1263–2170, 2008.
- [3] D. E. Aspnes and A. Heller. Photoelectrochemical hydrogen evolution and water-photolyzing semiconductor suspensions: Properties of platinum group metal catalyst-semiconductor contacts in air and in hydrogen. *J. Phys Chem*, 87:4919–4929, 1983.
- [4] Gratian R. Bamwenda, Takashi Uesigi, Yoshimoto Abe, Kazuhiro Sayama, and Hironori Arakawa. The photocatalytic oxidation of water to O₂ over pure CeO₂, WO₃, and TiO₂ using Fe³⁺ and Ce⁴⁺ as electron acceptors. *Applied Catalysis A: General*, 205:117–128, 2001.
- [5] Allen J. Bard and Marye Anne Fox. Artificial photosynthesis: Solar splitting of water to hydrogen and oxygen. *Acc. Chem. Res*, 28:141–145, 1995.
- [6] Patrick Batail, Kamal Boubekeur, Marc Fourmigué, and Jean-Christophe P. Gabriel. Electrocrystallization, an invaluable tool for the construction of ordered, electroactive molecular solids. *Chemical Materials*, 10:3005–3015, 1998.
- [7] Martin Z. Bazant, Katsuyu Thornton, and Armand Ajdari. Diffuse-charge dynamics in electrochemical systems. *Physical Review E*, 70(021506), 2004.
- [8] Angela M. Belcher, X. H. Wu, R. J. Christensen, P. K. Hansma, G. D. Stucky, and D. E. Morse. Control of crystal phase switching and orientation by soluble mollusc-shell proteins. *Nature*, 381:56–58, 1996.
- [9] N. Leo Benoiton. *Chemistry of Peptide Synthesis*. CRC Press, Taylor and Francis Group, Boca Raton, FL, 2006.
- [10] Theodore A. Betley, Yogesh Surendranth, Montana V. Childress, Glen E. Aliger, Ross Fu, Christopher C. Cummins, and Daniel G. Nocera. A ligand field chemistry of oxygen generation by the oxygen-evolving complex and synthetic active sites. *Phil. Trans. R. Soc. Lond. B*, 363:1293–1303, 2008.

- [11] R. E. Blankenship. *Molecular Mechanisms of Photosynthesis*. Blackwell Science, Oxford, U.K., 2002.
- [12] Geoffrey C. Bond and David T. Thompson. Catalysis by gold. *Catalysis Reviews: Science and Engineering*, 41(3 and 4):319–388, 1999.
- [13] A. D. Brailsford, M. Yussouff, and E. M. Logothetis. A first-principles model of the zirconia oxygen sensor. *Sensors and Actuators B*, 44:321–326, 1997.
- [14] Chantal Brouca-Cabarrecq, Jeanette Dexpert-Ghys, Auguste Fernandes, Joël Jaud, and Jean Chrisitan Trombe. Synthesis, crystal structures and properties of three new lanthanide 2,6-pyridinedicarboxylate complexes with zero-dimensional structure. *Inorganica Chimica Acta*, 361:2909–2917, 2008.
- [15] E. Budevski, G. Staikov, and W. J. Lorenz. Electrocrystallization nucleation and growth phenomena. *Electrochimica Acta*, 45:2559–2574, 2000.
- [16] B. C. Bunker, G. C. Nelson, K. R. Zavadil, J. C. Barbour, F. D. Wall, J. P. Sullivan, C. F. Windisch Jr., M. H. Englehardt, and D. R. Baer. Hydration of passive oxide films on aluminum. *J. Phys Chem B*, 106:4705–4713, 2002.
- [17] E. R. Carraway, J. N. Demas, B. A. Degraff, and J. R. Bacon. Photophysics and photochemistry of oxygen sensors based on luminescent transition-metal complexes. *Anal. Chem*, 63:337–342, 1991.
- [18] Sylvia E. Castillo-Blum, David T. Richens, and A. Geoffrey Sykes. Oxidation of hexaaquairidium(III) and related studies: Preparation and properties of iridium(III), iridium(IV), and iridium(V) dimers as aqua ions. *Inorganic Chemistry*, 28:954–960, 1989.
- [19] Jeffrey G. Catalano, Changyong Park, Zhan Zhang, and Paul Fenter. Termination and water adsorption at the α -Al₂O₃ (012) - aqueous solution interface. *Langmuir*, 22:4668–4673, 2006.
- [20] Eugene W. L. Chan, Sungjin Park, and Muhammad N. Yousaf. An electroactive catalytic dynamic substrate that immobilizes and releases patterned ligands, proteins and cells. *Angewandte Chemie*, 47:6267–6271, 2008.
- [21] Yuan-Chung Cheng and Graham R. Fleming. Dynamics of light harvesting in photosynthesis. *Annu. Rev. Phys. Chem*, 60:241–262, 2009.
- [22] Chung-Yi Chiang, Charlene M. Mello, Jiji Gu, Emilio C. C. M. Silva, Krystyn J. Van Vliet, and Angela M. Belcher. Weaving genetically engineered functionality into mechanically robust fibers. *Advanced Materials*, 19:826–832, 2007.
- [23] Paul A. Christensen, Wilson Erbs, and Anthony Harriman. Photo-oxidation of water in non-sacrificial systems. *J. Chem Soc., Faraday Trans. 2*, 81:575–580, 1985.

- [24] Paul A. Christensen, Anthony Harriman, George Porter, and Pedatsur Neta. A pulse-radiolytic and photochemical study of the oxidation of water by zinc porphyrin π -radical cations. *J. Chem Soc., Faraday Trans. 2*, 80:1451–1464, 1984.
- [25] Kevin T. Chu and Martin Z. Bazant. Nonlinear electrochemical relaxation around conductors. *Physical Review E*, 74(011501), 2006.
- [26] Jessica I. Chuang, Steven G. Boxer, Dewey Holten, and Christine Kirmaier. High yield of M-side electron transfer in mutants of rhodobacter capsulatus reaction centers lacking the L-side bacteriopheophytin. *Biochemistry*, 45(12):3845–3851, 2006.
- [27] L. C. Clark, R. Wolf, D. Granger, and Z. Taylor. Continuous recording of blood tensions by polarography. *J. Appl Physiol.*, 6:189–193, 1953.
- [28] Holger Dau and Michael Haumann. The manganese complex of photosystem II in its reaction cycle. Basic framework and possible realization at the atomic level. *Coordination Chemistry Reviews*, 252:273–295, 2008.
- [29] Ralf Dostatni, Helmut E. Meyer, and Walter Oettmeier. Mapping of two tyrosine residues involved in the quinone- (Q_B) binding site of the D-1 reaction center polypeptide of photosystem II. *FEBS Letters*, 239(2):207–210, 1988.
- [30] Lele Duan, Andreas Fischer, Yunhua Xu, and Licheng Sun. Isolated seven-coordinate Ru(IV) dimer complex with $[\text{HOHOH}]^-$ bridging ligand as an intermediate for catalytic water oxidation. *Journal of the American Chemical Society*, 131:103971–10399, 2009.
- [31] Nicholas J. Durr, Timothy Larson, Danielle K. Smith, Brian A. Korgel, Konstantin Sokolov, and Adela Ben-Yakar. Two-photon luminescence imaging of cancer cells using molecularly targeted gold nanorods. *Nanoletters*, 7(4):941–945, 2007.
- [32] Peter J. Eng, Thomas P. Trainor, Gordon E. Brown Jr., Glenn A. Waychunas, Matthew Newville, Stephen R. Sutton, and Mark L. Rivers. Structure of the hydrated $\alpha\text{-Al}_2\text{O}_3$ (0001) surface. *Science*, 288(5468):1029–1033, 2000.
- [33] Gregory S. Engel, Tessa R. Calhoun, Elizabeth L. Read, Tae-Kyu Ahn, Tomáš Mančal, Yuan-Chung Cheng, Robert E. Blankenship, and Graham R. Fleming. Evidence for wavelike energy transfer through quantum coherence in photosynthetic systems. *Nature*, 446:782–786, 2007.
- [34] Rawil F. Fakhrullin and Renata T. Minullina. Hybrid cellular-inorganic core-shell microparticles: Encapsulation of living cells in calcium carbonate microshells. *Langmuir*, 25(12):6617–6612, 2009.

- [35] Kristina N. Ferreira, Tina M. Iverson, Karim Maghlaoui, James Barber, and So Iwata. Architecture of the photosynthetic oxygen-evolving center. *Science*, 203:1831–1838, 2004.
- [36] Von Th. Förster. Zwischenmolekulare energiewanderung und fluoreszenz. *Annalen der Physik.*, 437:55–75, 1948.
- [37] Akira Fujishima, Koichi Kohayakawa, and Kenichi Honda. Hydrogen production under sunlight with an electrochemical photocell. *J. Electrochem. Soc.*, 122(11):1487–1489, 1975.
- [38] Michikazu Hara, Chad C. Waraksa, John T. Lean, Bradley A. Lewis, and Thomas E. Mallouk. Photocatalytic water oxidation in a buffered tris(2,2'-bipyridyl)ruthenium complex-colloidal IrO₂ system. *J. Phys Chem A*, 104:5275–5280, 2000.
- [39] Anthony Harriman. Luminescence of porphyrins and metalloporphyrins. *J. Chem Soc., Faraday Trans. 2*, 77:1281–1291, 1981.
- [40] Anthony Harriman, Gad S. Nahor, Shlomo Mosseri, and Pedatsur Neta. Iridium oxide hydrosols as catalysts for the decay of zinc porphyrin radical cations in water. *J. Chem Soc., Faraday Trans. 1*, 84(8):2821–2829, 1988.
- [41] Anthony Harriman, Ingrid J. Pickering, John M. Thomas, and Paul A. Christensen. Metal oxides as heterogeneous catalysts for oxygen evolution under photochemical conditions. *J. Chem Soc., Faraday Trans. 1*, 84(8):2795–2806, 1988.
- [42] Anthony Harriman, George Porter, and Philip Walters. Photo-oxidation of metalloporphyrins in aqueous solution. *J. Chem Soc., Faraday Trans. 1*, 79:1335–1350, 1988.
- [43] Christian D. Hodneland and Milan Mrksich. Design of self-assembled monolayers that release attached groups using applied electrical potentials. *Langmuir*, 13(23):6001–6003, 1997.
- [44] Christian D. Hodneland and Milan Mrksich. Biomolecular surfaces that release ligands under electrochemical control. *Journal of the American Chemical Society*, 122:4235–4236, 2000.
- [45] Paul G. Hoertz, Yeong-Il Kim, W. Justin Youngblood, and Thomas E. Mallouk. Bidentate dicarboxylate capping groups and photosensitizers control the size of IrO₂ nanoparticle catalysts for water oxidation. *J. Phys Chem B.*, 111:6845–6856, 2007.
- [46] A. J. Hoff and J. Deisenhofer. Photophysics of photosynthesis. structure and spectroscopy of reaction centers of purple bacteria. *Physics Reports*, 287:1–247, 1997.

- [47] D. L. Hoof, D. G. Tisley, and R. A. Walton. Studies on metal carboxylates. Part III. Pyridine-2-6-dicarboxylates of the lanthanides. Synthesis and spectral studies and the X-ray photoelectron spectra of several pyridine carboxylate complexes. *J. C. S. Dalton*, pages 200–205, 1973.
- [48] D. A. House. Kinetics and mechanism of oxidations by peroxydisulfate. *Chemical Reviews*, 62(3):185–203, 1962.
- [49] Seogjoo Jang. Generalization of Förster resonance energy transfer theory for quantum mechanical modulation of the donor-acceptor coupling. *The Journal of Chemical Physics*, 127:174710, 2007.
- [50] Seogjoo Jang, YounJoon Jung, and Robert J. Silbey. Nonequilibrium generalization of Förster-Dexter theory for excitation energy transfer. *Chemical Physics*, 275:319–332, 2002.
- [51] Xingyu Jiang, Rosaria Ferrigno, Milan Mrksich, and George M. Whitesides. Electrochemical desorption of self-assembled monolayers noninvasively releases patterned cells from geometrical confinements. *Journal of the American Chemical Society*, 125:2366–2367, 2003.
- [52] H. M. Jones and E. E. Kunhardt. Development of pulsed dielectric breakdown in liquids. *J. Phys. D: Appl. Phys.*, 28:178–188, 1995.
- [53] Wen-Hong Kao and Theodore Kuwana. Electrocatalysis by electrodeposited spherical Pt microparticles dispersed in a polymeric film electrode. *Journal of the American Chemical Society*, 106:473–476, 1984.
- [54] George Karreman, Richard H. Steele, and Albert Svent-Gyorgyi. On resonance transfer of excitation energy between aromatic amino acids in proteins. *Biochemistry*, 44:140–143, 1958.
- [55] Hitoshi Katada, Hidetake Seino, and Yasushi Mizobe. Crystal structure of Ce(IV)/dipicolinate complex as catalyst for DNA hydrolysis. *J. Biol. Inorg. Chem*, 13:249–255, 2008.
- [56] Jan Kern, Bernhard Loll, Athina Zouni, Wolfram Saenger, Klaus-Dieter Irrgang, and Jacek Biesiadka. Cyanobacterial photosystem II at 3.2 Å resolution - the plastoquinone binding pockets. *Photosynthesis Research*, 84:153–159, 2005.
- [57] J. W. Kim, A. S. Utada, A. Fernandez-Nieves, Z. B. Hu, and D. A. Weitz. Fabrication of monodisperse gel shells and functional microgels in microfluidic devices. *Angew Chem Int Edit*, 46:1819–1822, 2007.
- [58] Bessel Kok, Bliss Forbush, and Marion McGloin. Cooperation of charges in photosynthetic O₂ evolution-I. A linear four step mechanism. *Photochemistry and Photobiology*, 11(6):371–577, 1970.

- [59] Ekaterina A. Kozlova, Tatyana P. Korobkina, and Alexander V. Voronstov. Overall water splitting over Pt/TiO₂ catalyst with Ce³⁺/Ce⁴⁺ shuttle charge transfer system. *International Journal of Hydrogen Energy*, 34:138–146, 2009.
- [60] Eric M. Krauland. A broadly-binding peptide sequence selected from the PL12 yeast-display library. Private Communication, 2005.
- [61] Eric M. Krauland, Beau R. Peele, K. Dane Wittrup, and Angela M. Belcher. Peptide tags for enhanced cellular and protein adhesion to single-crystalline sapphire. *Biotechnology and Bioengineering*, 97(5):1009–1021, 2007.
- [62] Philipp Kurz, Gustav Berggren, Magnus F. Anderlund, and Stenbjorn Styring. Oxygen evolving reactions catalysed by synthetic manganese complexes: A systematic screening. *Dalton Transactions*, pages 4258–4261, 2007.
- [63] Seung-Wuk Lee, Chuanbin Mao, Christine E. Flynn, and Angela M. Belcher. Ordering of quantum dots using genetically engineered viruses. *Science*, 296(5569):892–895, 2002.
- [64] Soo Kwan Lee, D. S. Yun, and Angela M. Belcher. Cobalt ion mediated self-assembly of genetically engineered bacteriophage for biomimetic Co-Pt hybrid material. *Biomacromolecules*, 7:14–17, 2006.
- [65] Chwee Teck Lim and James C.H. Goh, editors. *A Novel pH Sensor Based on the Swelling a Hydrogel Membrane*, volume 23. ICBME, Springer, 2008.
- [66] A. P. Magyar, A. J. Silversmith, K. S. Brewer, and D. M. Boye. Fluorescence enhancement by chelation of Eu³⁺ and Tb³⁺ ions in sol-gels. *Journal of Luminescence*, 108(49-53), 2004.
- [67] Chuanbin Mao, Daniel J. Solis, Brian D. Reiss, Stephen T. Kottmann, Roza-mond Y. Sweeney, Andrew Hayhurst, George Georgiou, Brent Iverson, and Angela M. Belcher. Virus-based toolkit for the directed synthesis of magnetic and semiconducting nanowires. *Science*, 303(5565):213–217, 2004.
- [68] Gaetano Di Marco, Maurizio Lanza, and Sebastiano Campagna. Luminescent Ru(II)-polypyridine complexes in poly-2-hydroxyethylmethacrylate matrices as oxygen sensors. *Advanced Materials*, 7(5):468–471, 1995.
- [69] R. B. Merrifield. Solid phase peptide synthesis. I. The synthesis of a tetrapeptide. *Journal of the American Chemical Society*, 85:2149–2154, 1963.
- [70] Alexander Milchev. *Electrocrystallization: Fundamentals of Nucleation and Growth*. Kluwer Academic Publishers, Norwell, MA, USA, 2002.
- [71] D. J. Milliron, I. G. Hill, C. Shen, A. Kahn, and J. Schwartz. Surface oxidation activates indium tin oxide for hole injection. *Journal of Applied Physics*, 87(1):572–576, 2000.

- [72] Andrew Mills and Miguel A. Valenzuela. The photo-oxidation of water by sodium persulfate, and other electron acceptors, sensitised by TiO_2 . *Journal of Photochemistry and Photobiology A: Chemistry*, 165:25–34, 2004.
- [73] P. Modiba and A. M. Crouch. Electrochemical study of cerium(IV) in the presence of ethylenediaminetetraacetic acid (EDTA) and diethylenetriaminopentaacetate (DTPA) ligands. *J. Appl. Electrochem*, 38:1293–1299, 2008.
- [74] Masoud Mohseni, Patrick Rebentrost, Seth Lloyd, and Alán Aspuru-Guzik. Environment-assisted quantum walks in photosynthetic energy transfer. *The Journal of Chemical Physics*, 129, 2008.
- [75] Natalie D. Morris, Masahiro Suzuki, and Thomas E. Mallouk. Kinetics of electron transfer and oxygen evolution in the reaction of $[\text{Ru}(\text{bpy})_3]^{3+}$ with colloidal iridium oxide. *J. Phys Chem A*, 108:9115–9119, 2004.
- [76] Peter Müller. Practical suggestions for better crystal structures. *Crystallography Reviews*, 15:57–83, 2009.
- [77] Christopher S. Mullins and Vincent L. Pecoraro. Reflections on small molecule manganese models that seek to mimic photosynthetic water oxidation chemistry. *Coordination Chemistry Reviews*, 252:416–443, 2008.
- [78] G. S. Nahor, P. Hapiot, and A. Harriman. Changes in the redox state of iridium oxide clusters and their relation to catalytic water oxidation. Radiolytic and electrochemical studies. *J. Phys Chem.*, 95:616–621, 1991.
- [79] G. S. Nahor, P. Neta, P. Hambright, A.N. Thompson Jr., and A. Harriman. Metalloporphyrin-sensitized photooxidation of water to oxygen on the surface of colloidal iridium oxides. Photochemical and pulse radiolytic studies. *J. Phys Chem.*, 93:6181–6187, 1989.
- [80] Gad S. Nahor, S. Mosseri, P. Neta, and Anthony Harriman. Polyelectrolyte-stabilized metal oxide hydrosols as catalysts for the photooxidation of water by zinc porphyrins. *J. Phys Chem.*, 92:4499–4504, 1988.
- [81] Ki Tae Nam, Dong-Wan Kim, Pil J. Yoo, Chung-Yi Chiang, Nonglak Meethong, Paula T. Hammond, Yet-Ming Chiang, and Angela M. Belcher. Virus-enabled synthesis and assembly of nanowires for lithium ion battery electrodes. *Science*, 312:885–888, May 2006.
- [82] Yoon Sung Nam. Calculation of the surface reactive sites on nanowires, based on XPS and BET data. Private Communication.
- [83] Nathan Nelson and Charles F. Yocum. Structure and function of photosystems I and II. *Annu. Rev. Plant Biol.*, 57:521–565, 2006.

- [84] Beau R. Peele, Eric M. Krauland, K. Dane Wittrup, and Angela M. Belcher. Design criteria for engineering inorganic material-specific peptides. *Langmuir*, 21:6929–6933, 2005.
- [85] Beau R. Peele, Eric M. Krauland, K. Dane Wittrup, and Angela M. Belcher. Probing the interface between biomolecules and inorganic materials using yeast surface display and genetic engineering. *Acta Biomaterialia*, 1:145–154, 2005.
- [86] E. F. Pettersen, T. D. Goddard, C. C. Huang, G. S. Couch, D. M. Greenblatt, E. C. Meng, and T. E. Ferrin. UCSF Chimera - A visualization system for exploratory research and analysis. *J. Comput. Chem.*, 25(13):1605–1612, 2004.
- [87] Alfred Polson. Some aspects of diffusion in solution and a definition of a colloidal particle. *Journal of Physical Chemistry*, 54(5):649–652, 1950.
- [88] Albert T. Poortinga, Rolf Bos, and Henk J. Busscher. Reversibility of bacterial adhesion at an electrode surface. *Langmuir*, 17:2851–2856, 2001.
- [89] Joan F. Powell. Isolation of dipicolinic acid (pyridine-2:6-dicarboxylic acid) from spores of *bacillus megatherium*. *Biochemical Journal*, 54:210–211, 1953.
- [90] T. Raju and C. Ahmed Basha. Electrochemical cell design and development for mediated electrochemical oxidation-Ce(III)/Ce(IV) system. *Chemical Engineering Journal*, 114:55–65, 2005.
- [91] Patrick Rebentrost, Masoud Mohseni, Ivan Kassal, Seth Lloyd, and Alán Aspuru-Guzik. Environment-assisted quantum transport. *New Journal of Physics*, 11:033003, 2009.
- [92] K. V. Saban, J. Thomas, P. A. Varughese, and G. Vargese. Thermodynamics of crystal nucleation in an external electric field. *Cryst. Res. Technol.*, 37(11):1189–1199, 2002.
- [93] Urartu Ozgur Safek Seker, Brandon Wilson, Sevil Dincer, Il Won Kim, Ersin Emre Oren, John Spencer Evans, Candan Tamerler, and Mehmet Sarikaya. Adsorption behavior of linear and cyclic genetically engineered platinum binding peptides. *Langmuir*, 23:7895–7900, 2007.
- [94] G. M. Sheldrick. Phase annealing in SHELX-90: direct methods for larger structures. *Acta Cryst.*, A46:467–473, 1990.
- [95] G. M. Sheldrick. A short history of SHELX. *Acta Cryst.*, A64:112–122, 2008.
- [96] A. B. Shubnikov and V. F. Parvov. Formation of crystallization centers in a drop of ammonium chloride solution under the action of an electric field. *Soviet Physics - Crystallography*, 6(3):351–356, 1961.
- [97] Asher K. Sinensky and Angela M. Belcher. Biomolecular recognition of crystal defects: A diffuse-selection approach. *Advanced Materials*, 18:991–996, 2006.

- [98] Gerald J. Smith, Kenneth P. Ghiggino, Louise E. Bennett, and Tracy L. Nero. The ‘Q-band’ absorption spectra of hematoporphyrin monomer and aggregate in aqueous solution. *Photochemistry and Photobiology*, 49(1):49–52, 1988.
- [99] Vladimir Sobolev and Marvin Edelman. Modeling the quinone-B binding site of the photosystem-II reaction center using notions of complementarity and contact-surface between atoms. *Proteins: Structures, Functions and Genetics*, 21:214–225, 1995.
- [100] Martin A. Steffen, Kaiqin Lao, and Steven G. Boxer. Dielectric asymmetry in the photosynthetic reaction center. *Science*, 264:810–816, 1994.
- [101] Marek Szklarczyk, Ramesh C. Kainthla, and John O’M. Bockris. On the dielectric breakdown of water: An electrochemical approach. *J. Electrochem. Soc.*, 139(9):2512–2521, 1989.
- [102] Carel J. van Oss. *Interfacial Forces in Aqueous Media*. Marcel Dekker, New York, 1994.
- [103] Geoffery von Maltzahn, Ji-Ho Park, Amit Agrawal, Nanda Kishor Bandaru, Sarit K. Das, Michael J. Sailor, and Sangeeta N. Bhatia. Computationally guided photothermal tumor therapy using long-circulating gold nanorod antennas. *Cancer Research*, 69(9):OF1–OF9, 2009.
- [104] Joseph Wang, Gustavo Rivas, Mian Jiang, and Xueji Zhang. Electrochemically induced release of DNA from gold ultramicroelectrodes. *Langmuir*, 15:6541–6545, 1999.
- [105] Sandra R. Whaley, D. S. English, Evelyn L. Hu, Paul F. Barbara, and Angela M. Belcher. Selection of peptides with semiconductor binding specificity for directed nanocrystal assembly. *Nature*, 405:665–668, 2000.
- [106] John Whitmarsh and Govindjee. Photosystem II. In *Encyclopedia of the Life Sciences*. Macmillan Publishers Ltd, Nature Publishing Group, 2002.
- [107] O. Wichterle and D. Lím. Hydrophilic gels for biological use. *Nature*, 185:117–118, 1960.
- [108] R. L. Willett, K. W. Baldwin, K. W. West, and L. N. Pfeiffer. Differential adhesion of amino acids to inorganic surfaces. *PNAS*, 102(22):7817–7822, 2005.
- [109] Junko Yano, Jan Kern, Kenneth Sauer, Matthew J. Latimer, Yulia Pushkar, Jacek Biesiadka, Bernhard Loll, Wolfram Saenger, Johannes Messigner, Athina Zouni, and Vittal K. Yachandra. Where water is oxidized to dioxygen: Structure of the photosynthetic Mn₄Ca cluster. *Science*, 314:821–825, 2006.
- [110] Woon-Seok Yeo, Christian D. Hodneland, and Milan Mrksich. Electroactive monolayer substrates that selectively release adherent cells. *ChemBioChem*, (7/8):590–593, 2001.

- [111] Woon-Seok Yeo, Muhammad N. Yosaf, and Milan Mrksich. Dynamic interfaces between cells and surfaces: Electroactive substrates that sequentially release and attach cells. *Journal of the American Chemical Society*, 125:14994–14995, 2003.
- [112] W. Justin Youngblood, Seung-Hyun Anna Lee, Yoji Kobayashi, Emil A. Hernandez-Pagan, Paul G. Hoertz, Thomas A. Moore, Ana. A Moore, Devens Gust, and Thomas E. Mallouk. Photoassisted overall water splitting in a visible light-absorbing dye-sensitized electrochemical cell. *Journal of the American Chemical Society*, 131:926–927, 2009.
- [113] Dong Soo Yun. Iridium oxide binding sequence selected using phage pVIII 100% display library. Private Communication.
- [114] Dong Soo Yun. Technique for electro-pulse nanoparticle synthesis. Private Communication.
- [115] Markus Zahn and Tatsuo Takada. High voltage electric field and space-charge distributions in highly purified water. *J. Appl. Phys.*, 54(9):4762–4775, 1983.
- [116] Bo Zhang, Brandon A. Wustman, Daniel Morse, and John Spencer Evans. Model peptide studies of sequence regions in the elastomeric biomineralization protein, lustrin A. I. The C-domain consensus-PG-NVNCT-motif. *Biopolymers*, 63(6):358–369, 2002.
- [117] Jie Zheng, Caiewi Zhang, and Robert M. Dickson. Highly fluorescent, water-soluble, size-tunable gold quantum dots. *Physical Review Letters*, 93(7):077402–1–077402–4, 2004.
- [118] Rongjun Zuo, Dogan Örnek, and Thomas K. Wood. Aluminum- and mild steel-binding peptides from phage display. *Applied Genetics and Molecular Biotechnology*, 68:505–509, 2005.